The Dissertation Committee for Kaimin Yue Certifies that this is the approved version of the following dissertation:

HEIGHT CONTAINMENT OF HYDRAULIC FRACTURES IN LAYERED RESERVOIRS

Committee:

Jon E. Olson, Supervisor

Richard A. Schultz

John T. Foster

Maša Prodanović

Julia F.W. Gale

HEIGHT CONTAINMENT OF HYDRAULIC FRACTURES IN LAYERED RESERVOIRS

by

Kaimin Yue

Dissertation

Presented to the Faculty of the Graduate School of
The University of Texas at Austin
in Partial Fulfillment
of the Requirements
for the Degree of

Doctor of Philosophy

The University of Texas at Austin
August 2017

Dedication

To my parents, Zhixie Yue and Yajun Lu,
for their endless love, encouragement and support

Acknowledgements

I would like to express my sincerest gratitude to my supervisor, Dr. Jon E. Olson, for his advice, support, and encouragement throughout my study in the department of Petroleum and Geosystems Engineering. He supported me to continue the Ph.D. study after I transferred major from engineering mechanics. His ingenious perspectives into the research as well as the friendly and cheerful characters were great inspirations to me. It would be impossible to complete my Ph.D. study without his helpful supervision. Furthermore, I want to express my appreciation and acknowledge Fracture Research and Application Consortium (FRAC) for providing the financial support for this study.

I would like to extend my sincere appreciation to Dr. Richard A. Schultz for his guidance and support in my projects, as well as the instructions in writing and presentation, Dr. John T. Foster, Dr. Maša Prodanović, and Dr. Julia F.W. Gale for serving on my committee and contributing insightful technical comments, Dori L. Coy and Amy D. Stewart for their help in administration and registration, and John Cassibry for the technical support.

Many thanks go to my colleagues in Dr. Olson's group for their friendship, advice, and suggestions. They include Weiwei Wang, Kan Wu, Valerie Gono, Hunjoo Lee, Tiffany Li, Andreas Michael, and Mohsen Babazadeh. I also want to thank all my friends for their pleasant company.

I would also like to thank Weatherford and Schlumberger for providing me three internships during my Ph.D. study. They were great opportunities to connect with industry and provided invaluable insights into my career development. Special thanks go to my managers, Dr. Uno Mutlu and Dr. Xiaowei Weng, and my mentors, Dr. Jian Huang, Dr. Abbas Safdar, and Dr. Mojtaba Shahri.

Last but not least, I would like to express my deepest gratitude to my family for their endless love and support.

HEIGHT CONTAINMENT OF HYDRAULIC FRACTURES IN LAYERED RESERVOIRS

Kaimin Yue, Ph.D.
The University of Texas at Austin, 2017

Supervisor: Jon E. Olson

Oil and gas production from unconventional reservoirs generally requires hydraulic fracturing within layered reservoirs, which are usually stratified with layers of different mechanical properties. Vertical height growth of hydraulic fractures is one of the critical factors in the success of hydraulic fracturing treatments. Among all the factors, modulus contrast between adjacent layers is generally considered of secondary importance in terms of direct control of fracture height containment. However, arrested fluid-driven fractures at soft layers are often observed in outcrops and hydraulic fracture diagnostics field tests. Furthermore, conventional hydraulic fracturing models generally consider planar fracture propagation in the vertical direction. However, this ideal scenario is rather unsatisfactory and fracture offset at bedding planes was widely observed in experimental testing and outcrops. Once the offset is created, the reduced opening at the offset may result in proppant bridging or plugging and may also act as a barrier for fluid flow, and thus fracture height growth is inhibited compared to a planar fracture.

In order to illustrate the effect of modulus contrast on fracture height containment, this study proposed a new approach, which is based on the effective modulus of a layered reservoir. In this study, two-dimensional finite element models are utilized to evaluate the effective modulus of a layered reservoir, considering the effect of modulus values, fracture tip location, height percentage of each rock layer, layer thickness, layer location, the number of layers, and the mechanical anisotropy. Then, the effect of modulus contrast on fracture height growth is investigated with an analysis of the stress intensity factor, considering the change of effective modulus as the fracture tip propagates from the stiff layer to the soft layer. The results show the effective modulus is mainly dependent on the modulus values, fracture tip location, and height percentage of rock layers. This study empirically derived two types of effective modulus depending on fracture tip location, namely the modified height-weighted mean and the modified height-weighted harmonic average. By combining linear elastic fracture mechanics with the appropriate effective modulus approximations, the results indicate that hydraulic fracture propagation will be inhibited by the soft layer due to a reduced stress intensity factor.

A two-dimensional finite element model was utilized to quantify the physical mechanisms on fracture offset at bedding planes under the in-situ stress condition. The potential of fracture offset at a bedding plane is investigated by examining the distribution of the maximum tensile stress along the top surface of the interface. A new fracture is expected to initiate if the tensile stress exceeds the tensile strength of rocks. The numerical results show that the offset distance is on the order of centimeters. Fracture offset is encouraged by smaller tensile strength of rocks in the bounding layer, lower horizontal confining stress and higher rock stiffness in the bounding layer, weak interface strength, higher pore pressure, lower reservoir depth, and larger fracture toughness.

Table of Contents

List of Tables

List of Figures

CHAPTER 1: INTRODUCTION

1.1 Motivation

Hydraulic fracturing has been used for decades to improve production from low permeability reservoirs. The current technology of hydraulic fracturing enables the production of oil and natural gas from shale, which had not been considered a reservoir rock from which hydrocarbon is producible. According to Energy Information Administration (EIA), hydraulic fracturing has increased shale gas production in the last decade and is expected to be the most important contributor to natural gas production in the future (Energy Information Administration, Annual Energy Outlook 2012). As predicted in Figure 1.1, shale gas is expected to account for 49 percent of the total national gas production in 2035.

In order to produce hydrocarbon from unconventional reservoirs more efficiently and economically, a better understanding of fracture geometry and propagation is needed. Among all the issues, vertical height growth of hydraulic fractures is recognized as one of the critical factors in the success of hydraulic fracturing treatments (Gu and Siebrits, 2008; Fisher and Warpinski, 2011). Cost effective hydraulic fracturing design requires fractures to access as much reservoir pay zone as possible. If the expected hydraulic fracture height growth is not achieved, a large area of pay zone will not be stimulated, which affects the ultimate production. In contrast, if hydraulic fractures grow into the adjacent rock layers which are not productive, an excessive amount of injection fluid and proppants will be wasted (Abbas et al. 2014).

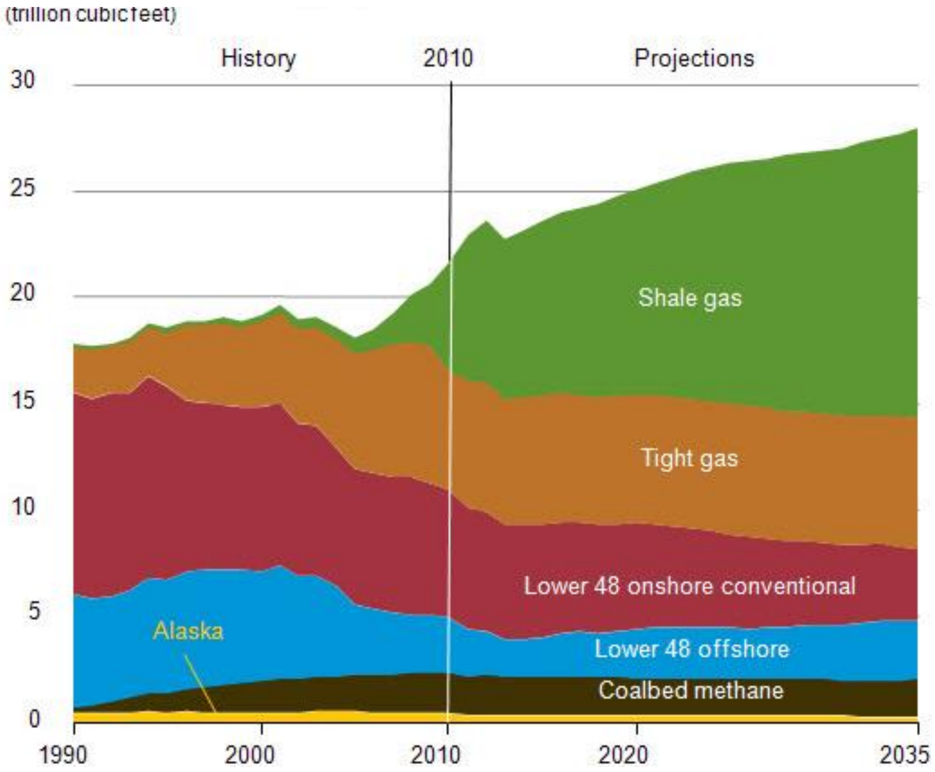

Figure 1.1. Natural gas production from 1990 to 2035 (Energy Information Administration, Annual Energy Outlook 2012).

As shown in the extensive fracture mapping database (Figure 1.2 and 1.3), hydraulic fractures are often better contained vertically than is predicted by models or conventional wisdom (Fisher and Warpinski, 2012). For instance, micro-seismic and micro-deformation data in Eagle Ford show that fracture length can sometimes exceed 300 meters, whereas fracture height is much smaller, usually measured in tens of meters (Fisher and Warpinski, 2012). In addition, fracture height is better restricted in unconventional reservoirs, which are usually stratified with layers of different mechanical properties. As shown in Figure 1.2 and 1.3, hydraulic fracture height in Eagle Ford is better contained compared to hydraulic fracture height in Barnett, which is mainly composed of siliceous mudstone (Loucks et al. 2009). However, Eagle Ford shale is a well laminated reservoir with alternating stiff carbonate rich layers and soft clay rich layers (Ferrill et al. 2014). Due to sedimentary laminations, the variation of in-situ stresses and mechanical properties of rocks in the vertical direction is more significant compared to horizontal variations, which contributes to the noticeable restriction of fracture height growth compared to the lateral propagation (Fisher and Warpinski, 2012).

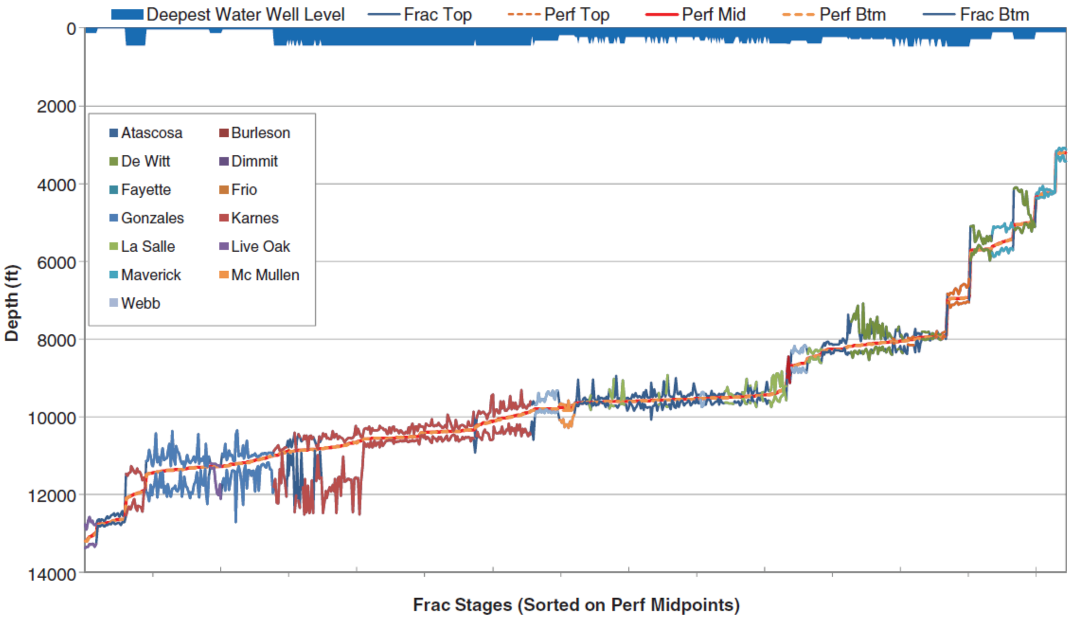

Figure 1.2. Mapped hydraulic fracture height for Eagle Ford shale. Perforation depths are illustrated by the red curve, with top and bottom illustrated by colored curves for all the mapped fracture treatments (from Fisher and Warpinski, 2012).

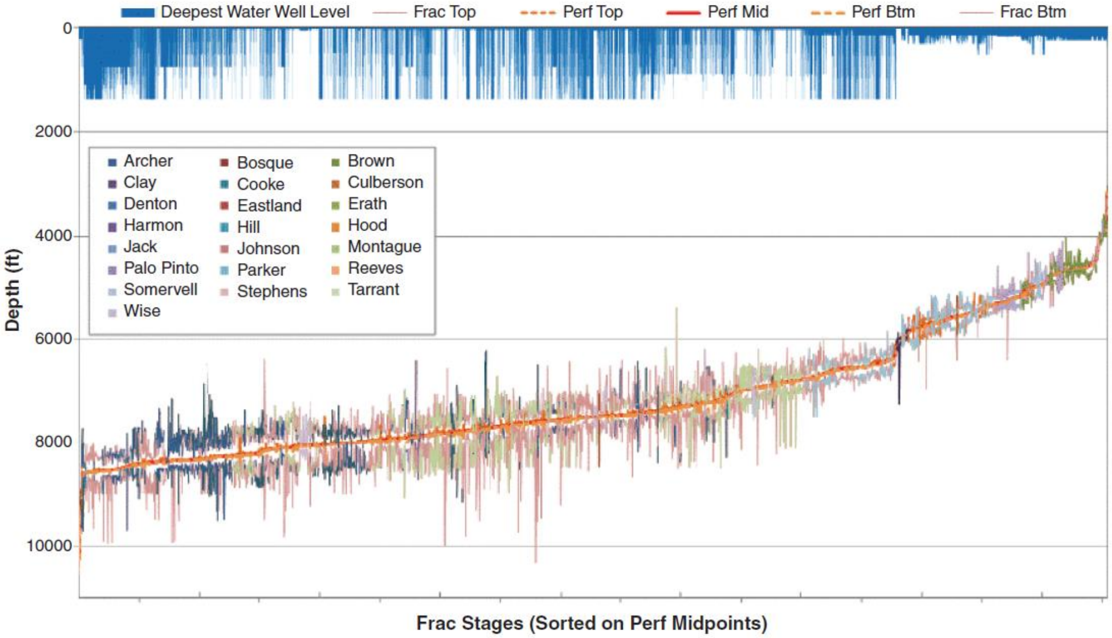

Figure 1.3. Mapped hydraulic fracture height for Barnett shale. Perforation depths are illustrated by the red curve, with top and bottom illustrated by colored curves for all the mapped fracture treatments (from Fisher and Warpinski, 2012).

Among all the factors, the variation of in-situ stresses between adjacent layers is generally considered to be the dominant mechanism for fracture height containment (Warpinski et al. 1982; Jeffrey and Bunger, 2007), whereas modulus contrast between adjacent layers is generally considered of secondary importance in terms of direct control on fracture height containment (Van Eekelen, 1982; Smith et al. 2001). However, as illustrated in Figure 1.4, arrested fluid-driven fractures at soft layers are often observed in outcrops (Philipp et al. 2013) and hydraulic fracture diagnostics field tests (Warpinski et al. 1998; Warpinski, 2011). In addition, layered modulus significantly impacts fracture width and treatment pressure, which will directly affect hydraulic fracture crossing behavior at bedding planes. Furthermore, conventional hydraulic fracture simulators either neglect modulus variation between layers or utilize over-simplified effective moduli to quantify the effect of layered modulus. However, the most common height-weighted approximation of effective modulus is not satisfactory and can lead to significant errors in calculating fracture width, as well as overall material balance and fluid efficiency (Smith et al., 2001).

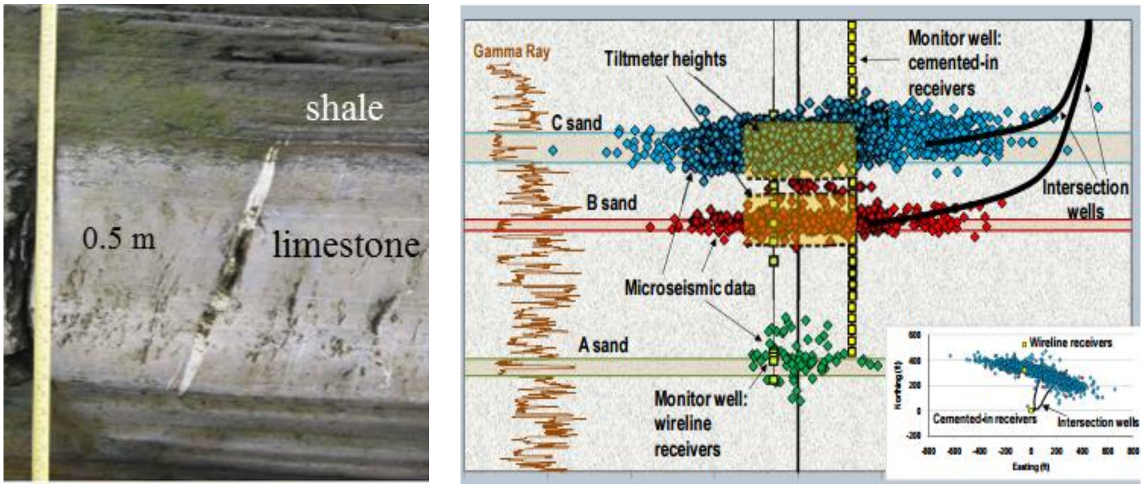

(a) (b)

Figure 1.4. (a) An arrested calcite vein in Kilve, Southwest England (Philipp et al. 2013). The calcite vein was arrested at the contact between a limestone layer and relatively soft shale layers above and below; (b) Contained hydraulic fractures within sandstone layers (Warpinski, 2011).

Furthermore, conventional hydraulic fracturing models generally consider planar fracture propagation in the vertical direction. However, this ideal scenario is rather unsatisfactory and fracture offset (Figure 1.5) at bedding planes are widely observed in experimental testing (Wang et al. 2013; Lee et al. 2015; ALTammar and Sharma, 2017) and field (Fisher and Warpinski, 2012; Philipp et al. 2013). According to numerical analysis (Zhang and Jeffrey, 2008; Abbas et al. 2014), offsets in the propagation path could contribute to fracture height containment. Once the offset is created, the reduced opening at the offset may result in proppant bridging or plugging (Daneshy, 2003). In addition, the offset may also act as a barrier for fluid flow, and thus fracture height growth is limited compared to a planar fracture. However, few studies have systematically investigated fracture offset at bedding planes, especially for hydraulic fractures under the in-situ stress condition.

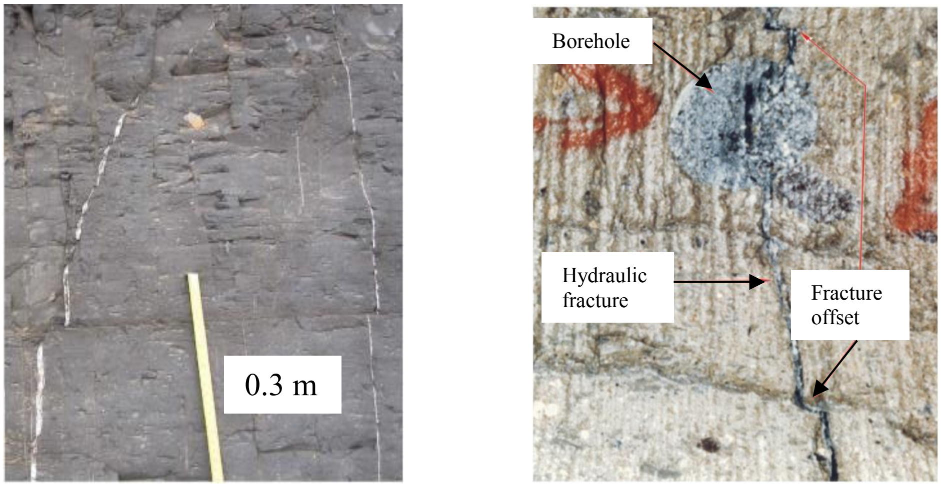

(a) (b)

Figure 1.5. (a) Calcite vein offset at a weak interface in Kilve, Southwest England (Philipp et al. 2013); (b) Mine-back photograph of hydraulic fracture offset at a weak interface (Fisher and Warpinski, 2012).

1.2 Research Objectives

A reliable and accurate estimation of fracture height growth in unconventional reservoirs is an important prerequisite to ensure the success in hydraulic fracture stimulation design. The primary objective of this dissertation is to study fundamental physics of fracture height containment. This study focuses on (1) evaluating fracture height containment due to modulus contrast between adjacent layers and (2) quantifying the physical mechanisms on fracture offset at bedding planes under the in-situ stress condition.

Because our analysis is based on the linear elastic fracture mechanics (LEFM) approach, another objective of this study is to explain the discrepancy of fracture toughness between laboratory measurements and field calibration, and to validate LEFM with the apparent fracture toughness for hydraulic fracturing analysis. The specific objectives of this dissertation are to:

i. Examine the effect of confining stress and fluid lag size on hydraulic fracture net pressure and apparent fracture toughness, and investigate the validity of LEFM with the apparent fracture toughness for hydraulic fracture modeling.

ii. Develop a new averaging method to evaluate the effective modulus of a layered reservoir, incorporating the effect of fracture tip location, modulus values, height percentage of each rock layer, layer location, the number of layers, and the in-situ stress difference between layers.

iii. Evaluate the effect of modulus contrast between adjacent layers on fracture height containment.

iv. Study fracture reinitiation at bedding planes and investigate the physical mechanisms on hydraulic fracture deflection and offset under the in-situ stress condition.

1.3 Literature Review

This section provides a review of the general background related to this dissertation, which includes hydraulic fracturing, rock fracture mechanics, layer properties of unconventional reservoirs, and fracture height containment mechanisms.

1.3.1 Hydraulic Fracturing

Hydraulic fracturing is a well stimulation technique in which rock is fractured by high pressure fluid or slurry. Hydraulic fracturing was first applied in the field in 1947 and has become a widely used technology in the last decade (George King, 2012). Now hydraulic fracturing is one of the key methods to extract unconventional oil and gas resources. According to George King (2012), over one million fracturing jobs were performed within the U.S. in 2012. Hydraulic fracturing is essential for oil and gas production from shale plays. Due to shale's low permeability, the commercial production of shale gas was impossible before the existence of slick-water fracturing. According to Energy Information Administration (Annual Energy Outlook 2012), only 1 percent of the United States natural gas production was from shale gas in 2000, but the percentage increased to 20 percent in 2010 (Figure 1.1).

Hydraulic fractures are created by pumping fracturing fluids at certain rates to increase pressure to exceed the fracture gradient of rocks at that location. Fluids injected during a fracturing job can be up to millions of gallons per well (Love 2005). Of all the fracturing fluids, slick water is the most popular. Generally, 99 percent of a slick water fracturing fluid is water and the rest is proppants and chemicals, which are mainly utilized to reduce friction. The proppants (typically sand or man-made ceramic materials) are designed to keep induced fractures open after injection.

Hydraulic fractures were generally described as simple, planar, and bi-wing fractures, propagating orthogonally to the plane of the least in-situ stress (Griggs and Handin, 1960; Perkins et al., 1961; Geertsma et al., 1969). However, mineback studies (Warpinski et al. 1982; Warpinski and Teufel, 1987; Fisher and Warpinski, 2012) and micro-seismic imaging (Warpinski et al. 1998; Warpinski et al. 2013) proved that the induced hydraulic fracture geometries are more complex than the conventional description. The complexity of the fracture geometry is mainly controlled by well orientation, in-situ stress, injection rate, fluid properties, mechanical stratigraphy, and pre-existing natural fracture system. Due to the complexity, fractures tend to be shorter and wider than those predicted by conventional models. Furthermore, Warpinski (1991) pointed out that complex fractures could cause abnormally high treatment pressure during hydraulic fracturing.

1.3.2 Rock Fracture Mechanics

Modern fracture mechanics is based on the theory of Griffith (1920), which proposed that the reduction in strain energy due to crack extension must be equal to the increase in surface energy of new fracture surfaces. However, Griffith's theory disagreed with the experiment with steel, which had to do with the plastic deformation at crack tips. In order to solve the discrepancy, Irwin (1948) and Orowan (1948) modified Griffith' theory by taking into account the plastic energy dissipation. If the plastic zone at the fracture tip is small compared to the size of the specimen (fracture length, specimen thickness, and etc.), the deformation of the body obeys the linear elastic theory except for a small zone around the fracture tip. Under the small scale yielding (SSY) condition, the body is said to undergo brittle fracture and the stress state near the fracture tip (K-dominant region) is dominated by the singular term and the other higher-order terms become negligible (Irwin, 1957). In LEFM, fracture will propagate if the stress intensity factor reaches fracture toughness, which is a material constant and describes the resistance of material against fracture (Zhu and Joyce, 2012). The stress intensity factor criterion is equivalent to the energy criterion of Griffith for elastic cracks. Fracture toughness and fracture energy are related through Irwin's formula (Irwin, 1957),

$$G = \frac{(1-v^2)K_c^2}{E} \tag{1.1}$$

where K_c is fracture toughness, E is Young's modulus, v is Poisson's ratio, and G is fracture energy.

As illustrated in Figure 1.6, depending on the relative displacement of fracture surfaces, fractures can be classified into three modes: I, II, and III (Whittaker et al., 1992). Each type of fracture has distinctive stress and displacement fields. Mode I fracture is opening mode and the relative displacement of two fracture surfaces is perpendicular to fracture surface. In general, hydraulic fractures are opening-mode fractures, propagating in planes oriented orthogonal to the minimum in-situ stress (Griggs and Handin, 1960; Perkins et al., 1961). For a mode I crack aligned along x axis in a two dimensional space, the stress state (neglecting higher order term) in the vicinity of crack tip can be expressed in terms of the stress intensity factor, which yields

$$\sigma_{xx} = \frac{K_I}{\sqrt{2\pi r}} \cos\left(\frac{\theta}{2}\right) [1 - \sin(\frac{\theta}{2})\sin(\frac{3\theta}{2})] \tag{1.2}$$

$$\sigma_{yy} = \frac{K_I}{\sqrt{2\pi r}} \cos\left(\frac{\theta}{2}\right) \left[1 + \sin\left(\frac{\theta}{2}\right) \sin\left(\frac{3\theta}{2}\right)\right] \tag{1.3}$$

$$\tau_{xy} = \frac{K_I}{\sqrt{2\pi r}} \cos(\frac{\theta}{2})\sin(\frac{\theta}{2})\cos(\frac{3\theta}{2}) \tag{1.4}$$

where *r* and θ are local polar coordinates at the crack tip, K_I is the opening mode stress intensity factor. Mode II fracture is in-plane shear mode and the relative displacement of surfaces is parallel to fracture surface, whereas Mode III refers to the anti-plane shear mode. Fractures are among the most common geologic features. The opening-mode structures include joints, veins, igneous dikes; whereas the shear-mode fractures include faults (Schultz, et al. 2008).

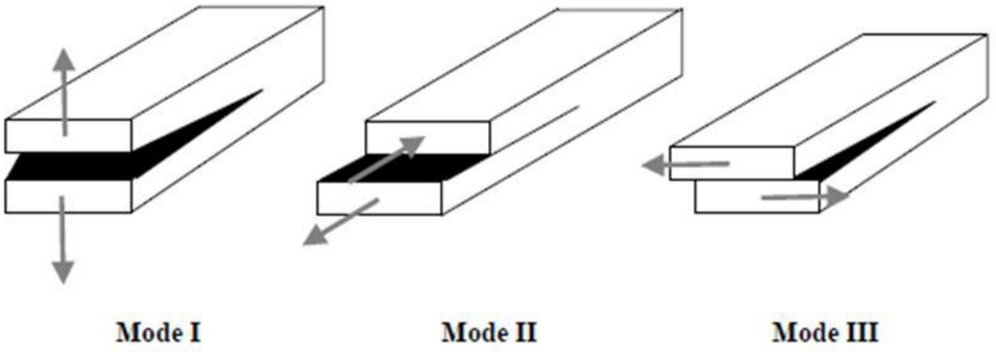

Figure 1.6. Illustration of three fracture modes (from Whittaker et al. 1992).

Figure 1.7 illustrates a typical laboratory stress-strain curve for well-cemented sandstone being deformed uniaxially (Zoback, 2007). The results show that the rock exhibits nearly linear elastic behavior for a considerable range of applied stress until a stress of about 45 MPa is reached. After the applied stress exceeds 45 MPa, the sandstone begins to deform plastically until a complete failure occurs at a stress of 50 MPa. Based on the stress magnitude and loading condition in hydraulic fracturing, most rocks (except for soft rocks such as clay or unconsolidated sandstones) exhibit in a brittle manner (Perkins and Kern, 1961). Thus, rocks are generally assumed brittle and elastic materials in hydraulic fracturing and LEFM has been applied with great success in the analysis of hydraulic fracturing (Perkins and Kern, 1961; Simonson et al. 1978; Wu and Olson, 2015). A detailed description and discussion of LEFM in hydraulic fracturing will be presented in Chapter 2.

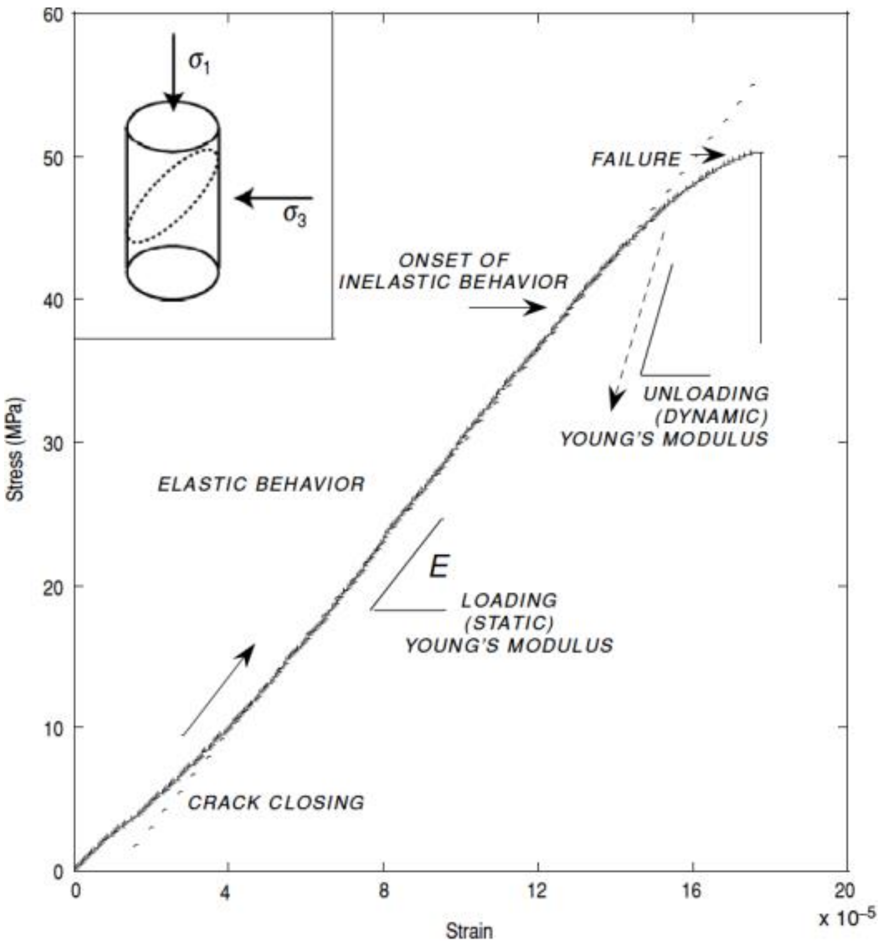

Figure 1.7. A typical stress-strain curve for well-cemented sandstone being deformed uniaxially (from Zoback, 2007).

1.3.3 Layer Properties of Unconventional Reservoirs

Hydraulic fractures in some shale plays such as Eagle Ford shale and Woodford shale exhibit little out of zone height growth and are usually well contained within the same rock stack which contains multiple rock layers (Fisher and Warpinski, 2012). However, in other relatively continuous shales such as Barnett shale, Marcellus shale and Haynesville shale, fracture growth into the adjacent rock stacks is often observed and height containment is usually poor (Curry et al. 2010). Thus, an advanced understanding of the layer properties of unconventional reservoirs is essential to evaluate hydraulic fracture height containment.

Cores, outcrops, micro-seismic data, and log profiles suggest that many unconventional reservoirs are stratified with layers of different mechanical properties (Comer, 1991; Rodrigues et al. 2009; Donovan and Staerker, 2010; Mullen, 2010; Ferrill et al. 2014; Wang and Gale, 2016; Breyer et al. 2016). For instance, Eagle Ford shale, an emerging unconventional hydrocarbon producer in south Texas, is a geological formation underlying Austin Chalk and overlying Buda Limestone (Figure 1.8). Many studies (Mullen, 2010; Martin et al. 2011; Breyer et al. 2016) characterized the petrophysical properties of Eagle Ford by investigating various log responses across the Eagle Ford play. They discovered that Eagle Ford formation is laminated with alternative carbonate and calcareous mudrock beds. As illustrated in Figure1.9, outcrops of Eagle Ford formation in Sycamore Creek pavement (located in south-central Texas) also revealed that Eagle Ford is stratified with chalk and calcareous mudrock beds (Ferrill et al. 2014).

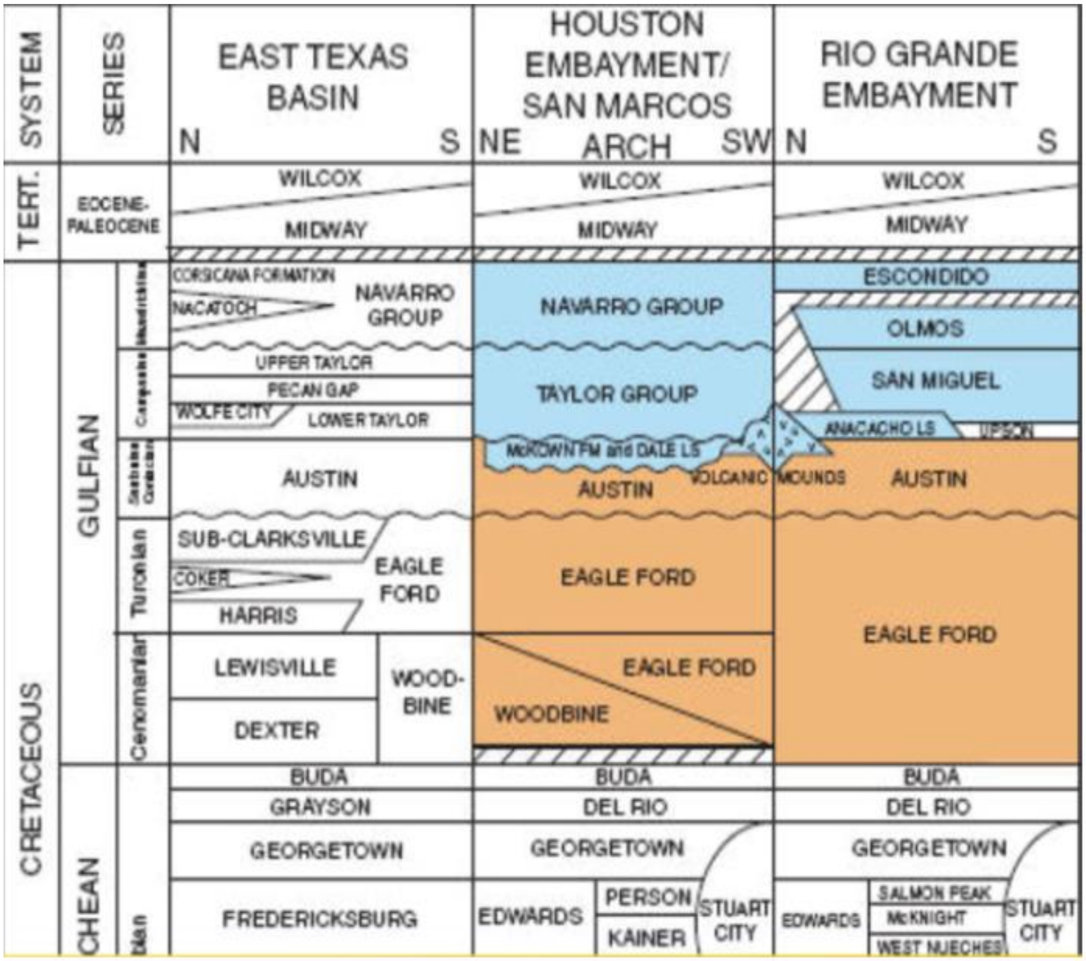

Figure 1.8. Stratigraphic column through south Texas (from Condon and Dyman, 2006).

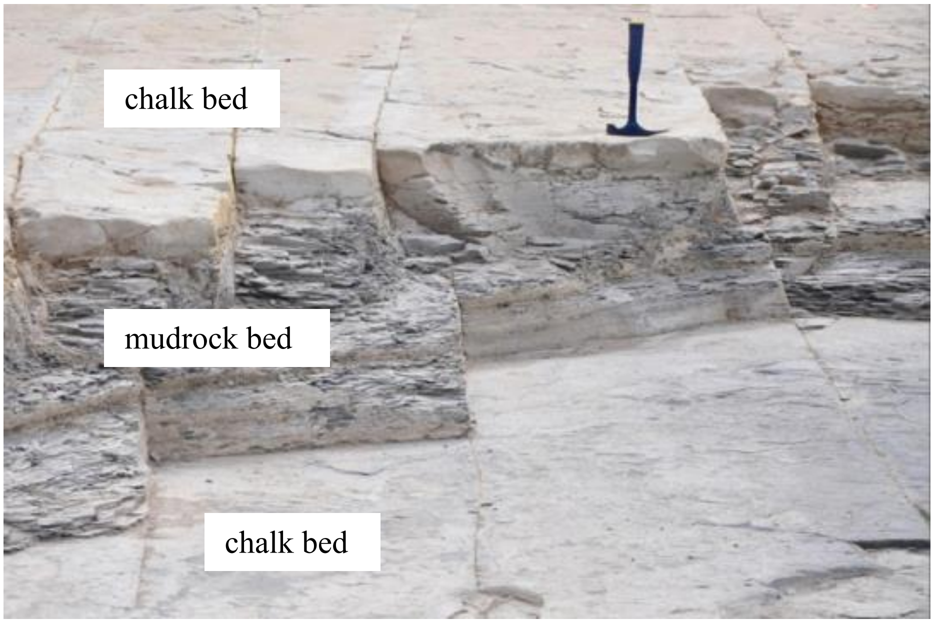

Figure 1.9. Illustration of mechanically layered rocks (succession of chalk and mudstone) at Sycamore Creek pavement, TX (from Ferrill et al. 2014).

In the outcrop of Sycamore Creek pavement, as illustrated in Figure 1.9 and 1.10, the thickness of the chalk beds ranges from 8 to 20 cm, whereas the thickness of the mudstone beds ranges from 50 to 90 cm. The results of bed thickness measured from outcrops are consistent with petrophysical characterization (Figure 1.11), from which Breyer et al. (2016) calculated that the average thicknesses of limestone and mudstone beds are 25 and 50 cm, respectively. The outcrop also revealed that gradational contact exists between chalk and mudstone beds, with vertically varying carbonate content. Variation of bed-scale compositional and textural character of Eagle Ford leads to contrasting strength and stiffness between layers. In the Eagle Ford formation, chalk beds are stiffer and stronger than mudstone beds. As illustrated in Figure 1.10, a Schmidt rebound profile shows that rebound values of mudstone beds range from 5 to 17 (R), with chalk beds having the higher rebound values, ranging from 28 to 45 (R). Based on the log and core data, Mullen (2010) also discovered that the ratio of Young's modulus between limestone and mudstone in Eagle Ford is around two. In addition, mudstone facies has higher closure stress compared to chalk facies (Mullen, 2010).

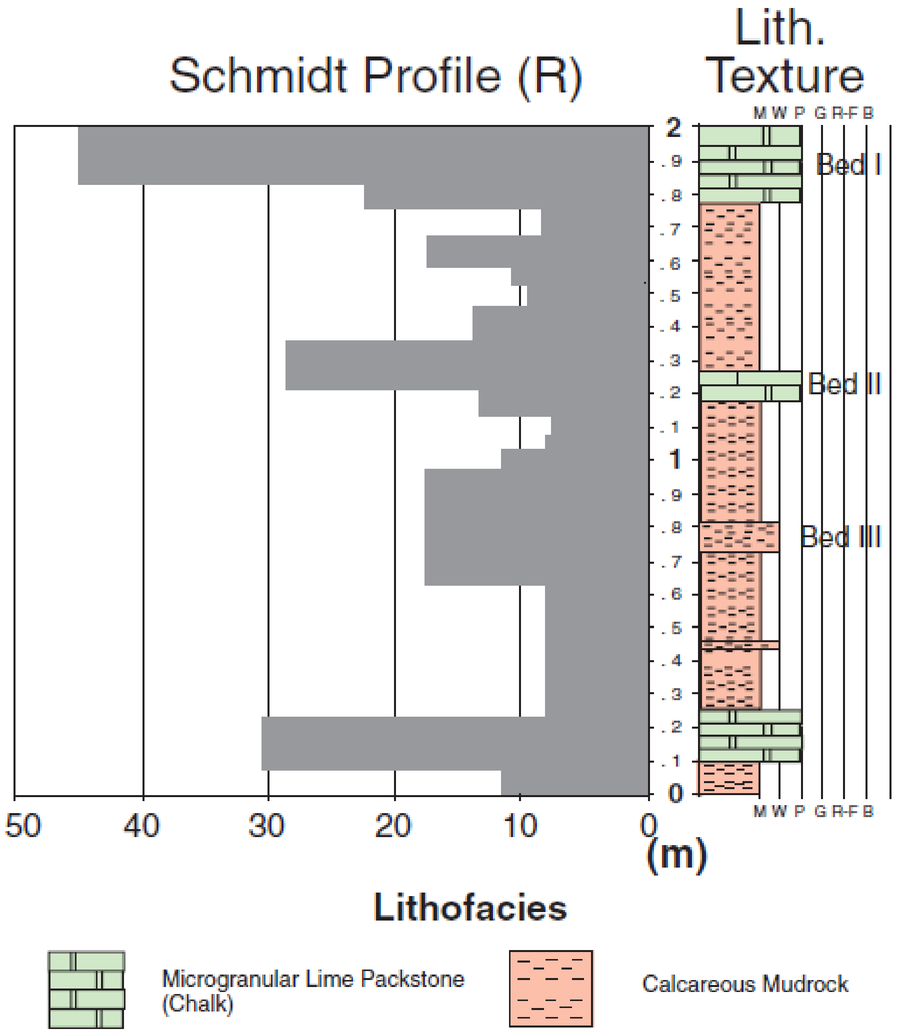

Figure 1.10. Lithostratigraphy and rebound profiles of mechanically layered chalk and mudrock beds at Sycamore Creek pavement, TX (from Ferrill et al. 2014). Chalk beds have higher rebound values than mudrock beds.

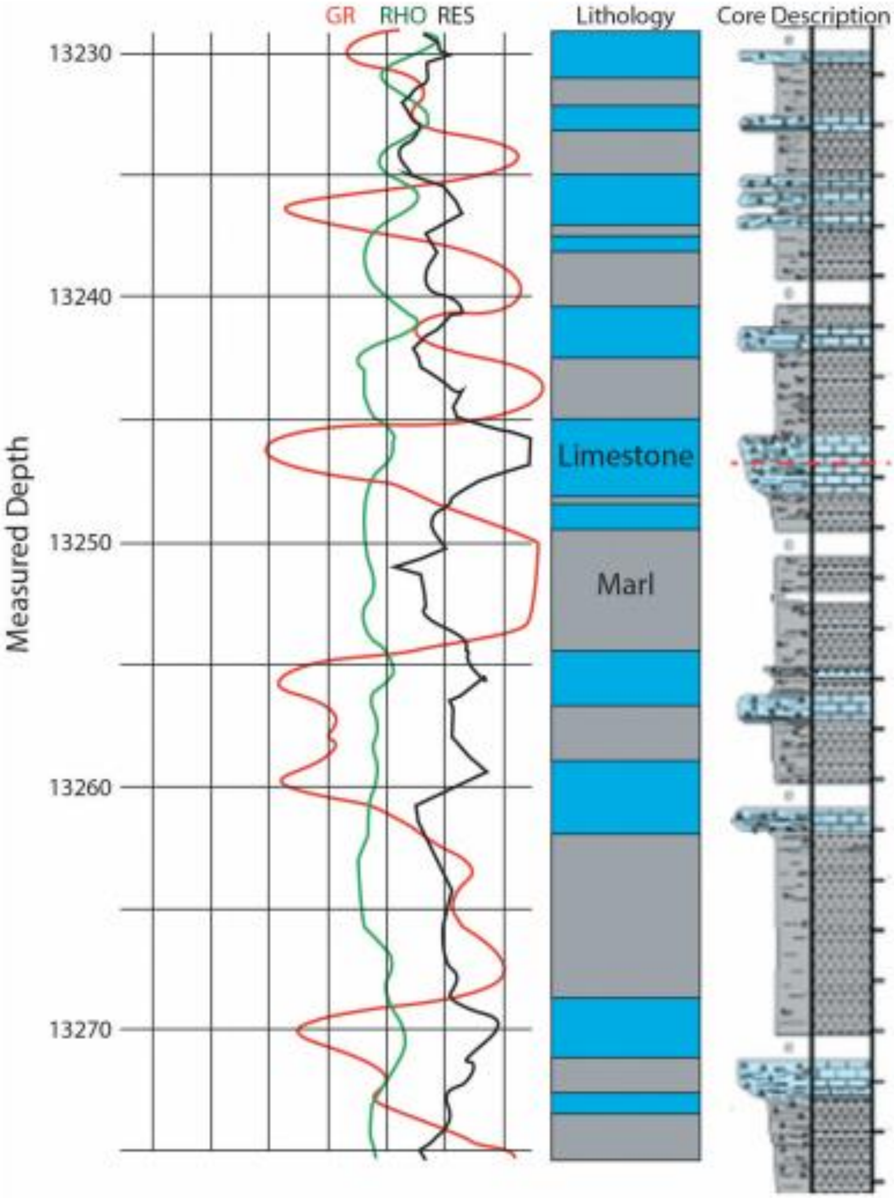

Figure 1.11. Well logs, lithology, and core description of well laminated facies in Eagle Ford formation. The average thicknesses of limestone and mudstone beds are 25 and 50 cm, respectively (from Breyer et al. 2016).

It is recognized in the modern geology that fluctuating sea level, yielding in transgression (rising-sea-level) and regression (falling-sea-level), gives rise to a vertical stratigraphic succession (Nichols, 2009). The nature of stratigraphy is mainly controlled by three factors, namely the magnitude and period of sea-level change, rate of sediment supply from land, and tectonic uplift/subsidence. For instance, the Eagle Ford formation was deposited between 94 and 88 Ma in the transition between Western Interior seaway and Gulf of Mexico basin (Ferrill et al. 2014). Eagle Ford sediments show an overall regressive sequence with a distribution of higher-frequency transgressive-regressive cycles within the formation (Donovan and Staerker, 2010; Workman, 2013; Ferrill et al., 2014). Depositional facies and sequences correlate directly to the fluctuations in sea level. High-frequency cycle transgressive deposits are relatively fine-grained calcareous mudstones, whereas the high-frequency cycle regressive deposits are relatively coarse-grained chalk (Workman, 2013).

1.3.4 Fracture Height Containment Mechanism

Hydraulic fracture propagation in the vertical direction and height containment have been extensively studied by numerical modeling (Simonson et al. 1978; Van Eekelen, 1982; Zhang et al. 2007; Gu and Siebrits, 2008; Garcia et al. 2013; Chuprakov, et al., 2014; Ouchi et al. 2017), laboratory testing (Daneshy, 1976; Teufel and Clark, 1984; ALTammar and Sharma, 2017), and mine-back tests (Warpinski et al. 1982). The results indicate that fracture geometry is complex and fracture height is mainly affected by the heterogeneities of both in-situ stresses and mechanical properties, as well as the interface strength of bedding planes.

When hydraulic fractures meet bedding planes, four types of interaction between hydraulic fractures and bedding planes, as illustrated in Figure 1.12, are usually considered (Thiercelin et al. 1987). Fractures can either penetrate through bedding planes or may be arrested at the interface due to tip blunting. Other than the above extreme cases, hydraulic fractures may be deflected into the interface or may reinitiate a new fracture at the opposite layer to form an offset pattern.

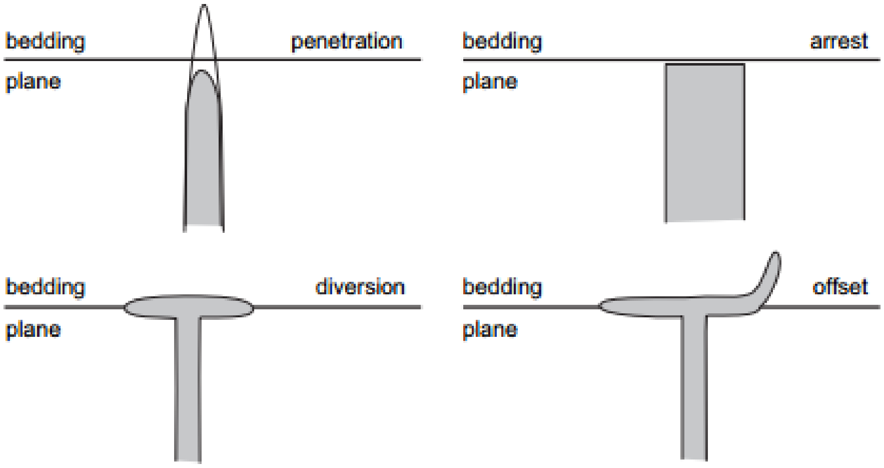

Figure 1.12. Four types of interaction between hydraulic fractures and bedding planes (from Thiercelin et al. 1987).

In this section, literature review about various mechanisms of hydraulic fracture height containment will be discussed in detail, namely in-situ stress contrast, weak interfaces, mechanical property contrast, leak-off, and treatment parameters (injection rate and fluid viscosity).

1.3.4.1 In-situ Stress Contrast between Layers

In-situ stress contrast between adjacent layers is considered to be the most important factor on fracture height containment in a layered sequence (Cleary, 1980; Warpinski et al. 1982a; Warpinski et al. 1982b; Teufel and Clark, 1984; Jeffrey and Bunger, 2007).

In order to quantify the effect of in-situ stress contrast on fracture height containment, Simonson et al. (1978) proposed a correlation between confining stress and fracture height. For a symmetric case with three layers (the confining stresses in the upper and lower layers are the same) where the pay zone is surrounded by rocks with higher stress as illustrated in Figure 1.13, the height of a pressurized fracture can be calculated based on the linear elastic fracture mechanics. The solution of fracture height in this case was first obtained by Simonson et al. (1978), as given by

$$\sigma_2 - P = \frac{2}{\pi}(\sigma_2 - \sigma_1)\, sin^{-1}\left(\frac{h}{H}\right) - \frac{K_{IC}}{\sqrt{\pi H/2}} \tag{1.5}$$

where P is the fluid pressure inside the fracture, σ_1 is the confining stress in the pay zone, σ_2 is the confining stress in the upper and lower layers, h is the height of the pay zone, H is the calculated fracture height and K_{IC} is the fracture toughness. According to equation

(1.5), fracture height is more restricted in the case of larger σ_2. The in-situ stress mechanism is effective only if there is higher stress in the confining layers.

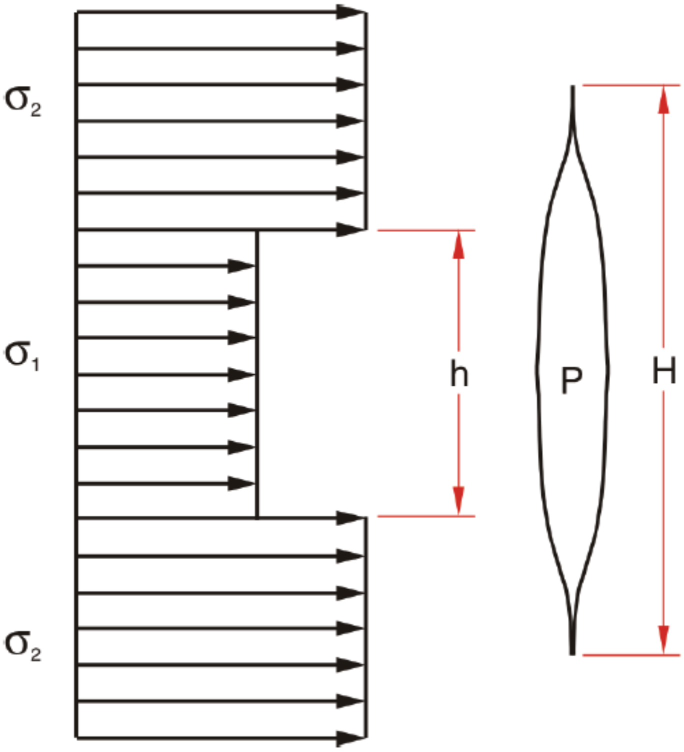

Figure 1.13. Geometry for fracture height calculation. (from Fisher and Warpinski, 2012)

1.3.4.2 Weak Interface

Hydraulic fracture geometries were conventionally modeled with the assumptions that hydraulic fractures are simple, planar, and bi-wing. In these models, in-situ stress contrast between adjacent layers is considered to dominate fracture height growth. However, as shown in the extensive fracture mapping database (Fisher and Warpinski, 2012), hydraulic fractures are often better contained vertically than those are predicted by models or conventional wisdom. Mechanisms other than in-situ stress contrast should be considered to explain the extensive fracture height containment.

Hydraulic fracturing experiments revealed that the strength of interface is essentially important to hydraulic fracture height containment (Daneshy, 1976; ALTammar and Sharma, 2017). With a weak bonding, fracture containment is possible associated with shear slip at the interface. Small scale laboratory experiments (Hanson et al. 1980) indicated that decreasing the friction at the interface reduced the tendency of fractures from propagating through the interface. The laboratory testing (Teufel and Clark, 1984) also demonstrated that hydraulic fracture propagation could be inhibited at a weak shear strength interface. At weak interfaces, fractures will be arrested or deflected into the interface due to shear slip. As a result, fracture propagation is inhibited and height is contained.

In order to incorporate shear slip and failure behavior at the interface, Barree and Winterfeld (1998) introduced an elastically decoupled shear slip model. In that model, the discontinuous fracture geometry, caused by shear slip at the interface, reduces fracture width and stress concentration at the fracture tip. The predicted fracture geometry is better matched with field observations and the model provides better height containment and higher treating pressure compared to the conventional models.

Zhang et al. (2007) also investigated propagation and deflection of a fluid-driven fracture at frictional bedding interfaces using a two-dimensional boundary element model. The frictional stress at the interface is described by the Coulomb criterion without cohesion. The results showed that fracture deflection and fluid invasion into the interface are highly dependent on the local stress state and rock deformation at the intersection point. Fluid invasion into bedding planes and formation of T-shape fractures are promoted in the case of low to medium friction strength. Furthermore, Cooke and Underwood (2001) revealed that combined sliding and opening yield fracture termination at a weak interface and offset at a moderate interface. Ouchi et al. (2017) also pointed out that fracture deflection into the interface is promoted by weak interfaces.

In order to quantify the effect of interface strength on fracture crossing behavior, Renshaw and Pollard (1995) proposed an experimentally verified criterion for fracture propagation through unbounded frictional interfaces in brittle linear elastic materials. Fractures will perpendicularly cross the interface if the following criterion is satisfied

$$\frac{1.06}{0.35+0.35\mu} > \frac{S_{yy}+T_0}{\mu S_{xx}} \tag{1.6}$$

where the interface is in the y direction, μ is the friction coefficient of the interface, S_{xx} is the remote compressive stress in the x direction, S_{yy} is the remote compressive stress in y direction, and T_0 is the tensile strength of the opposite layer. Equation (1.6) shows that shear slip is more likely to occur at small friction coefficient. This crossing criterion also agrees with bi-material interface crossing data where the modulus ratio between adjacent layers is between 0.4 and 2. In order to take into account the effect of interfacial slip in fracture geometry modeling, a novel Pseudo-three-dimensional (P3D) hydraulic fracture propagating simulator was developed by implementing Renshaw and Pollard’s criterion (Gu et al. 2008). This hydraulic fracturing simulator showed that shear slip at the interface resulted in higher fracturing pressure and better hydraulic fracture height containment.

The models mentioned above are all based on stress analysis, the interaction between fractures and interfaces can be also investigated with an energy based fracture propagation criterion, which was first proposed by He and Hutchinson (1989). Dahi-Taleghani and Olson (2011) then applied this criterion to investigate the interaction between hydraulic fractures and natural fractures. Fractures will divert into the interface if the following criterion is satisfied

$$\frac{G_\theta}{G} > \frac{G_c^{interface}}{G_c^{rock}} \tag{1.7}$$

where the interface is oriented with an angle (θ) toward the original fracture direction, G and G_θ are the energy release rates of fracture propagating in the original direction and along the interface, respectively, G_c^{rock} and $G_c^{interface}$ are the fracture energy of the rock and interface, respectively. Equation (1.7) also indicates that fracture height will be better contained due to fracture deflection at the weak interface. For a mode I crack, the left term in equation (1.7) can be expressed as (Dahi-Taleghani and Olson, 2011)

$$\frac{G_\theta}{G} = \frac{1}{2}cos^2(\frac{\theta}{2})(1 + cos(\theta)) \tag{1.8}$$

If the hydraulic fracture is orthogonally oriented relative to the interface, the ratio between G_θ and G is 0.25 (Dahi-Taleghani and Olson, 2011). Thus, fractures will be deflected into the interface if the ratio between $G_c^{interface}$ and G_c^{rock} is less than 0.25; otherwise fractures will penetrate the interface.

At the weak interface, hydraulic fracture propagation may be inhibited due to tip blunting or offset caused by lateral sliding at the interface. As discussed in the motivation section, the existence of these offsets in the propagation path may contribute to fracture height containment (Abbas, et al., 2014; Zhang and Jeffrey, 2008). After hydraulic fractures are deflected at the interface, hydraulic fracture propagation mode changes from tensile to shear. Offsets at the interface also contribute to increased injection pressure and reduced fracture width (Zhang and Jeffrey, 2006; Jeffrey et al. 2009). Once the offset is created, the reduced opening at the offset may also result in proppant bridging at the offset. In addition, the offset may also act as a barrier for fluid flow which requires higher treating pressure.

In conclusion, fracture height growth is considerably affected by interface properties. Moreover, the weak interface mechanism is considered to be the most important factor on hydraulic fracture height containment in shallow depth or over-pressurized reservoirs where the friction at bedding planes is not sufficient to resist interface sliding (Warpinski et al. 1982; Teufel and Clark, 1984; Cooke and Underwood, 2000; Fisher and Warpinski, 2012). At deep depth, shear slip at the interface will be inhibited due to the friction caused by large overburden stress. However, Daneshy (2009) pointed out that tip blunting at the interface and subsequent fracture height containment might occur at any depth because of the existing shear stress at the interface, which is caused by mechanical property difference between layers.

1.3.4.3 Mechanical Property Contrast between Layers

Mechanical property contrast between adjacent layers is usually not considered to be a direct control on fracture height containment. In general, fracture height growth could be influenced by mechanical property contrast between adjacent layers in four ways.

The first possible effect on height containment was proposed by Simonson et al. (1978) with an analysis of the stress intensity factor at the crack tip as the fracture approaches the interface. His study showed that the stress intensity factor at the fracture tip starts to change as the tip approaches the interface between two dissimilar elastic materials. If the opposite material is stiffer, the stress intensity factor approaches to zero as the tip gets closer to the interface. Thus, the opposite material acts as a perfect barrier to prevent fracture from penetration. However, this rigorous fracture mechanics solution requires a geological rare 'sharp' boundary at the interface (Smith et al. 2001). In fact, numerous experimental studies (Daneshy, 1978; Teufel and Clark, 1984) and mine-back testing (Warpinski et al. 1982a, b) demonstrated that hydraulic fractures can cross the interface from a low-modulus material to a high-modulus material.

The second effect of mechanical properties on fracture height containment is related with fracture width changes, which can be critical to fluid flow, proppant transportation, and net pressure. It was initially believed that hydraulic fracture penetration into the outer layer is inhibited if the outer layer is stiffer (Van Eekelen, 1982). Based on Van Eekelen's analysis, the fracture width in stiffer layers where fractures propagate into will be narrower. This then reduces fluid flow into fracture tip in the stiff layers, and finally, reduces the rate of fracture height growth. However, the analysis of Gu and Siebrits (2008) showed a contrary result. According to their analysis, using a pseudo 3D hydraulic fracture simulator coupled with fluid flow, low modulus outer layer does not enhance but hinder fracture growth and the fracture height is larger if the outer layer is stiffer. According to Gu and Siebrits (2008), the main reason of this discrepancy is that fluid pressure is dependent on the coupling effect of fracture width and fluid flow rate in their analysis but a constant fluid pressure is assumed in Van Eekelen's analysis. Based on their results and other earlier studies, Gu and Siebrits (2008) concluded that a stiff layer might hinder fracture propagation before the fracture tip reaches the interface but a soft layer hinders fracture propagation after the fracture tip is already inside the soft layer.

The third effect is related to fracture toughness contrast between adjacent layers. Fracture toughness is a measurement of the resistance of a material to crack extension. Given other properties being equal, it is more difficult for fractures to grow in a material with larger fracture toughness. Numerical analysis (Thiercelln et al. 1989; Garcia et al. 2013) showed that fracture toughness has a significant effect on fracture height growth. Ouchi et al. (2017) also investigated the effect of fracture toughness on fracture height containment using a peridynamics numerical model, which was comprised of a detailed near-interface small-scale domain. The results indicated that the variation of fracture toughness contrast between adjacent layers can lead to three types of propagation behaviors at the interface, namely fracture crossing, turning, and branching. In general, the fracture propagates straight across the interface when there is low fracture toughness contrast, whereas the fracture is deflected into the interface when the ratio of fracture toughness between the bounding layer and pay zone is high. The critical ratio of toughness for fracture turning is dependent on the principal stress difference (the difference between the overburden stress and minimum horizontal stress): a fracture toughness ratio of two to four is necessary for fracture turning under a low principal stress difference (less than 1 MPa), whereas about eight to ten times fracture toughness contrast is necessary for a high principal stress difference (about 20 MPa). However, according to the measured values of fracture toughness for various rocks (Van Eekelen, 1982), fracture toughness is on the order of 1 MPa$\sqrt{m}$ and the range is narrow. Moreover, in-situ fracture toughness is difficult to measure and the value is dependent on fracture size, confining pressure and fluid (Thiercelln et al. 1989).

The fourth possible mechanism of hydraulic fracture height containment due to mechanical property contrast is related to the effect of mechanical properties on stress concentration. Philipp et al. (2013) investigated the tensile stress distribution near the fracture tip for a layered sequence. The results showed that high tensile stress was concentrated at the stiff layers and the tensile stress in the soft layers was relatively much lower. The results indicate that hydraulic fractures are more likely to be arrested in the soft layers if the tensile stress propagation criterion was favored.

In conclusion, it is difficult to quantify the direct effect of mechanical property contrast on fracture height containment. However, the effect of material properties can be significant on fracture height containment indirectly through the influence on net pressure, width profile, and stress distribution. More importantly, Differences in the mechanical properties can contribute to the contrast of in-situ stress among layers. In a stratified formation, layers expand horizontally due to the overburden stress. For the same lateral strain, the stress concentration in stiff layers will be greater than that in soft layers (Teufel and Clark, 1984). As a result, in-situ stresses at different layers are different due to the mechanical property contrast.

1.3.4.4 Leak-off

Shear activation of mineralized interface greatly enhances fluid conductivity of bedding planes (Olsson and Brown, 1993). The contact between hydraulic fractures and conductive bedding planes contributes to fluid flow into the interface and causes fluid leak-off from the main hydraulic fracture. In order to study the effect of interfacial leak-off, Chuprakov (2015) provided a numerical solution of fracture height growth based on the distribution of interfacial leak-off along the bedding planes. The results showed that fracture height is better contained due to fluid leak-off into the bedding planes.

Since leak-off has a strong impact on fracture propagation in highly permeable formations, fracture height growth is also affected by fluid loss due to leak-off into the high permeability formations. Laboratory testing and numerical analysis were utilized to test fracture propagation through layers with different permeability in order to investigate fracture height containment due to leak-off (De Peter and Dong, 2009). The experimental results show that fractures may be strongly contained by layers with high permeability. The numerical results also indicate that the fracture tip in the highly permeable formations tends to close due to fluid leak-off.

1.3.4.5 Treatment Parameters

In recent numerical studies (Chuprakov, et al., 2014; Chuprakov, 2015), the OpenT model was developed to examine the effect of fluid viscosity on fracture crossing behavior at geological discontinuities, such as bedding planes and natural fractures. The results showed that fluid viscosity has been identified to be an important factor on hydraulic fracture crossing scenario at natural fractures. Increasing fluid viscosity contributes to fracture crossing at natural fractures. Kresse et al. (2013) also showed that the simulated rock volume and fracture network could be quite different due to the change of fluid viscosity. Fracture network is more complex in the case of low fluid viscosity other than high fluid viscosity.

The effect of injection rate on fracture crossing at natural fractures has been also taken into account in the OpenT model (Chuprakov, et al., 2014; Chuprakov, 2015). The change of pumping rate can not only affect fluid pressure, fracture width, the local stress state, and fracture footprint, but also the fracture crossing behavior at natural fractures. Kresse et al. (2013) showed that the generated hydraulic fracture networks can be quite different with different injection rates. More complex fracture network will be expected with higher injection rate.

1.4 Dissertation Outline

This dissertation contains five chapters.

Chapter 1 primarily presents the motivation and objectives of this dissertation. This chapter also reviews the general background of hydraulic fracturing, rock fracture mechanics, layer properties of unconventional reservoirs, and fracture height containment mechanisms.

Chapter 2 employs Dugdale-Barenblat (DB) cohesive zone model to evaluate the effect of confining stress and fluid lag size on net pressure and apparent fracture toughness. In addition, the near-tip stress state and fracture energy of LEFM with the apparent fracture toughness are compared to the DB model to demonstrate the validity of LEFM approach for hydraulic fracture analysis.

Chapter 3 discusses the effect of modulus contrast between adjacent layers on hydraulic fracture height growth. First, we develop a new averaging method to quantify the effective modulus of a layered reservoir by comparing to the effective modulus which is determined from finite element method. Then, we apply the derived averaging modulus to evaluate the change of net pressure and stress intensity factor when a hydraulic fracture propagates from a stiff layer to a soft layer. Fracture height growth is evaluated if the stress intensity factor exceeds fracture toughness.

Chapter 4 utilizes LEFM to study hydraulic fracture offset at bedding planes under the in-situ stress condition. The potential of fracture offset is investigated by examining the distribution of the maximum tensile stress along the top surface of bedding planes. A new fracture is expected to reinitiate if the tensile stress exceeds the tensile strength of rocks. Various factors on fracture offset are investigated: in-situ stress and modulus contrast between adjacent layers, interface strength, reservoir depth, pore pressure, and fracture toughness.

Chapter 5 draws the conclusions of this dissertation and provides recommendations for future research plan.

CHAPTER 2: MODIFICATION OF FRACTURE TOUGHNESS BY INCORPORATING THE EFFECT OF CONFINING STRESS AND FLUID LAG

2.1 Introduction

Linear Elastic Fracture Mechanics (LEFM) has been applied to investigate fracture initiation and propagation in solid mechanics (Irwin, 1957; Rice, 1968) and rock mechanics problems (Delaney and Pollard, 1981; Olson, 2003; Wu and Olson, 2015). In LEFM, fracture will propagate if the stress intensity factor reaches fracture toughness, which describes the resistance of material against fracture (Zhu and Joyce, 2012). The stress intensity factor criterion is equivalent to the energy criterion of Griffith (1920) for an elastic crack in a perfectly brittle material. Fracture toughness and fracture energy are related through Irwin's formula (equation (1.1)).

LEFM is applicable under the small scale yielding (SSY) condition, in which the fracture process zone is small compared to the size of the specimen (fracture length, specimen thickness, and etc.). Under the condition of SSY, most of the body deforms elastically and the stress state near the fracture tip (K-dominant region) is dominated by the singular term and the other higher-order terms become negligible. However, real materials cannot withstand infinite stress, and it deforms inelastically in the vicinity of the fracture tip.

If fracture toughness is a material constant, as it is assumed in LEFM, the value of fracture toughness is independent of loading conditions. However, experimental results (Schmidt and Huddle, 1976; Thiercelin, 1987; Guo et al. 1993; Al-Shayea et al. 2000) showed that fracture toughness is not a material constant but the value of fracture toughness increases with the confining stress. For instance, the measured fracture toughness of Indiana limestone increases from 0.93 to 4.2 $\mathrm{MPa}\sqrt{\mathrm{m}}$ as the confining pressure increases from atmosphere pressure to 62 MPa (Schmidt and Huddle, 1976). Moreover, the fracture toughness calibrated from hydraulic fracturing treatments (Shlyapobersky, 1985) and displacement-length scaling of dikes, joints, and veins (Delaney and Pollard, 1981; Olson, 2003; Schultz et al. 2008) is usually one to two orders of magnitude greater than the values obtained from conventional laboratory tests. The high value in-situ fracture toughness might be attributed to scaling effect, confining stresses, and plasticity near the fracture tip (Papanastasiou, 1999).

Rubin (1993) demonstrated that fracture toughness is not a material constant but depends on the crack size and loading conditions when the confining pressure exceeds the tensile strength of the rock. The singular term is not a good measurement of the stress state near the crack tip when the confining stress exceeds the material’s tensile strength. Johnson and Cleary (1991) also pointed out that the net pressure required for hydraulic fracture propagation is greater than the value predicted by the standard LEFM model using the fracture toughness from laboratory measurement. Due to the limitation of LEFM, cohesive zone model (CZM) has been proposed to explain the discrepancies between the field observation and LEFM (Rubin, 1993; Khazan and Fialko, 1995;

Papanastasiou, 1999). In the CZM approach, the estimated fracture toughness is not recognized as a material constant but can be subjected to loading conditions. Moreover, fracture tip effects related to fluid lag (where fracture tip is not penetrated by fracturing fluid) and nonlinear rock deformation can be lumped to the apparent fracture toughness (Rubin, 1993).

In this study, a Dugdale-Barenblat (DB) cohesive zone model is utilized to establish the contributions of fluid lag and confining stress on net pressure and the apparent fracture toughness of fluid-driven fractures. Then, by comparing the near-tip stress state and fracture energy, this study shows that LEFM applies for fluid-driven fractures with the existence of fluid lag under confining stress if the apparent fracture toughness is utilized.

2.2 Dugdale-Barenblat Model without Fluid Lag

Cohesive zone models have been applied to avoid singularity at fracture tip and to consider the inelastic deformation ahead of the fracture tip. In rocks, the cohesive zone may consist of micro cracks, crushed grains, and etc. (Jaeger and Cook, 1979). In this regard, Dugdale (1960) and Barenblat (1962) proposed a model with a small cohesive zone ahead of the fracture tip where the internal stress resists fracture surfaces from separation. In DB model, the cohesive stress is assumed to be constant when the separation between fracture surfaces is smaller than the critical value δ_c, which is determined by

$$\delta_c = \frac{G}{\sigma_c} \tag{2.1}$$

where σ_c is the cohesive stress, which is generally identified as the tensile strength of rocks. According to Jaeger and Cook (1979), the tensile strength of many types of rocks varies between 5 and 15 MPa. Furthermore, four-point beam tests under confining pressure (Weinberger et al. 1994) showed that tensile strength depends only slightly on confining stress and the tensile strength for various rocks is on the order of 5 MPa. In addition, fracture energy of rocks is on the order of 1 J/m^2 (Rubin, 1993). By considering the tensile strength and fracture energy as approximately 5 MPa and 1 J/m^2, respectively, the value of the critical opening is estimated on the order of 0.02 mm according to equation 2.1. In this study, the critical opening and tensile strength are considered as material constant.

Figure 2.1a shows the configuration of the near-tip region of cracks using DB model subjected to remote tensile stress T. In the DB model, a constant cohesive stress σ_c is acting at the cohesive zone of length R_c to prevent fracture surfaces from separation. The fracture will start to propagate when the fracture opening at the end of cohesive zone (x = 0) is equal to the critical value δ_c. In the DB model, the length of cohesive zone is determined by the requirement that there is no singularity at the tip of cohesive zone (neglecting terms of order R_c/l)

$$T\sqrt{l} - \frac{\sqrt{8}}{\pi}\sigma_T\sqrt{R_c} = 0 \tag{2.2}$$

where l is the fracture half-length, R_c is the length of cohesive zone, and σ_T is the tensile strength. The critical fracture opening at the end of cohesive zone can be expressed in terms of the tensile strength, elastic modulus, and cohesive zone length as (Rubin, 1993)

$$\delta_c = \frac{8(1-v^2)}{\pi E} \sigma_T R_c \tag{2.3}$$

where E is Young's modulus and v is Poisson's ratio. The length of cohesive zone can be determined based on equation (2.3) as

$$R_c = \frac{\pi E \delta_c}{8(1-v^2)\sigma_T} \tag{2.4}$$

Noting that the tensile strength is approximately 5 MPa, the value of the critical fracture opening is on the order of 0.02 mm, and plane strain Young's modulus $\frac{E}{1-v^2}$ is assumed 10 GPa, the process zone size at zero confining condition is therefore on the order of 0.0157 m. The result indicates that cohesive zone size is independent of loading condition and fracture length when the cohesive zone size is negligible compared to fracture length. In LEFM, fracture will propagate when the stress intensity factor reaches fracture toughness, which is defined in terms of remote tensile stress and fracture half-length,

$$K_c = T\sqrt{\pi l} \tag{2.5}$$

By substituting equation (2.5) to equation (2.2), fracture toughness can be determined based on the cohesive model parameters and expressed as

$$K_c = \sqrt{\frac{8}{\pi}} \sigma_T \sqrt{R_c} = \sqrt{\frac{E\delta_c \sigma_T}{(1-v^2)}} \tag{2.6}$$

Equation (2.6) indicates that fracture toughness is a material constant and independent of loading condition if the fracture is under remote tensile stress. Based on the parameters of DB models for rocks, the fracture toughness is on the order of 1 MPa$\sqrt{\text{m}}$, which is in good agreement with the values measured from experiments (Roegiers and Zhao, 1991; Schmidt and Huddle, 1997).

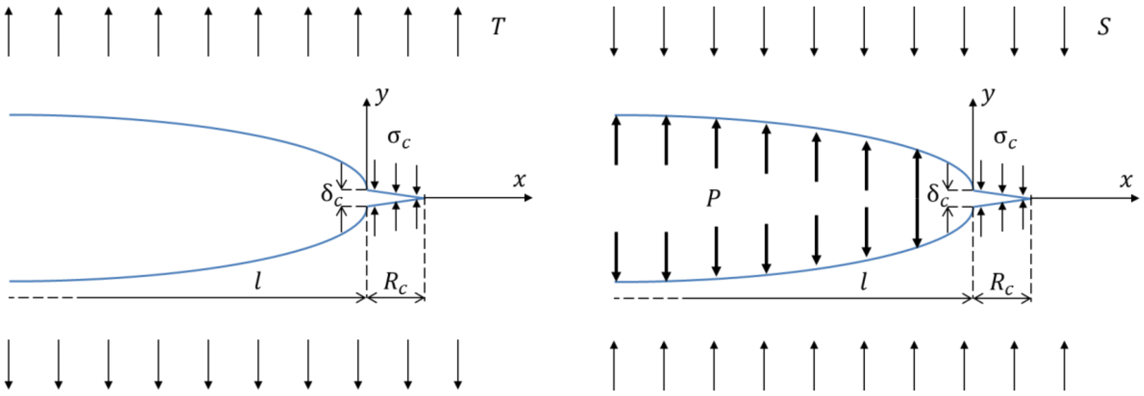

(a) (b)

Figure 2.1. Configurations of near-tip regions of cracks in DB model: (a) a crack under uniform remote tensile stress T with the cohesive length of R_c and (b) a crack subjected to ambient compressive stress S and internal pressure P. (R_c is the length of cohesive zone and $\delta_c$is the opening at the end of cohesive zone)

DB model was initially proposed to account for nonlinear fracture behavior in solid mechanics, in which the loading conditions are close to Figure 2.1a, and then Rubin (1993) applied DB model to investigate fractures under confining stress. Figure 2.1b shows the configuration of a crack subjected to ambient confining stress and internal pressure in DB model. In that case, a constant fluid pressure P is applied on the fracture surface to open the crack and fluid front is coincidence with the end of cohesive zone ($x =$

0). A compressive stress S is applied as in-situ stress to resist fracture from opening. There is also a constant cohesive stress σ_c acting on the cohesive region, which is located between $x = 0$ and $x = R_c$. In order to eliminate the singularity at the tip of cohesive zone, the stress intensity factor should be zero at that point. The condition for absence of singularity at the crack tip can be written as

$$\int_{-l}^{l}(P-S)\sqrt{\frac{l+R_c-t}{l+R_c+t}}dt-\int_{-(l+R_c)}^{-l}(S+\sigma_T)\sqrt{\frac{l+R_c-t}{l+R_c+t}}dt-\int_{l}^{(l+R_c)}(S+\sigma_T)\sqrt{\frac{l+R_c-t}{l+R_c+t}}dt=0 \quad (2.7)$$

where t is the position along fracture. After the integration, equation (2.7) can be simplified as

$$(P-S)\arcsin(x)-(S+\sigma_T)\arccos(x)=0 \quad (2.8)$$

where $x = l/(l + R_c)$. In the case of negligible cohesive zone size compared to the fracture half-length ($R_c \ll l$), equation (2.8) can be rewritten as

$$(P-S)\sqrt{l}-\frac{\sqrt{8}}{\pi}(P+\sigma_T)\sqrt{R_c}=0 \quad (2.9)$$

Moreover, when fracture starts to propagate, fracture opening at the end of cohesive zone ($x = 0$) should be equal to the critical opening δ_c, which gives (Khazan and Fialko, 1995)

$$\delta(0)=\frac{8(1-v^2)}{\pi E}(l+R_c)(P+\sigma_T)x\ln\frac{1}{x}=\delta_c \quad (2.10)$$

In the case of negligible cohesive zone size ($R_c \ll l$), equation (2.10) becomes

$$\delta(0)=\frac{8(1-v^2)}{\pi E}(P+\sigma_T)R_c=\delta_c \quad (2.11)$$

Based on equation (2.11), the length of cohesive zone can be calculated as

$$R_c=\frac{\pi}{8}\frac{E}{(1-v^2)}\frac{\delta_c}{(P+\sigma_T)} \quad (2.12)$$

In LEFM, fracture toughness is defined in terms of fracture net pressure and fracture half-length. From equation (2.9) and (2.12), the apparent fracture toughness can be written as

$$K_c = (P - S)\sqrt{\pi l} = \sqrt{\frac{1}{\pi}\frac{E}{(1-v^2)}(P + \sigma_T)\delta_c} \tag{2.13}$$

According to equation (2.9) and the assumption $R_c \ll l$, it is evident that the net pressure $(P - S)$ is negligible compared to the internal fluid pressure P, thus the internal fluid pressure P can be approximated as confining pressure S. As a result, the length of cohesive zone and apparent fracture toughness can be also expressed in terms of confining stress as (Rubin, 1993; Khazan and Fialko, 1995)

$$R_c = \frac{\pi}{8}\frac{E}{(1-v^2)}\frac{\delta_c}{(S+\sigma_T)} \tag{2.14}$$

$$K_c = \sqrt{\frac{1}{\pi}\frac{E}{(1-v^2)}(S + \sigma_T)\delta_c} \tag{2.15}$$

Jaeger and Cook (1979) stated that elastic modulus is nearly independent of the confining stress. As a result, equation (2.14) indicates that the size of process zone decreases as confining pressure increases. It is also evident from equation (2.15) that fracture toughness is not a material constant, and instead it increases with confining stress for fractures under remote compression.

The increase of fracture toughness in terms of confining stress measured in the laboratory (Schmidt and Huddle, 1997; Roegiers and Zhao, 1991) could be explained by using the DB model illustrated in Figure 2.1b. In this case, the apparent fracture toughness can be obtained from equation (2.15), which is expressed in terms of confining stress. The fracture toughness, tensile strength, and elastic moduli of Indiana limestone

(Schmidt and Huddle, 1997) and Berea sandstone (Roegiers and Zhao, 1991) are listed in Table 2.1. Based on equation (1.1) and (2.1), the critical opening of Indiana limestone and Berea sandstone are estimated to be 0.006 mm and 0.05 mm, respectively. Then, the apparent fracture toughness can be expressed in terms of confining stress based on equation (2.15). The comparison between experimental measurements of fracture toughness and calculated fracture toughness based on equation (2.15) is illustrated in Figure 2.1.

Table 2.1. Mechanical properties of Indiana limestone and Berea sandstone

(* from Schmidt and Huddle (1977), + from Roegiers and Zhao (1991), # from Weinberger et al. (1994))

Rock type	Fracture toughness (MPa$\sqrt{m}$)	Tensile strength (MPa)	Young's modulus (GPa)
Indiana limestone	0.93^*	$5.3^{\#}$	$26.6^{\#}$
Berea sandstone	1.36^+	$3.5^{\#}$	$10.2^{\#}$

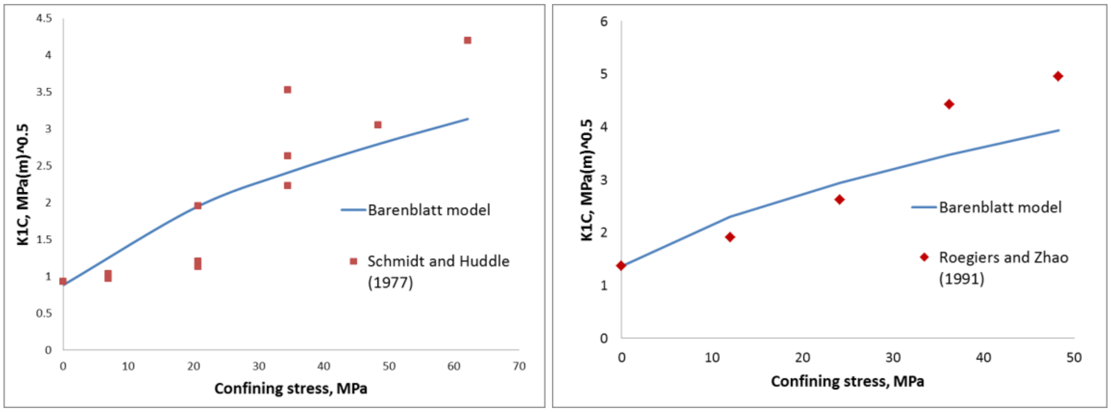

(a)

(b)

Figure 2.2. Comparison of fracture toughness estimated by the DB model and laboratory measurements of (a) Schmidt and Huddle (1997) and (b) Roegiers and Zhao (1991) under various confining stresses.

2.3 Dugdale-Barenblat Model with Fluid Lag

As indicated by the DB model, the apparent fracture toughness increases with confining stress. However, the estimated value is still one order of magnitude lower than the fracture toughness calibrated from the field data (Delaney and Pollard, 1981; Shlyapobersky, 1985; Olson, 2003; Schultz et al. 2008). In order to solve this discrepancy, the consideration of fluid lag in CZM has been proposed to investigate fluid-driven fractures under the in-situ condition (Jeffrey, 1989; Rubin, 1993; Khazan and Fialko 1995; Garagash, 2006).

In fact, fluid lag has been observed in both hydraulic fracturing experiments (Groenenboom and Van Dam, 2000; Bunger et al. 2005) and mine-back studies (Warpinski, 1985). Groenenboom and Van Dam (2000) obtained the geometry and configuration of fracture tip during hydraulic fracture propagation by using time-lapse ultrasonic measurements. Their results indicated that fracture tip is not penetrated by fluid. In mine-back studies, Warpinski (1985) also discovered that fluid front does not reach the fracture tip. As illustrated in Figure 2.3 (Bunger et al. 2005), fluid front and fracture tip location are directly characterized from video images by measuring the intensity of light transmitted through fracture surfaces. Based on the crack tip behavior, Bunger et al. (2005) concluded that fluid viscosity plays an important role in determining the near-tip fracture opening as well as the fluid lag length. As a result, fluid lag effect might be significant and must be included to better understand crack tip behavior in addition to the net pressure and geometries of hydraulic fractures.

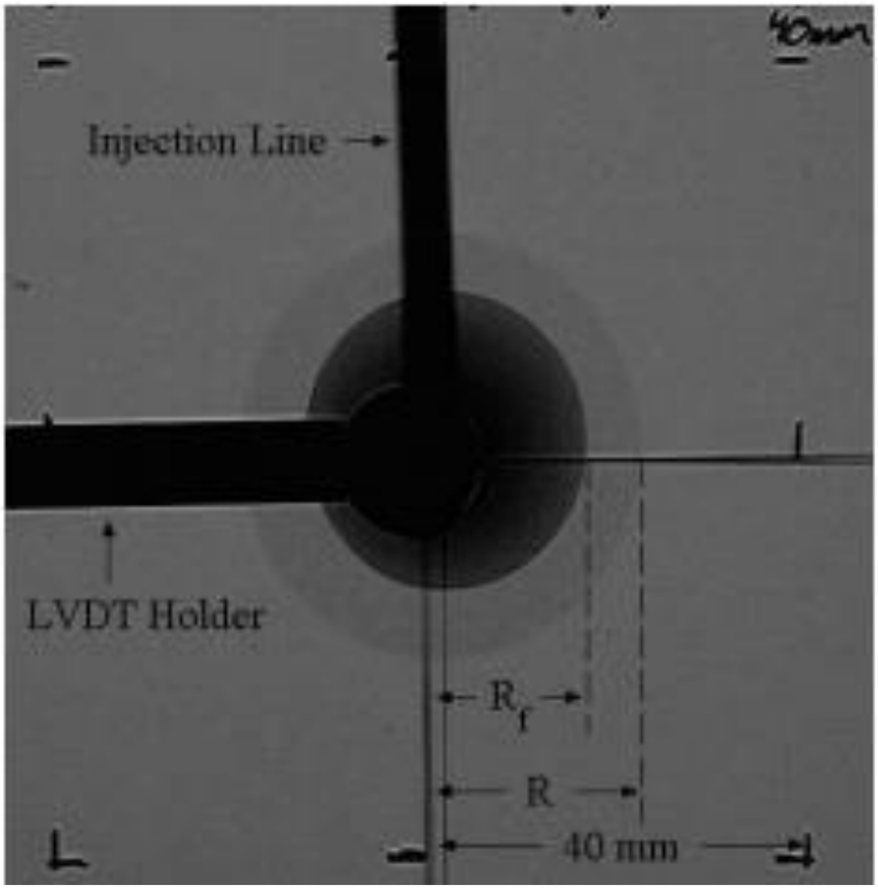

Figure 2.3. Image of fluid front and tip location during hydraulic fracture propagation (from Bunger et al. 2005). R_f is the radius of fluid-filled region, whereas R is fracture radius.

Figure 2.4 shows the configuration of DB model with dry tip region under confining pressure. The only difference between models in Figure 2.4 and Figure 2.1b is that there exists an unwetted zone with length R_f between fluid front and cohesive zone in

Figure 2.4. Depending on rock permeability, the internal pressure acting on the fracture surface of unwetted zone is considered either zero (Rubin, 1993) or pore pressure (Detournay and Garagash, 2003).

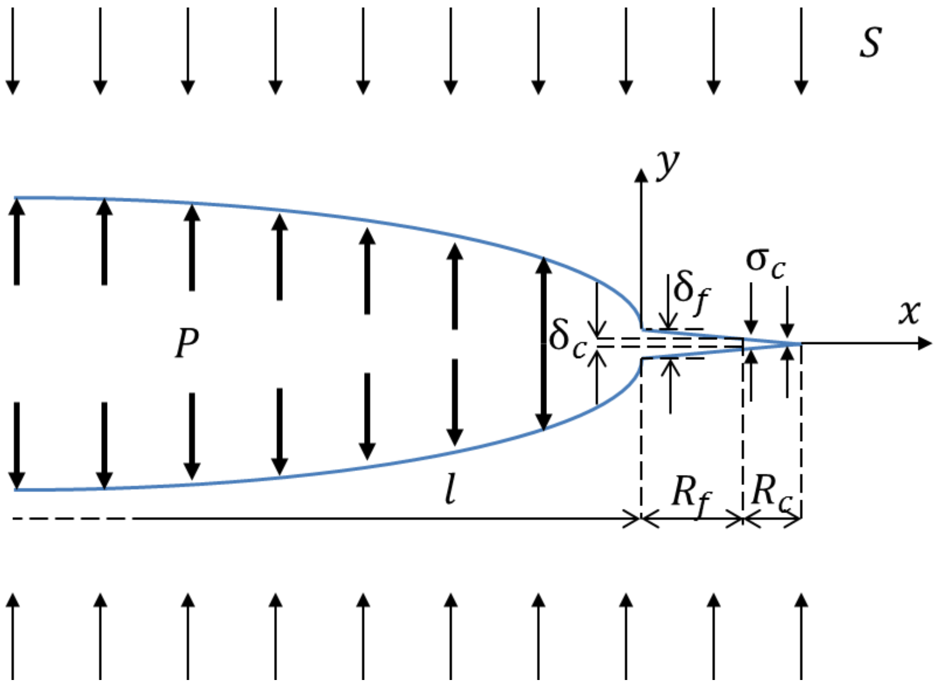

Figure 2.4. Configuration of DB model with fluid lag under confining pressure. (R_c and R_f are the length of cohesive zone and fluid lag, respectively. δ_c and δ_f are the opening at the end of cohesive zone and fluid lag, respectively. l is fracture half-length)

As indicated by Rubin (1993), in order to eliminate the singularity at the tip of cohesive zone ($x = R_f + R_c$), the stress intensity factor should be zero at that point.

Following the procedure in deriving equation (2.9), the condition of absence of singularity at the cohesive zone tip with fluid lag can be written as

$$(P-S)\sqrt{l+R_f+R_c}-\frac{\sqrt{8}}{\pi}P\sqrt{R_f+R_c}-\frac{\sqrt{8}}{\pi}\sigma_T\sqrt{R_c}=0 \qquad (2.16)$$

If the fluid front ($x = 0$) is considered as the crack tip, the apparent fracture toughness is defined as (neglecting terms of order R_f/l and R_c/l)

$$K_c=(P-S)\sqrt{\pi l}=\sqrt{\frac{8}{\pi}}(P\sqrt{R_f+R_c}+\sigma_T\sqrt{R_c}) \qquad (2.17)$$

Considering $R_f \ll l$ and $R_c \ll l$, based on equation (2.17), the fluid net pressure $(P-S)$ is negligible compared with the internal fluid pressure P, and thus P can be approximated as the confining stress S. Thus, the apparent fracture toughness can be also expressed as

$$K_c=\sqrt{\frac{8}{\pi}}(S\sqrt{R_f+R_c}+\sigma_T\sqrt{R_c}) \qquad (2.18)$$

To initiate fracture propagation, the opening at the end of cohesive zone should be equal to the critical opening δ_c, which is given as (Rice, 1968; Rubin, 1993; Khanzan and Fialko, 1995)

$$\delta_c=\frac{4(1-v^2)\sqrt{R_c}}{E}[\sqrt{2}(P-S)\sqrt{l}-\frac{1}{\pi}P\left(2\sqrt{R_c+R_f}+\frac{R_f}{\sqrt{R_c}}ln\frac{(\sqrt{R_c+R_f}+\sqrt{R_c})}{(\sqrt{R_c+R_f}-\sqrt{R_c})}\right)-\frac{2}{\pi}\sigma_T\sqrt{R_c}] \quad (2.19)$$

Substitute equation (2.17) to equation (2.19), δ_c can be expressed as (P can be approximated as the confining stress S)

$$\delta_c=\frac{8(1-v^2)\sigma_T R_c}{\pi E}[\frac{S}{\sigma_T}\left(\sqrt{1+R_f/R_c}-\frac{R_f}{2R_c}ln\frac{(\sqrt{R_c+R_f}+\sqrt{R_c})}{(\sqrt{R_c+R_f}-\sqrt{R_c})}\right)+1] \qquad (2.20)$$

Based on equation (2.20), cohesive zone length R_c can be normalized by the cohesive length under zero confining, which is given by equation (2.4). The dimensionless cohesive length can be represented as function of dimensionless confining pressure $\frac{S}{\sigma_T}$, and dimensionless fluid lag length $\frac{R_f}{R_c}$, which yields

$$\frac{R_c}{R_c^0} = \frac{1}{[\frac{S}{\sigma_T}\left(\sqrt{1+R_f/R_c} - \frac{R_f}{2R_c} ln\frac{\left(\sqrt{1+R_f/R_c}+1\right)}{\left(\sqrt{1+R_f/R_c}-1\right)}\right)+1]} \tag{2.21}$$

where R_c^0 is the cohesive zone length at zero confining and the value is given by equation (2.4). According to equation (2.21), the cohesive zone length R_c increases from $\frac{R_c^0}{1+S/\sigma_T}$ to R_c^0 as the length of fluid lag R_f increases from zero to infinite. The relationship between dimensionless cohesive zone size and dimensionless fluid lag size at different confining stress is illustrated in Figure 2.5. As illustrated in the figure, the length of cohesive zone decreases with the in-situ stress magnitude.

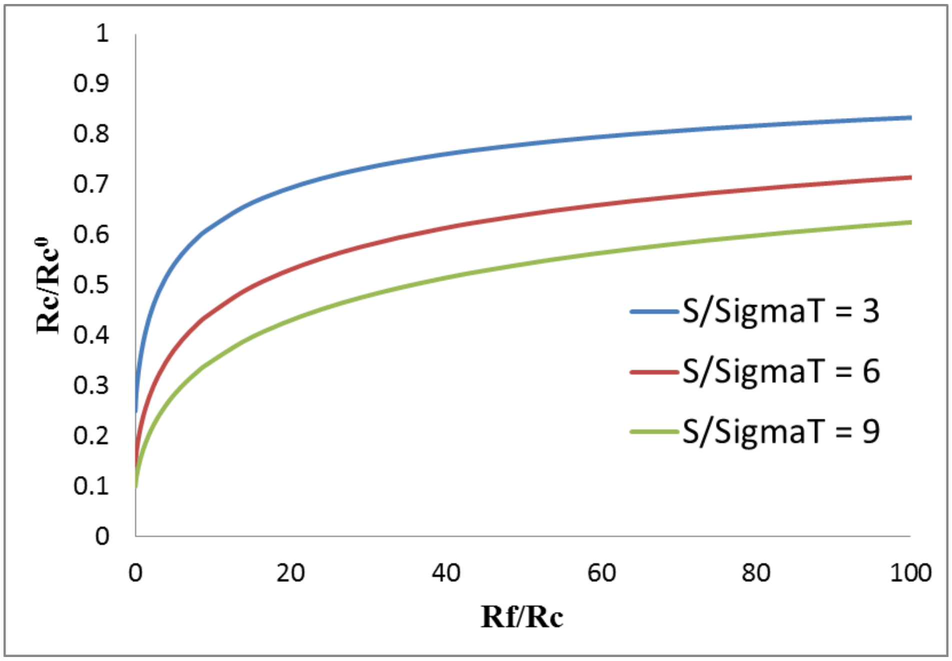

Figure 2.5. Relationship between dimensionless cohesive zone length and dimensionless fluid lag length under various confining stresses. S is the confining stress and SigmaT is the cohesive stress.

The value of apparent fracture toughness can be also normalized by the fracture toughness at zero confining. Thus, equation (2.18) can be reorganized as

$$\frac{K_c}{K_c^0} = \left(\frac{S}{\sigma_T}\sqrt{R_f/R_c + 1} + 1\right)\sqrt{R_c/R_c^0} \tag{2.22}$$

where K_c^0 is the apparent fracture toughness at zero confining, which is given by equation (2.6). Based on equation (2.21) and (2.22), the relationship between the dimensionless fracture toughness and dimensionless fluid lag size at different confining pressures is illustrated in Figure 2.6. The result shows that the value of apparent fracture toughness increases with confining stress magnitude and fluid lag length. Remote compressive stress acting on the process zone resists fracture from opening. As confining stress increases, greater net pressure is required to initiate fracture. As indicated by Figure 2.6, the apparent fracture toughness will increase with the length of fluid lag. If fluid lag exists (R_f > 0), higher net pressure is required to make fracture propagate. As a result, the apparent fracture toughness determined from the DB model with fluid lag could probably explain the large fracture toughness calibrated from field data.

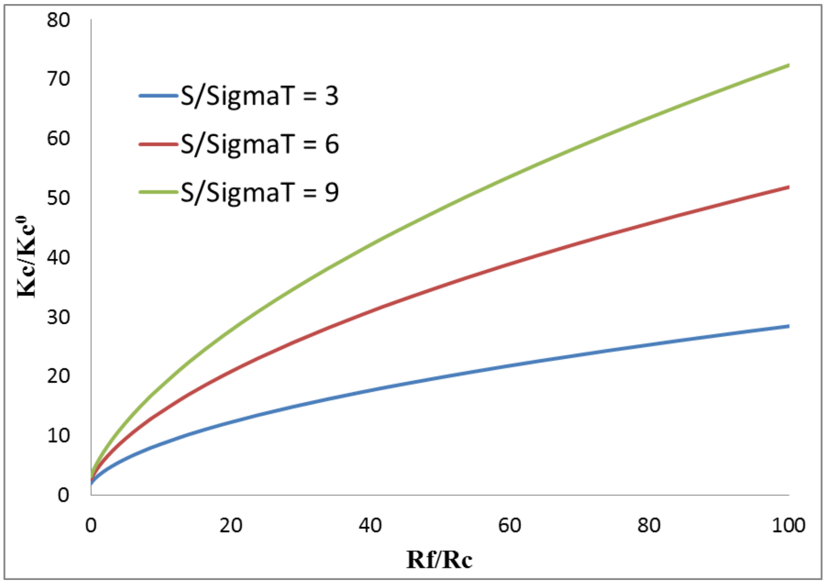

Figure 2.6. Relationship between dimensionless apparent fracture toughness and dimensionless fluid lag size under different confining stress. SigmaT is the tensile strength and *S* is the confining stress. Fracture toughness increases with confining stress and fluid lag size.

The first term in equation (2.18) is the contribution of fluid lag on the apparent fracture toughness, whereas the second term is the contribution of cohesive stress. The contribution of the fluid lag on the apparent fracture toughness is related to both confining stress and fluid lag length. The contribution of the fluid lag on the apparent fracture toughness can be represented as

$$\frac{K_f}{K_c} = \frac{\sqrt{\frac{8}{\pi}} S \sqrt{R_f + R_c}}{\sqrt{\frac{8}{\pi}} (S\sqrt{R_f + R_c} + \sigma_T \sqrt{R_c})} = \frac{\frac{S}{\sigma_T} \sqrt{R_f/R_c + 1}}{\left(\frac{S}{\sigma_T} \sqrt{R_f/R_c + 1} + 1\right)} \tag{2.23}$$

where K_f is the contribution of fluid lag on the apparent fracture toughness and K_c is the apparent fracture toughness. According to equation (2.23) and Figure 2.7a, the weight of contribution of fluid lag on the apparent fracture toughness increases from $\frac{S/\sigma_T}{1+S/\sigma_T}$ to 1 as

R_f increases from zero to infinite. The result indicates that the contribution of fluid lag on the apparent fracture toughness increases with fluid lag length and confining stress. The contribution of fluid lag is zero if the in-situ confining stress is zero or fluid lag length is zero. Based on Figure 2.6 and Figure 2.7a, the weight of contribution of fluid lag on the apparent fracture toughness can be also characterized in terms of dimensionless apparent fracture toughness, which is illustrated in Figure 3.7b. The result shows that as the apparent fracture toughness increases, the contribution of fluid lag becomes more important. As a result, the fluid lag effect becomes dominant at large fracture toughness and cannot be ignored in hydraulic fracture analysis. Large value of apparent fracture toughness calibrated from the field data (Delaney and Pollard, 1981; Shlyapobersky, 1985; Olson, 2003; Schultz et al. 2008) is mainly attributed to the fluid lag effect.

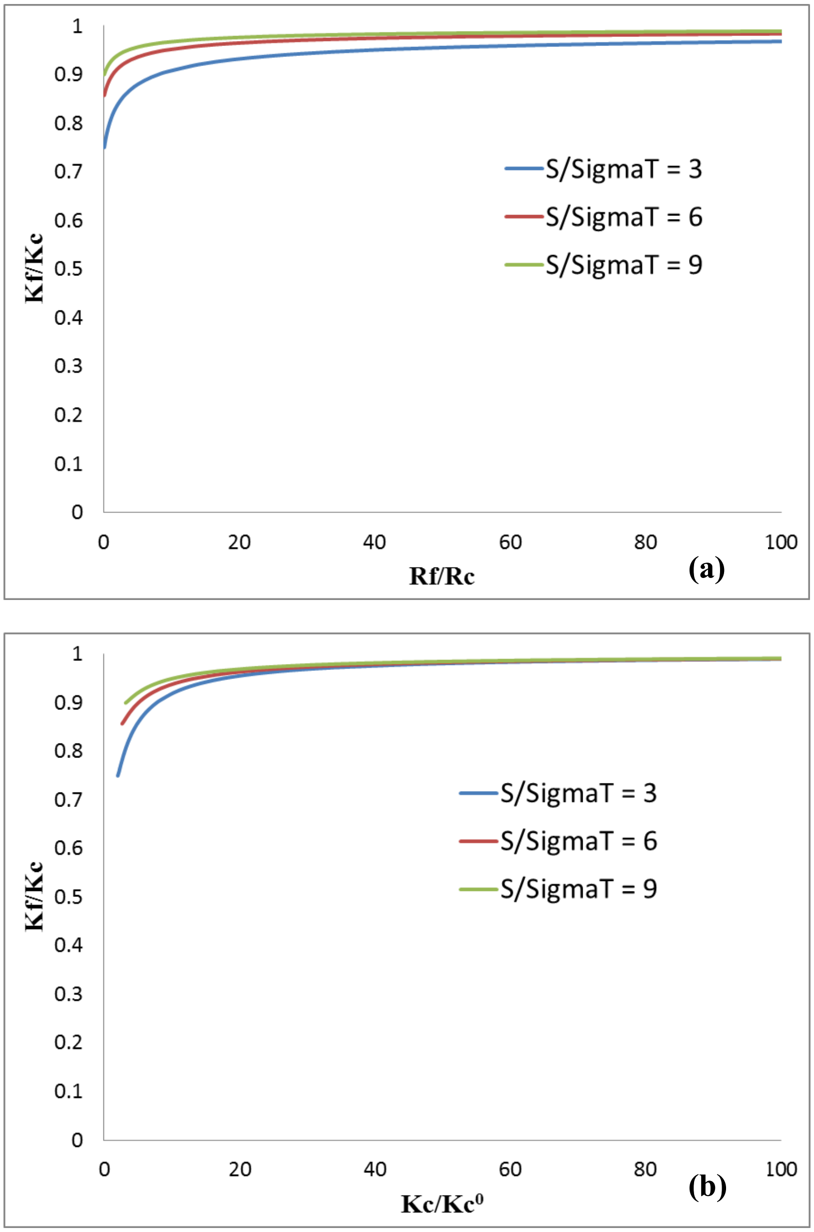

Figure 2.7. The contribution of fluid lag on the apparent fracture toughness in terms of (a) dimensionless fluid lag length and (b) dimensionless apparent fracture toughness under different confining pressures. The results indicate that fluid lag effect becomes dominant at large apparent fracture toughness.

2.4 Comparison of Near-tip Stress

Simulating hydraulic fracture initiation and propagation with CZM is complicated and computationally expensive (Garagash and Detournay 2000; Garagash and Detournay 2003). On the contrary, in the approach of LEFM, the tip effects related to fluid lag and nonlinear rock deformation can be lumped into the apparent fracture toughness. Thus, the goal is to demonstrate that LEFM with accurate apparent fracture toughness is an appropriate approach to investigate the propagation of fluid-driven fractures under confining pressure. Previous studies (TSCRG Groups, 1993; Yakov and Khazan, 1995) compared fracture width profiles between LEFM solutions and DB model predictions. They showed that both solutions agree well for a significant portion of the fracture width profile. In this study, the near-tip stress state and fracture energy of LEFM with the apparent fracture toughness are compared with the DB model to demonstrate the validity of this approach for fracture propagation.

In the DB model, we could define and compute a value for apparent fracture toughness based on fluid lag size and confining stress. In LEFM, fracture toughness is utilized as the criterion of fracture propagation and the value of fracture toughness significantly affects fracture net pressure, fracture geometry, and the stress state ahead of fracture tip. In this section, solutions between LEFM and DB models with/without fluid lag are compared by investigating the near-tip stress state of a quasi-statically propagating fracture. Three cases are investigated: a 100-meter long crack under uniform remote tensile stress with the cohesive length of R_c (Figure 2.1a), a 100-meter long crack without fluid lag subjected to compressive stress and internal pressure (Figure 2.1b), and a 100-meter long crack with fluid lag subjected to compressive stress and internal pressure (Figure 2.4).

In the cohesive zone model, the cohesive stress is equal to 5 MPa and the critical opening is 0.02 mm, which accounts for fracture energy to be 1 J/m^2. Furthermore, the plane strain Young's modulus ($\frac{E}{1-v^2}$) of rocks is assumed 10 GPa. According to equation (2.6), for fractures under tensile loading (Figure 2.1a), the fracture toughness and cohesive zone size are calculated to be 1 MPa$\sqrt{\mathrm{m}}$ and 1.57 cm, respectively. Based on equation (2.5), the remote tensile stress is calculated to be 0.08 MPa. The stress state is computed using the finite element software ABAQUS (Dassault Systèmes, 2013). Figure 2.8a shows the near-tip stress state from LEFM solutions when fracture toughness is 1 MPa$\sqrt{\mathrm{m}}$, whereas Figure 2.8b shows the near-tip stress state based on DB model without confining stress. As illustrated in Figure 2.8a, the stress is infinite at the fracture tip and decreases with distance relative to fracture tip. The results in Figure 2.8b show that the stress state is finite everywhere and the stress value is approximately 5 MPa in the vicinity of cohesive zone. Note that the contour of stress magnitude, 3 MPa and below, of Figure 2.8a is identical to Figure 2.8b outside the cohesive zone. If the base of cohesive zone is considered as fracture tip, the near-tip stress state outside the cohesive zone could be represented by K-dominated solutions.

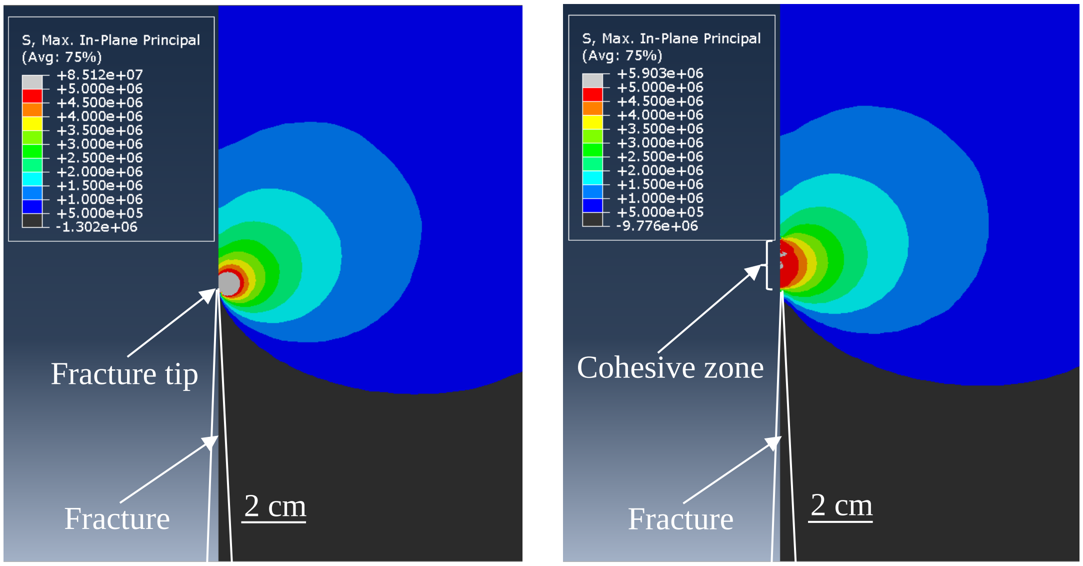

(a) (b)

Figure 2.8. Comparison of the near-tip stress states induced by fracture: (a) the maximum principal stress of LEFM with fracture toughness of 1MPa$\sqrt{m}$; (b) the maximum principal stress based on DB model without confining. For fractures under tensile loading, the near-tip stress state between LEFM and DB models is comparable outside the cohesive zone. In LEFM model, a remote tensile stress of 0.08 MPa is applied normal to the fracture surface. In the cohesive zone model, a remote tensile stress of 0.08 MPa is applied normal to the fracture surface and a cohesive stress of 5 MPa is applied in the cohesive zone to close the fracture.

For fractures under confining (Figure 2.1b), the parameters of DB model in Figure 2.9b are the same with those in Figure 2.8b but there is a confining stress of 40 MPa acting perpendicular to the fracture surface. According to equations (2.13) and (2.14), the cohesive zone size and fluid net pressure are calculated to be 0.174 cm and 0.24 MPa, respectively. Based on LEFM, fracture toughness can be defined in terms of net pressure and fracture half-length, and the value is calculated to be 3 MPa$\sqrt{m}$. Compared to fractures under tension, the cohesive zone size decreases and the apparent fracture toughness increases when the fracture is under confining. Figure 2.9a shows the near-tip stress state from LEFM solutions when the fracture toughness is 3 MPa$\sqrt{m}$, whereas Figure 2.9b shows the near-tip stress state based on DB model with a confining stress of 40 MPa. The results indicate that the near-tip stress state outside the cohesive zone in Figure 2.9b is equivalent to the stress state in Figure 2.9a. However, LEFM solutions (Figure 2.8a) using the fracture toughness (1 MPa$\sqrt{m}$) measured from standard tests would underestimate the near-tip stress state when fractures are under confining pressure. Thus, the solution of LEFM with the apparent fracture toughness is a good approximate for the near-tip stress state under high confining stress.

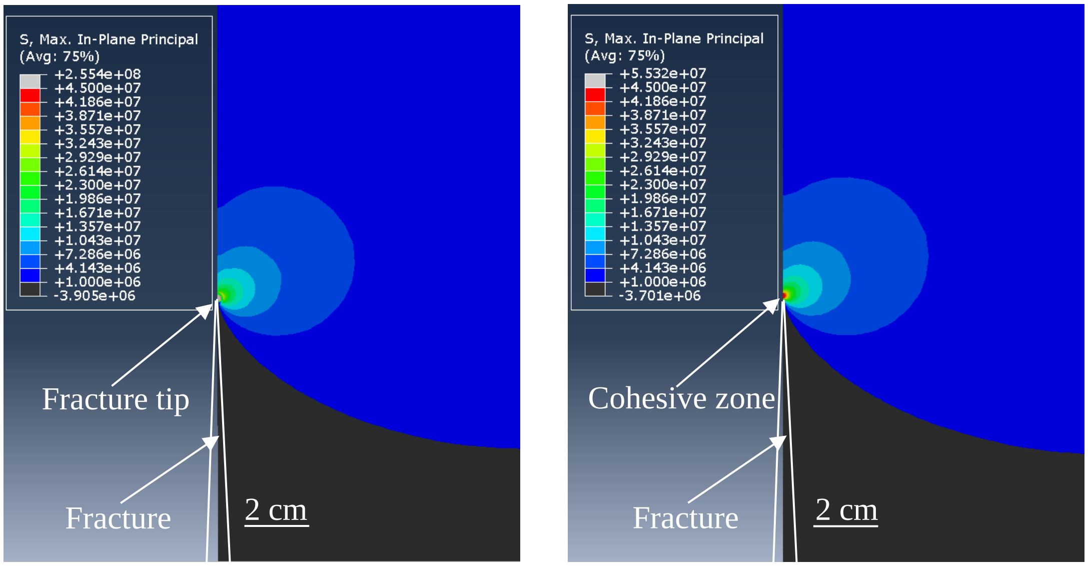

(a) (b)

Figure 2.9. Comparison of the near-tip stress states induced by pressurized fracture: (a) the near-tip stress state of LEFM with fracture toughness of 3MPa$\sqrt{m}$; (b) the near-tip stress state based on DB model without fluid lag under compressive loading. In LEFM model, a net pressure of 0.24 MPa is applied normal to the fracture surface. In the cohesive zone model, a net pressure of 0.24 MPa is applied normal to the fracture surface and a cohesive stress of 45 MPa is applied in the cohesive zone to close the fracture.

For fractures under confining with fluid lag (Figure 2.4), the parameters of DB model in Figure 2.10b are identical to those in Figure 2.8b and Figure 2.9b. Figure 2.10b shows the near-tip stress state for DB model with fluid lag under the confining stress of 40 MPa. Based on equation (2.21), the length of cohesive zone is calculated to be 0.45 cm when the fluid lag length is assumed 4 times the cohesive zone length. According to equation (2.17), net pressure is calculated to be 0.8 MPa when fracture starts to propagate. Based on LEFM, fracture toughness can be defined in terms of net pressure and fracture half-length, and the value is calculated to be 10 MPa$\sqrt{m}$. The results show that both net pressure and apparent fracture toughness increase if fluid lag exists ahead of fluid front. Compared to Figure 2.9b, the results in Figure 2.10b show that the near-tip stress induced by the pressurized fracture increases if there is unwetted zone behind the fracture tip. If the fluid front is considered as fracture tip, the near-tip stress state outside the process zone in Figure 2.10b is equivalent to the stress state in Figure 2.10a, which is based on LEFM with the apparent fracture toughness of 10 MPa$\sqrt{m}$. Thus, the near-tip stress state of LEFM using apparent fracture toughness is a good estimate to the stress state of fluid-driven fracture with fluid lag under confining stress.

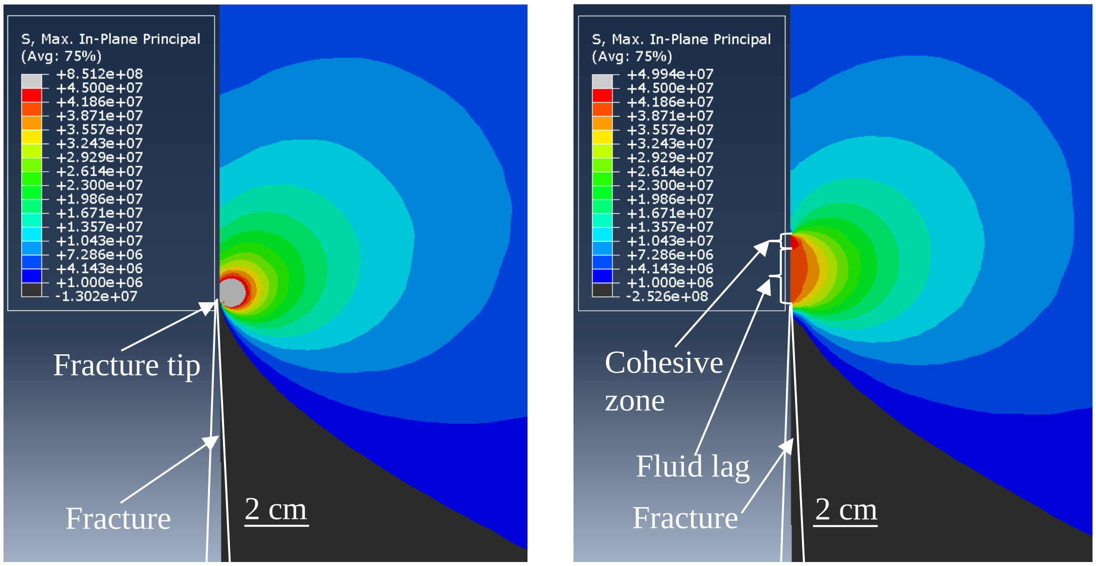

(a) (b)

Figure 2.10. Comparison of the near-tip stress states induced by pressurized fracture: (a) the near-tip stress state of LEFM with fracture toughness of 10MPa$\sqrt{\text{m}}$; (b) the near-tip stress state based on DB model with fluid lag under compressive loading. In LEFM model, a net pressure of 0.8 MPa is applied normal to the fracture surface. In the cohesive zone model, a net pressure of 0.8 MPa is applied normal to the fracture surface and a cohesive stress of 45 MPa is applied in the cohesive zone to close the fracture, with a confining stress of 40 MPa acting on the fluid lag to close the fracture.

2.5 Comparison of Fracture Energy

In this section, another approach is applied to investigate the validity of LEFM with the apparent fracture toughness by comparing fracture energy between LEFM and DB models. In LEFM, fracture is going to propagate when the stress intensity factor reaches fracture toughness. The stress intensity factor criterion is equivalent to the energy balance criterion through Irwin's formula. In LEFM, the apparent fracture toughness of fluid-driven fractures can be obtained from equation (2.18) and fracture energy can be expressed as

$$G = \frac{8(1-v^2)(S\sqrt{R_f+R_c}+\sigma_T\sqrt{R_c})^2}{\pi E} \tag{2.24}$$

Based on the DB model with fluid lag, fracture propagation is resisted by the confining pressure acting on the fluid lag zone and the cohesive stress acting on the cohesive zone. Thus, the total fracture energy can be expressed as

$$G = \sigma_T * \delta_c + S * \delta_f \tag{2.25}$$

where $\sigma_T * \delta_c$ is the fracture energy of cohesive zone based on the definition of traction-separation law in the DB model, whereas $S * \delta_f$ represents the fracture energy of fluid lag. Thus, in order to calculate the total fracture energy, the opening at the fluid front is required. By using equation (3.12) of Khazan and Fialko (1995), the opening at the fluid front is calculated to be

$$\delta_f = \frac{8(1-v^2)\sigma_T R_c}{\pi E}[\frac{S}{\sigma_T}(1+\frac{R_f}{R_c}) + \left(\sqrt{1+\frac{R_f}{R_c}} + \frac{R_f}{2R_c} ln \frac{(\sqrt{R_c+R_f}+\sqrt{R_c})}{(\sqrt{R_c+R_f}-\sqrt{R_c})}\right)] \tag{2.26}$$

Based on equations (2.20) and (2.26), the ratio between opening at the fluid front and opening at the end of cohesive zone can be expressed as (*P* is approximated as *S*)

$$\frac{\delta_f}{\delta_c} = \frac{\frac{S}{\sigma_T}(1+\frac{R_f}{R_c})+\left(\sqrt{1+\frac{R_f}{R_c}}+\frac{R_f}{2R_c}ln\frac{\left(\sqrt{R_c+R_f}+\sqrt{R_c}\right)}{\left(\sqrt{R_c+R_f}-\sqrt{R_c}\right)}\right)}{\frac{S}{\sigma_T}\left(\sqrt{1+R_f/R_c}-\frac{R_f}{2R_c}ln\frac{\left(\sqrt{R_c+R_f}+\sqrt{R_c}\right)}{\left(\sqrt{R_c+R_f}-\sqrt{R_c}\right)}\right)+1} \tag{2.27}$$

As indicated by equation (2.27), the normalized opening at the fluid front is related to the dimensionless confining stress and the dimensionless fluid lag length. As shown in Figure 2.11a, the critical opening at fluid front increases with the length of fluid lag. For a given fluid lag size, the opening at fluid front increases with confining stress. The relationship between normalized opening of fluid front and dimensionless apparent fracture toughness under different confining stress can also be obtained by combining equation (2.21), (2.22) and (2.27). As shown in Figure 2.11b, the opening at fluid front increases with the apparent fracture toughness. However, for a given fracture toughness, the normalized opening at the fluid front decreases with confining stress. As a result, for a given apparent fracture toughness of hydraulic fractures, it can be interpreted that the opening at the fluid front at a shallow reservoir will be larger than the value in a deep reservoir.

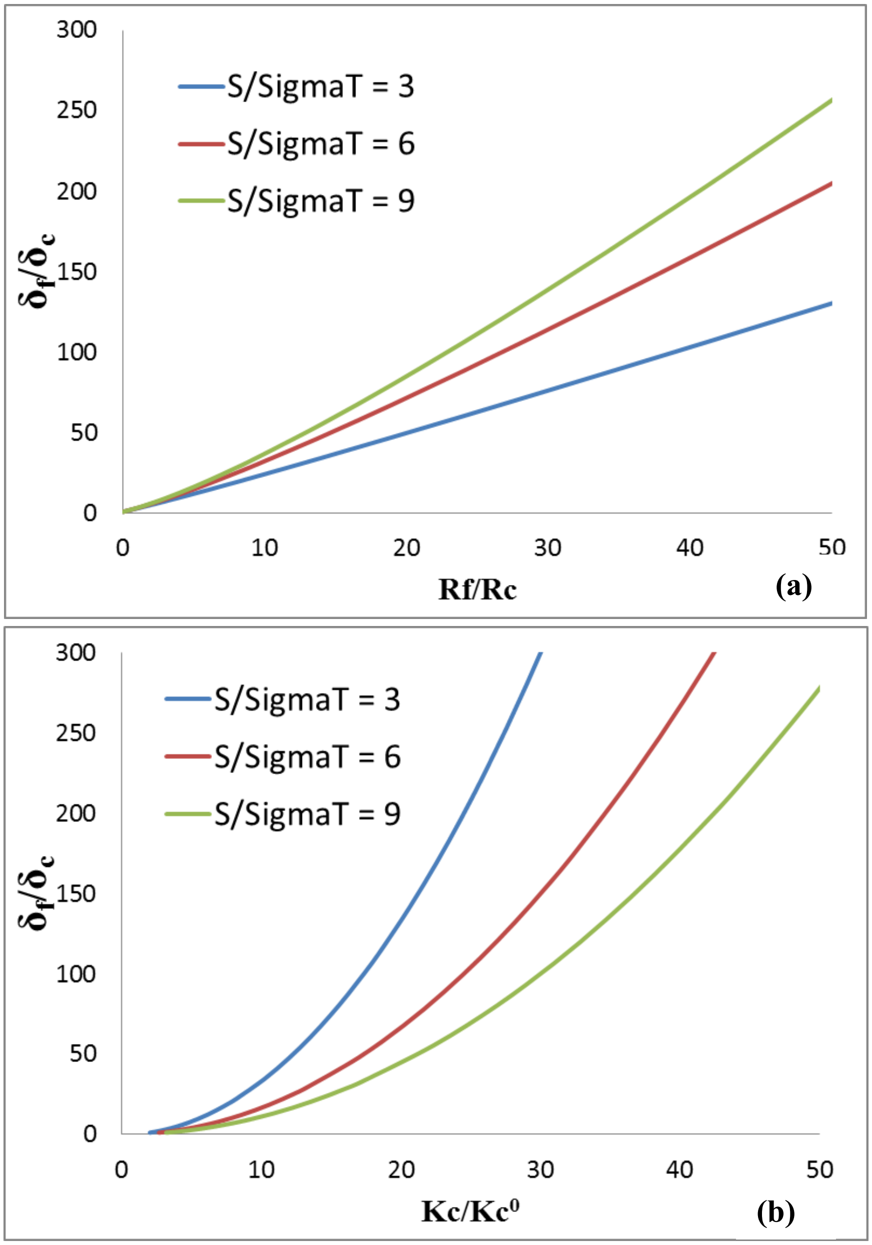

Figure 2.11. The relationship between normalized opening at the fluid front and (a) the normalized fluid lag length and (b) the dimensionless apparent fracture toughness under different confining stress.

After calculating the critical opening of fluid front, the second term in equation (2.25) can be expressed as

$$S * \delta_f = \frac{8(1-v^2)}{\pi E}[S^2(R_c + R_f) + \sigma_T * S\left(\sqrt{(R_c + R_f)R_c} + \frac{R_f}{2} ln\frac{(\sqrt{R_c+R_f}+\sqrt{R_c})}{(\sqrt{R_c+R_f}-\sqrt{R_c})}\right)] \quad (2.28)$$

By substituting equation (2.20) to equation (2.25), the first term in equation (2.25) can be expressed as

$$\sigma_T * \delta_c = \frac{8(1-v^2)}{\pi E}[S * \sigma_T\left(\sqrt{(R_c + R_f)R_c} - \frac{R_f}{2} ln\frac{(\sqrt{R_c+R_f}+\sqrt{R_c})}{(\sqrt{R_c+R_f}-\sqrt{R_c})}\right) + \sigma_T^2 * R_c] \quad (2.29)$$

Thus, the total fracture energy based on DB model is calculated as

$$G = \frac{8(1-v^2)(S\sqrt{R_f+R_c}+\sigma_T\sqrt{R_c})^2}{\pi E} \quad (2.30)$$

Noting that equations (2.24) and (2.30) are equivalent, fracture energy calculated by DB model is the same as the fracture energy based on LEFM if the apparent fracture toughness is utilized. As a result, LEFM with the apparent fracture toughness is an appropriate approach to investigate fluid-driven fractures under confining stress.

2.6 Discussion

The fracture toughness of hydraulic fractures could be calibrated from hydraulic fracturing treatments (Shlyapobersky, 1985), whereas the fracture toughness of joints and veins could be calibrated based on displacement-length scaling (Olson, 2003; Schultz et al. 2008). The estimated fracture toughness of hydraulic fractures is on the order of 10 MPa$\sqrt{m}$ (Shlyapobersky 1985; Shlyapobersky 1989). According to Olson (2003), the fracture toughness of meter-long veins (Culpeper Quarry and Florence Lake veins) observed in field is also on the order of 10 MPa$\sqrt{m}$. Based on equation (2.18), fluid lag size can be quantified based on the cohesive stress, in-situ stress, cohesive zone size, and the apparent fracture toughness of fluid-driven fractures. Assuming that the cohesive stress is 5 MPa and apparent fracture toughness is constant, the relationship between fluid lag size and in-situ stress is illustrated in Figure 2.12. Fisher and Warpinski (2012) showed that the depth of various unconventional plays varies between 4000 and 14000 ft. Thus, the range of minimum in-situ stress in Figure 2.12 is chosen to be in the range between 20 and 70 MPa. The results show that the fluid lag length of hydraulic fractures is on the order of centimeters. When the apparent fracture toughness is considered 10 $\text{MPa}\sqrt{\text{m}}$, the fluid lag length of hydraulic fractures decreases from 7.6 to 0.5 cm as depth increases from 4000 to 14000 ft.

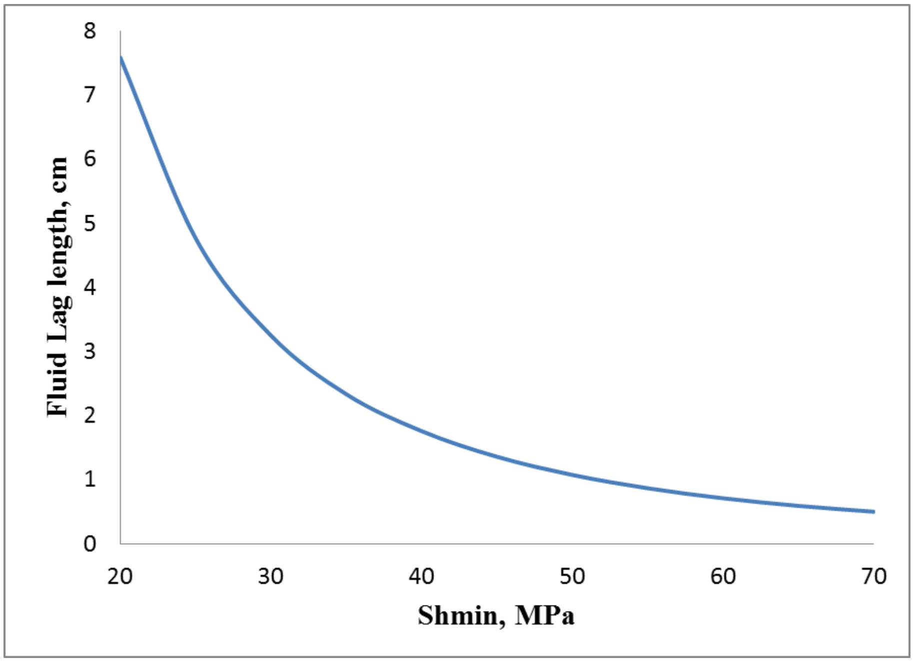

Figure 2.12. Relationship between fluid lag length and confining pressure at the apparent fracture toughness of 10 $\text{MPa}\sqrt{\text{m}}$ (veins and hydraulic fractures).

As shown in Table 2.2, based on the calibrated fracture toughness, the estimated fluid lag length of hydraulic fractures and veins is on the order of centimeters if the fractures are in the depth of a few kilometers. The results also indicate that the ratio between fluid lag length and fracture length for hydraulic fractures and veins are approximately on the order of 0.01, which validates the small scale yield condition in the previous analysis.

Table 2.2. Fluid lag length of various fluid-driven fractures (hydraulic fractures and veins)

	Shmin, MPa	Fracture type	Fracture toughness, $\mathrm{MPa}\sqrt{m}$	Fluid lag, cm
Shlyapobersky (1985)	41.4	hydraulic fracture	9.7, 15.6, 21.5	2, 4.5, 8
Culpeper Quarry Olson (2003)	32-64	vein	8-16	~2.5
Florence Lake Olson (2003)	38-76	vein	12-25	~4

A number of numerical studies also determined the fluid lag length by finite element based algorithm analysis (Hunsweck et al. 2013) and boundary element method (Garagash and Detournay, 2000; Detournay 2016). In their approach, fracture and fluid propagation is characterized by two distinctive boundaries changing with time: crack tip and fluid front. The crack tip position is quantified by Griffin's theory of fracture propagation. The location of the fluid front is characterized by satisfying the condition that fluid pressure is equal to zero and the moving front velocity is equal to the flux at the fluid front, which yields

$$\frac{dl}{dt} = \frac{q}{w} \tag{2.31}$$

where l is the fracture half-length, q is the flow rate at the fluid front, and w is the fracture width at the fluid front.

Under the assumption of constant fracture propagation velocity, Garagash and Detournay (2000) concluded that the size of fluid lag is dependent on fluid viscosity, in-situ stress, fluid propagation velocity, modulus, and fracture toughness of the host rock. In particular, the estimate of the maximum fluid lag is given as (Garagash and Detournay, 2000).

$$\lambda \cong \frac{4\mu_f E'^2 V}{S^3} \tag{2.32}$$

where S is the in-situ stress perpendicular to fracture surface, μ_f is the fluid viscosity, V is the fracture propagation velocity, E' is the plane strain Young's modulus, and λ is the length of fluid lag. Based on equation (2.32), the maximum fluid lag length can be estimated if the fracture propagation velocity is known. As indicated by equation (2.32), the length of fluid lag is zero when the fluid viscosity is zero and increases with fluid viscosity. Thus, the apparent fracture toughness increases with fluid viscosity. Equation (2.32) might qualitatively provide insight into the effect of viscosity on fluid lag size as well as the apparent fracture toughness. The difference of apparent fracture toughness between hydraulic fractures (approximately 10 $\mathrm{MPa}\sqrt{\mathrm{m}}$) and dikes (approximately 100 $\mathrm{MPa}\sqrt{\mathrm{m}}$) might be due to the viscosity difference between fracturing fluids (1~1000 cp) and highly viscous magma (~100000 cp) (Delaney and Pollard, 1981).

2.7 Conclusions

In this study, we utilized the Dugdale-Barenblat cohesive zone model to investigate the contributions of fluid lag and confining stress on the apparent fracture toughness of fluid-driven fractures. Based on the DB model, the analytical results show that the discrepancy of fracture toughness between laboratory measurement and field calibration is mainly due to fluid lag and confining stress. The magnitude of apparent fracture toughness increases with the length of fluid lag and the magnitude of the in-situ confining stress.

By comparing the near-tip stress state between LEFM and DB model, this study demonstrated that K-dominated stress state is a good measurement of the near-tip stress state outside the fluid lag and cohesive zone of fluid-driven fractures if the apparent fracture toughness is utilized. However, LEFM with the fracture toughness measured from standard laboratory tests underestimates the near-tip stress state. This study also proved that fracture energy of fluid-driven fractures calculated by DB model is the same as the fracture energy based on LEFM by utilizing the apparent fracture toughness. Thus, under the small scale yielding condition, LEFM with apparent fracture toughness is an appropriate approach to investigate the near-tip stress state of fluid-driven fractures under confining stress.

This study also calculated the fluid lag size of hydraulic fractures and veins. The results showed that the fluid lag length is on the order of centimeters, which validates the small scale yield condition of LEFM in hydraulic fracturing analysis.

CHAPTER 3: LAYERED MODULUS EFFECT ON FRACTURE MODELING AND HEIGHT CONTAINMENT

3.1 Introduction

As discussed in the literature review of fracture height containment (section 1.3.4), compared to the in-situ stress contrast and interface strength, the effect of modulus contrast between adjacent layers is generally not considered to exert an important impact on fracture height containment. Simonson et al. (1978) investigated the effect of modulus contrast on fracture height containment with an analysis of the stress intensity factor at the crack tip. His study showed that if the opposite material is stiffer, the stress intensity factor approaches to zero as the tip gets closer to the interface, and thus the stiffer material acts as a perfect barrier to prevent fractures from penetration. Van Eekelen (1982)'s results also revealed that fracture width at the stiff layer is narrower, which reduces fluid flow to fracture tip in the stiff layers, and finally, reduces the rate of fracture height growth. However, their conclusions are contradictory to the field observations (Figure 1.3), where soft layers generally arrest fluid-driven fractures.

Very few studies established the contribution of soft layers on fracture height containment, and instead the effect of modulus contrast between adjacent layers on fracture height growth is generally neglected (Van Eekelen, 1982; Smith et al. 2001). In order to illustrate the effect of soft layers on fracture height containment, this study proposed an alternative approach, which is based on the effective modulus of a layered reservoir.

In this study, finite element analysis was utilized to develop an approximation to evaluate the effective modulus of a layered reservoir, which could contribute to the improvement of the material balance in hydraulic fracture simulation. Then, the effect of modulus contrast on fracture height growth is investigated with an analysis of the stress intensity factor, considering the change of effective modulus as the fracture tip propagates from the stiff layer to the soft layer. The fracture height containment mechanism illustrated in this work could provide insight into the field observations of arrested fluid-driven fractures at soft layers (Jeffrey et al. 1992; Philipp et al. 2013; Ferrill et al. 2014).

3.2 Literature Review of Effective Modulus

In hydraulic fracturing, the elastic modulus of host rocks significantly affects the net pressure and fracture width profiles. In general, stiffer host rocks yield higher treating pressure and smaller fracture width, and vice versa. Sneddon (1946) provided one of the most common 2-D plane strain solutions for calculating fracture width in a homogeneous medium, which are given as

$$w(x) = \frac{4(1-v^2)P_{net}}{E}\sqrt{(H/2)^2 - x^2} \tag{3.1}$$

$$\bar{w} = \frac{\pi(1-v^2)P_{net}H}{2E} \tag{3.2}$$

where w is the width along the crack, $\overline{w}$ is the average fracture width, E is the Young's modulus, v is Poisson's ratio, H is fracture height, and P_{net} is the net pressure (the difference between fluid pressure and the closure pressure).

However, unconventional reservoirs are highly heterogeneous and usually stratified with layers of different mechanical properties. For instance, Eagle Ford shale is a well-laminated reservoir with alternating stiff carbonate-rich layers and soft clay-rich layers (Ferrill et al. 2014). It is challenging to evaluate fluid pressure and width profiles when the formation is stratified. Thus, a number of numerical approaches were applied to take into account the variation of mechanical properties in hydraulic fracturing design. StimPlan (NSI Technologies Inc. 2010), a fully 3D finite element simulator, has been widely utilized to provide a correct solution of fracture geometry in a layered formation. Siebrits and Peirce (2002) also presented a multi-layer elastic model, based on the modified displacement discontinuity method, to evaluate fracture width profiles in a layered medium.

Layered modulus leads to significant complication in fracture modeling. Most hydraulic fracturing simulators assume a single and uniform value of modulus to reduce the computational cost. A common approach for simulating fracture width in a layered medium is to utilize an effective modulus by averaging elastic properties across the layers that are hydraulically fractured. Table 3.1 shows a summary of approximation methods to evaluate the effective modulus in various hydraulic fracturing simulators. GOHFER (Barree, 1983) utilized Boussinesq (1885) displacement solution to calculate the average elastic modulus. However, Smith et al. (2001) pointed out that this method is inappropriate because Boussinesq displacement solution is only valid in a homogeneous medium. The approach in Terra-Frac (Clifton and Wang, 1988) extended the displacement solution for bi-material space (Lee and Keer, 1986) to solutions for multiple layers. However, this approach could also lead to large errors in the prediction of fracture width (Smith et al. 2001). CFRAC (McClure and Horne, 2013) and XFRAC (Wu and Olson, 2015) do not take into account the modulus variation between layers. The effective modulus of a layered medium in FracproPT (FracproPT, 2007) is based on the height-weighted mean, which is given as

$$\bar{E} = \frac{\sum h_i E_i}{\sum h_i} \tag{3.3}$$

where h_i is the thickness of layer *i* and E_i is the Young's modulus of layer *i*. However, determining the effective modulus is tricky and the common height-weighted approximation can lead to significant errors in calculating fracture width, as well as the overall material balance and fluid efficiency (Smith et al., 2001). Several important factors must be considered in calculating the effective modulus (Smith et al., 2001): (1) height percentage of each rock in a layered sequence; (2) the location of each rock layer; (3) the value of modulus of each rock.

Table 3.1. Approximations of effective modulus in various hydraulic fracturing simulators

GOHFER (Barree, 1983)	Based on Boussinesq displacement solution for infinite half homogeneous space under point load
Terra-Frac (Clifton and Wang, 1988)	Based on displacement solution for infinite half space consisting two bonded homogenous materials
FracproPT (FracproPT, 2007)	Height-weighted averaging method
XFRAC (Wu and Olson, 2015) /CFRAC (McClure and Horne, 2013)	Do not consider mechanical heterogeneity

3.3 Methodology

In this study, the approximation of effective modulus was developed by comparing to the FEM effective modulus, which is determined by matching the average width using a trial-and-error approach based on the numerical results of fracture width profiles. The finite element software ABAQUS (Dassault Systèmes, 2013) is utilized for numerical simulation.

The first goal of this study is to determine the FEM effective modulus of a layered medium. Figure 3.1 illustrates a 28-layer model with a 120-feet tall fracture in the middle. The total dimension of the model is 800 feet by 400 feet, with fixed displacement boundary conditions at the top and bottom. As illustrated in Table 3.2, a net pressure of 300 psi is applied on the fracture surface, and the default Young's modulus and Poisson's ratio are 1 Mpsi and 0.3, respectively. The given fracture height and applied fluid net pressure yield an apparent fracture toughness of 15 $\text{MPa}\sqrt{\text{m}}$, which is in good agreement with the fracture toughness calibrated from hydraulic fracturing treatments

(Shlyapobersky, 1985). Figure 3.2 shows the comparison of fracture width profiles between the numerical results and the analytical solution, which is calculated using equation (3.1). The results indicate that our numerical model gives very good agreement with the analytical solution. The FEM effective modulus of a layered medium can be investigated by changing the modulus value of each rock layer, height percentage of each rock, the number of layers, and layer location.

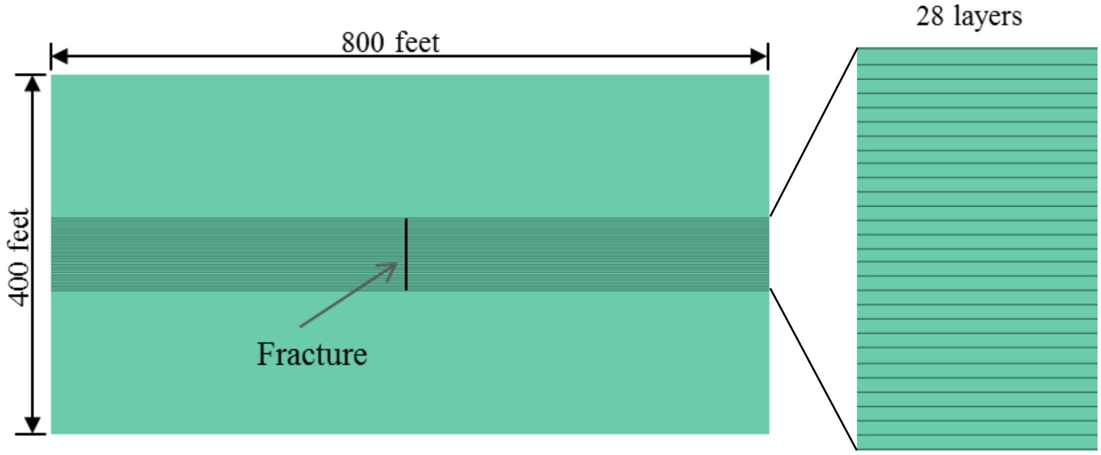

Figure 3.1. Configuration of a 28-layer fracture model. The top and bottom of the model is fixed. Net pressure is applied on the fracture surface to open the fracture.

Table 3.2. Parameters of the fracture model

Parameters	
Net pressure, psi	300
Young’s modulus, psi	1e6
Poisson's ratio	0.2
Fracture height, ft	120

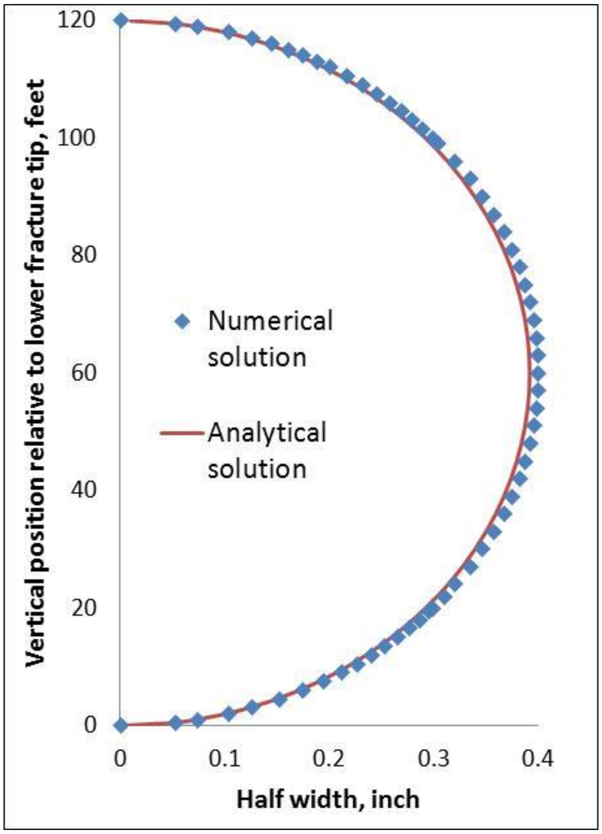

Figure 3.2. Comparison of fracture width profiles between numerical and analytical solutions (equation 3.1). The parameters of the fracture model are given in Table 3.2.

The second goal is to develop an alternative method to evaluate the effective modulus that is a good estimate of the FEM effective modulus. In this study, our approach is to run various numerical simulations for field cases, and then to compare the effective modulus approximations with the FEM effective modulus. Our approximation methods are based on two analytical assumptions, namely height-weighted mean (equation 3.3) and height-weighted harmonic average (Jones, 1975; Yue et al. 2016), which is given as

$$\bar{E}_{harmonic} = \frac{\sum h_i}{\sum \frac{h_i}{E_i}} \tag{3.4}$$

Figure 3.3a and b show the conceptual models for the height-weighted mean and the height-weighted harmonic average, respectively, for a layered elastic system. In the case of height-weighted mean, bedding planes are bonded and layers are deformed uniformly under a uniform compressive load. However, in the conceptual model of the height-weighted harmonic average, bedding planes are freely slipping and layers are deformed independently.

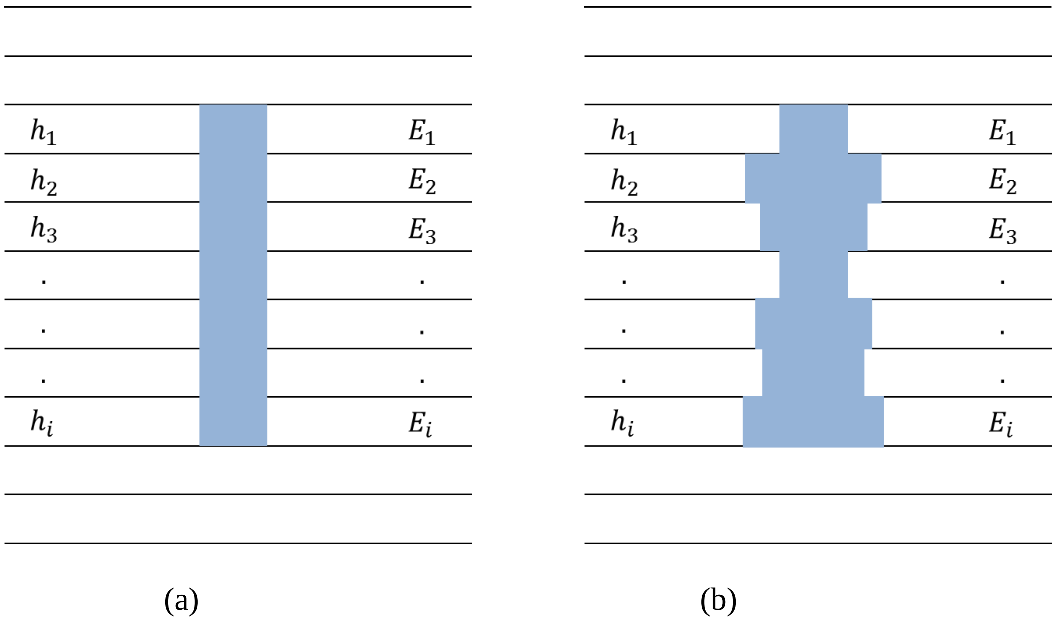

Figure 3.3. Conceptual models for (a) the height-weighted mean and (b) the height-weighted harmonic average. In the conceptual model of the height-weighted mean, bedding planes are bonded and layers are deformed uniformly, whereas layers deforms with freely slipping bedding planes in the conceptual model of the height-weighted harmonic average.

Height-weighted mean is known as the Voigt (1910) average and height-weighted harmonic average is known as the Reuss (1929) average. Voigt and Reuss averages are widely interpreted as the upper and lower bounds, respectively, for the ratio of average stress to average strain within the composite. However, the definition of effective modulus in this study is not the ratio of average stress to average strain within a composite, and instead it can be expressed in terms of the ratio of fluid net pressure to average fracture width, which is given by equation (3.2). The representation of the effective modulus of the layers which are hydraulically fractured, using Voigt and Reuss averages, have not been studied.

3.4 Results

3.4.1 Effective Modulus of a Layered Reservoir

A number of numerical simulations were performed with various tip locations, modulus values, layer location, the number of layers, and height percentage of each rock layer to evaluate FEM effective modulus.

3.4.1.1 Effect of Tip Locations

Based on the log and core data, Mullen (2010) discovered that the values of Young's Modulus vary between 1 and 2 Mpsi for a well drilled in the gas-condensate window of Eagle Ford play. For another well in the dry-gas window, Young's Modulus in the mud facies is around 2 Mpsi; whereas the limestone layers have a higher modulus of 3-3.5 Mpsi. Thus, the ratio of Young's Modulus between stiff and soft layers in Eagle Ford is on the order of two. In addition, Vaca Muerta is also a laminated formation with bedding-parallel veins called 'beef' (Rodrigues et al. 2009; Wang and Gale, 2016). According to Ortiz et al. (2016), the static Young's Modulus of Vaca Muerta formation varies between 0.8 and 6 Mpsi due to the mineralogical variations. Thus, modulus ratios between one and five were utilized in this study to investigate the effect of modulus values.

In this study, the numerical models contain alternating stiff and soft layers, which is a good approximate of Eagle Ford formation. A three-layer model (Figure 3.4a) was utilized to evaluate the FEM effective modulus of a layered reservoir. The height ratio of top, middle, and bottom layers is 9: 10: 9, and the moduli of the outer and middle layers are defined as E_1 and E_2, respectively. In this study, the modulus of each layer varies between 1 and 5 Mpsi, whereas Poisson's ratio and net pressure are kept constant. By changing the modulus contrast between the middle and outer layers, the effect of modulus values on the effective modulus could be evaluated.

Figure 3.4b shows the comparison between the approximations of effective moduli (height-weighted and harmonic moduli) and FEM effective modulus, which is determined from finite element modeling for the three-layer case illustrated in Figure 3.4a. The results show that the height-weighted mean yields a good match with the FEM effective modulus if the ratio of E_2 to E_1 is less than one (in that case, the fracture tips lie in the stiff layer). For example, when the ratio of E_2 to E_1 is 0.5, the normalized FEM effective modulus is $0.84E_1$, which is close to the height-weighted mean of $0.82E_1$;

whereas the use of height-weighted harmonic average would suggest a modulus of 0.74E_1, an error of 12% in calculating the average fracture width.

When the ratio of E_2 to E_1 is larger than one (as illustrated in Figure 3.4a, the fracture tips lie in soft layers), the height-weighted harmonic average matches with the FEM effective modulus, whereas the common height-weighted mean can cause significant errors. For instance, when the ratio of E_2 to E_1 is two, the normalized FEM effective modulus is 1.14E_1, which is close to the height-weighted harmonic average of 1.21E_1; whereas the use of height-weighted effective modulus would suggest a modulus of 1.35E_1, an error of 18% in calculating the average fracture width. The results indicate that the height-weighted approximation is a good estimation of the FEM effective modulus if the fracture tip lies in the stiff layer; whereas the height-weighted harmonic average is a good estimation of FEM effective modulus if the fracture tip lies in the soft layer.

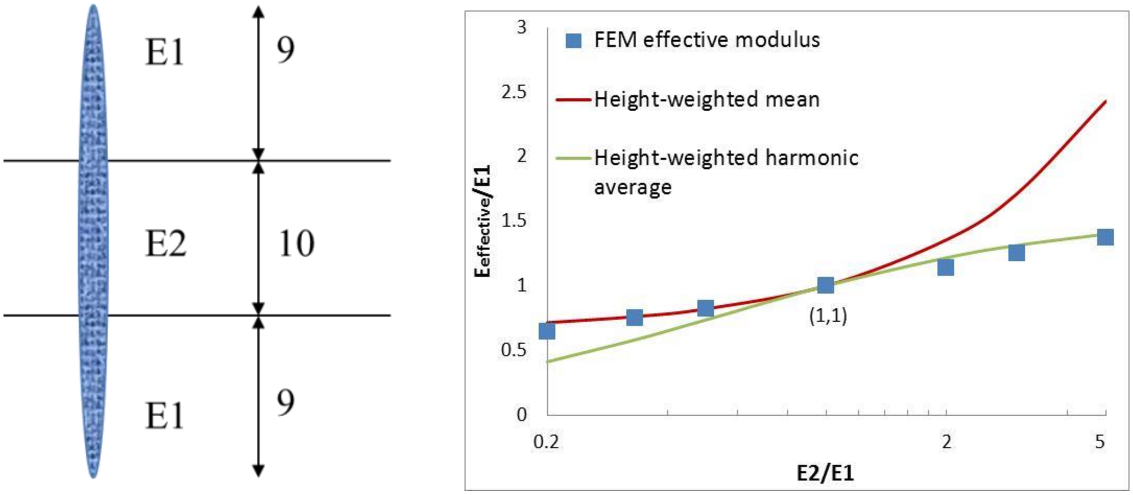

(b) (b)

Figure 3.4. (a) Illustration of a three-layer model. The height ratio of top, middle, and bottom layers is 9: 10: 9; (b) Comparison between FEM effective modulus and effective modulus approximations (height-weighted and harmonic) with respect to various modulus ratios for the three-layer case. The results indicate that the height-weighted approximation is a good estimation of the FEM effective modulus if the fracture tip lies in the stiff layer; whereas the height-weighted harmonic average is a good estimation of FEM effective modulus if the fracture tip lies in the soft layer.

Figure 3.5 illustrates the comparison of fracture width profiles with respect to fracture tip locations. The solid curves show the fracture width profiles when the fracture tip lies in stiff layers, whereas the dashed curves illustrate the fracture width profiles when the fracture tip lies in soft layers. The results indicate that fracture width profiles are different when fracture tips lie in different layers. Compared to cases where fracture tips are in stiff layers, fracture tips are blunter at soft layers, which enhances fracture opening everywhere. This could probably explain the reason why the effective modulus approximations are different when the fracture tips lie in different layers.

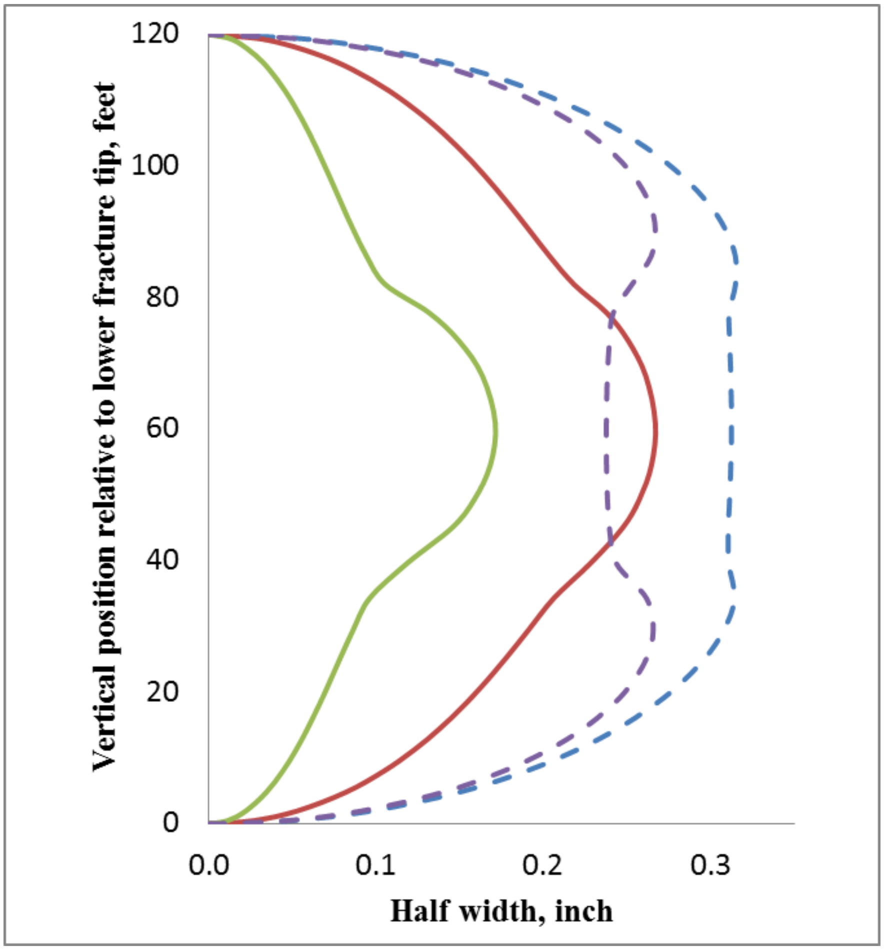

Figure 3.5. Illustration of fracture width profiles with respect to tip location. Solid curves show the cases of fracture tip in the stiff layer, whereas dashed curves show the cases of fracture tip in the soft layer. In the case of solid green curve, the outer and inner moduli are 5 and 1 Mpsi, respectively. In the case of solid red curve, the outer and inner moduli are 2 and 1 Mpsi, respectively. In the case of dashed purple curve, the outer and inner moduli are 1 and 5 Mpsi, respectively. In the case of dashed blue curve, the outer and inner moduli are 1 and 2 Mpsi, respectively.

3.4.1.2 Effect of Modulus Contrast and Height Percentage of Rock Layer

A number of simulations were performed to investigate the effect of height percentage of each rock layer on the effective modulus of a layered medium. As illustrated in Figure 3.6, layered models with the following height percentages of soft rocks were utilized: 0.07, 0.29, 0.43, 0.64, and 0.93. In these models, the moduli of the soft and stiff layers are 1 and 2 Mpsi, respectively, which are a good approximate for Eagle Ford formation. The FEM effective modulus is determined from numerical analysis and height-weighted harmonic average is calculated based on equation (3.4) for comparison.

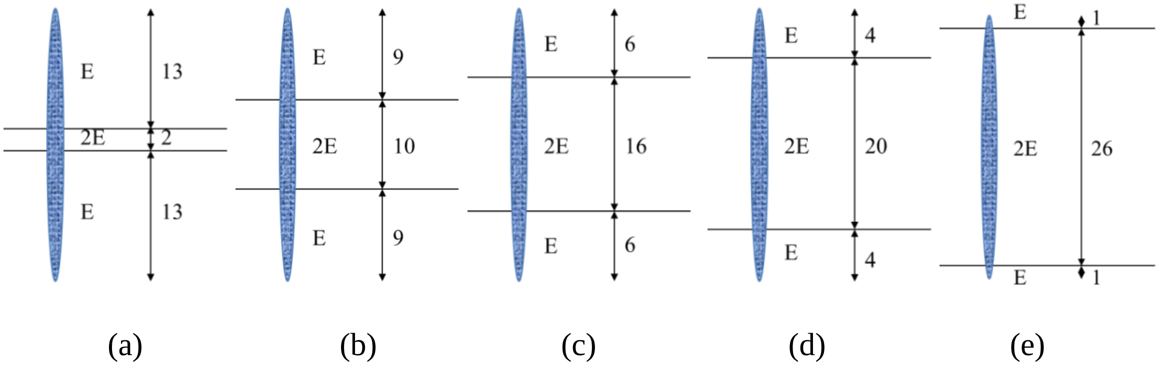

(a) (b) (c) (d) (e)

Figure 3.6. Illustration of layered reservoir-analog models when fracture tips are in the soft layer (a) the height percentage of soft rock is 0.93; (b) the height percentage of soft rock is 0.64; (c) the height percentage of soft rock is 0.43; (d) the height percentage of soft rock is 0.29; (e) the height percentage of soft rock is 0.07. (*E* = 1 Mpsi)

The blue dots and red curve in Figure 3.7a show the FEM effective modulus and height-weighted harmonic average, respectively. The results indicate that the value of FEM effective modulus is smaller than height-weighted harmonic average and the error increases as the height percentage of soft rock layer decreases. For instance, the height-weighted harmonic average only yields a difference of 2% relative to the harmonic value when the height percentage of soft rock layer is 0.93, whereas the difference increases to 25% when the height percentage of soft rock layer is 0.07. The results indicate that an additional geometry factor should be included in order to reduce the error in the height-weighted harmonic average. Thus, the effective modulus is given as

$$\bar{E} = \frac{1}{(\frac{a}{E_l}+\frac{1-a}{E_h})} * (1 + f(a)) \tag{3.5}$$

where a is the height percentage of soft rock layer, E_l is the modulus of soft rocks, and E_h is the modulus of stiff rocks, $\frac{1}{(\frac{a}{E_l}+\frac{1-a}{E_h})}$ is equivalent to the height-weighted harmonic average, and $f(a)$ is the geometry factor and could be represented as a function of height percentage a. Mathematically, $f(a)$ could be represented in series of a as

$$f(a) = x_0 + x_1 a + x_2 a^2 + x_3 a^3 + \cdots \tag{3.6}$$

where x_0, x_1, x_2, x_3, … are coefficients and need to be determined. According to Figure 3.7a, the height-weighted harmonic average yields a difference of 16% relative to the harmonic value when the height percentage of soft rock layer is 0.29, whereas the difference increases to 25% when the height percentage of soft rock layer is 0.07. However, when the layered medium is 100% soft rocks, the geometry factor should be zero. Thus, the boundary conditions are given by

$$\begin{aligned} f(1) &= 0 \\ f(0.29) &= -0.16 \end{aligned} \tag{3.7}$$

$$f(0.07) = -0.25$$

As a result, $f(a)$ could not be constant or a linear function. Based on the boundary conditions, the solution of $f(a)$ is not unique but the simplest formula of $f(a)$ could be calculated as

$$f(a) = -0.28 + 0.48a - 0.2a^2 \tag{3.8}$$

Figure 3.7a illustrates the comparison between FEM effective modulus and modified height-weighted harmonic average. The results indicate that a good match is obtained at the modulus ratio of two after the geometry factor $f(a)$ is included. Thus, the effective modulus at the modulus ratio of two could be represented as

$$\bar{E} = \frac{1}{(\frac{a}{E_l}+\frac{1-a}{E_h})} * (1 + (-0.28 + 0.48a - 0.2a^2)) \tag{3.9}$$

However, when $E_h = E_l = E$, the effective modulus is equal to E and the value of the effective modulus is independent of the percentage of soft rock layer, suggesting that equation 3.9 needs to be adjusted to take into account the effect of modulus contrast at modulus ratios other than two. Thus, a modulus factor $y\left(\frac{E_h}{E_l}\right)$ is included and the effective modulus in equation 3.9 is modified as

$$\bar{E} = \frac{1}{(\frac{a}{E_l}+\frac{1-a}{E_h})} * \left(1 + y\left(\frac{E_h}{E_l}\right) * (-0.28 + 0.48a - 0.2a^2)\right) \tag{3.10}$$

The boundary conditions of modulus factor $y(\frac{E_h}{E_l})$ could be represented as

$$y(1) = 0$$

$$y(2) = 1 \tag{3.11}$$

Based on the boundary conditions, the simplest form of $y(\frac{E_h}{E_l})$ can be represented as

$$y\left(\frac{E_h}{E_l}\right) = \left(\frac{E_h}{E_l} - 1\right)^c \tag{3.12}$$

where *c* is the power coefficient. In order to evaluate *c*, another set of simulations were performed for a modulus ratio equal to three. According to Figure 3.7b, the height-weighted harmonic average yields a difference of 22% when the height percentage of soft rock layer is 0.29 whereas the difference increases to 36% when the height percentage of soft rock layer is 0.07. Thus, the boundary conditions are

$$y(3)f(0.29) = (2)^c * (-0.16) = -0.22 \tag{3.13}$$

$$y(3)f(0.07) = (2)^c * (-0.25) = -0.36$$

Solving each of these cases in equation 3.13 yields *c* as 0.46 and 0.51, respectively. Then, we averaged *c* to be 0.48. Thus, a modified height-weighted harmonic average is developed as

$$\bar{E} = \frac{1}{\left(\frac{a}{E_l} + \frac{1-a}{E_h}\right)} * \left(1 + \left(\frac{E_h}{E_l} - 1\right)^{0.48} (-0.28 + 0.48a - 0.2a^2)\right) \tag{3.14}$$

The comparison of effective modulus in Figure 3.7b also demonstrates that the modified height-weighted harmonic average yields a good match with the FEM effective modulus for various height percentages when the modulus ratio is three.

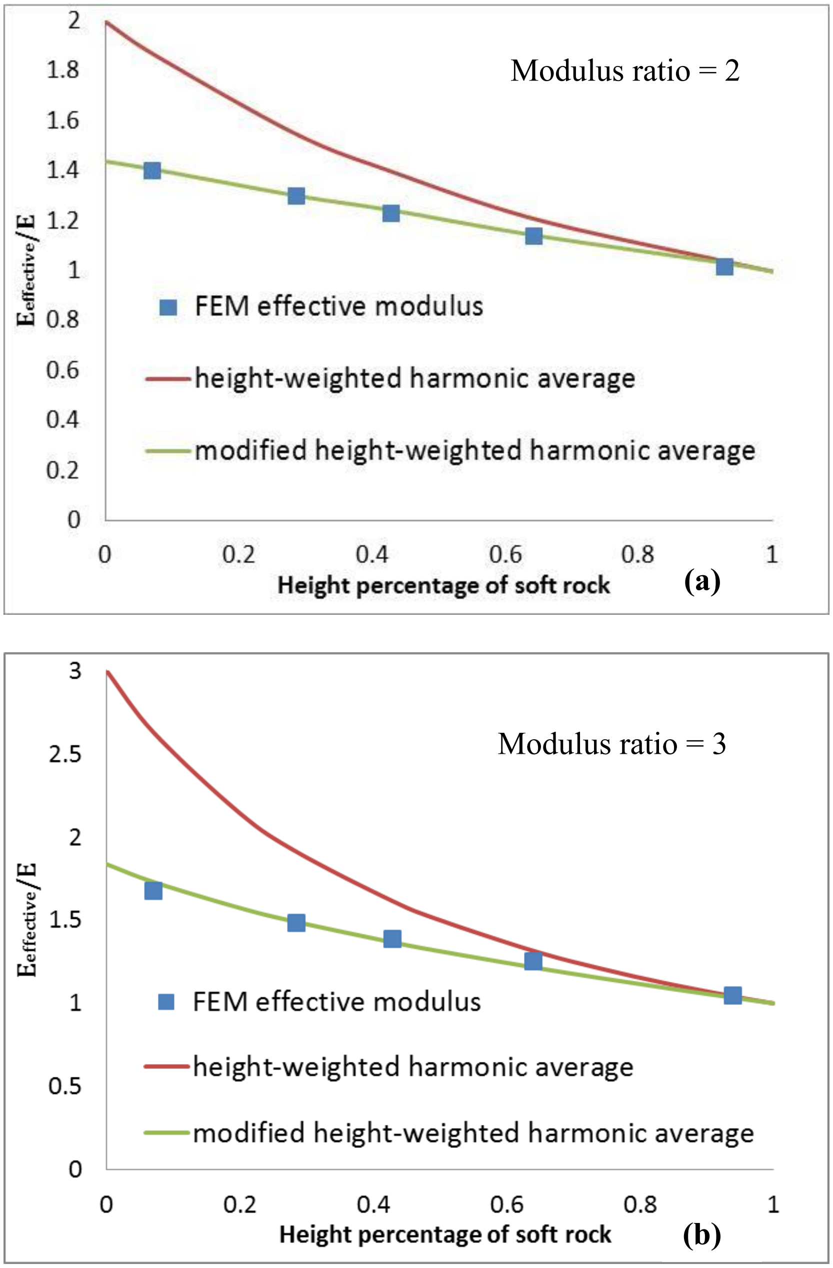

Figure 3.7. Comparison between FEM effective modulus, height-weighted harmonic average, and modified height-weighted harmonic average with respect to height percentage of soft rock when (a) the modulus ratio is two; (b) the modulus ratio is three.

Figure 3.8 shows layered models with various height percentages of stiff rocks to illustrate the effect of height percentage on the effective modulus when the fracture tips lie in stiff layers. In these models, the modulus ratio is two and the Poisson's ratio is 0.3. As illustrated in Figure 3.8, the following height percentages of stiff rock layer were utilized: 0.07, 0.29, 0.43, 0.64, and 0.93. The blue dots in Figure 3.9a show the FEM effective modulus and the red curve illustrates the height-weighted mean. The results indicate that there is error when fracture tips lie in the stiff layer but it is not as significant as when the tips were in the soft layer. The error of height-weighted mean increases as the height percentage of stiff rock layer decreases. For example, the height-weighted mean only yields a difference of 1% relative to the height-weighted mean when the height percentage of stiff rocks is 0.93. However, the difference increases to 15% when the height percentage of stiff rock is 0.07.

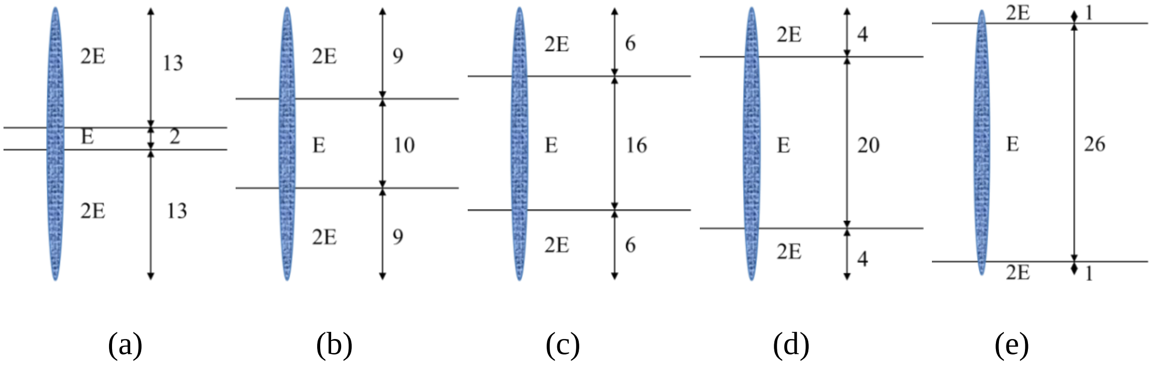

Figure 3.8. Illustration of layered reservoir-analog models when fracture tips are in the stiff layer (a) the height percentage of stiff rock is 0.93; (b) the height percentage of stiff rock is 0.64; (c) the height percentage of stiff rock is 0.43; (d) the height percentage of stiff rock is 0.29; (e) the height percentage of stiff rock is 0.07.

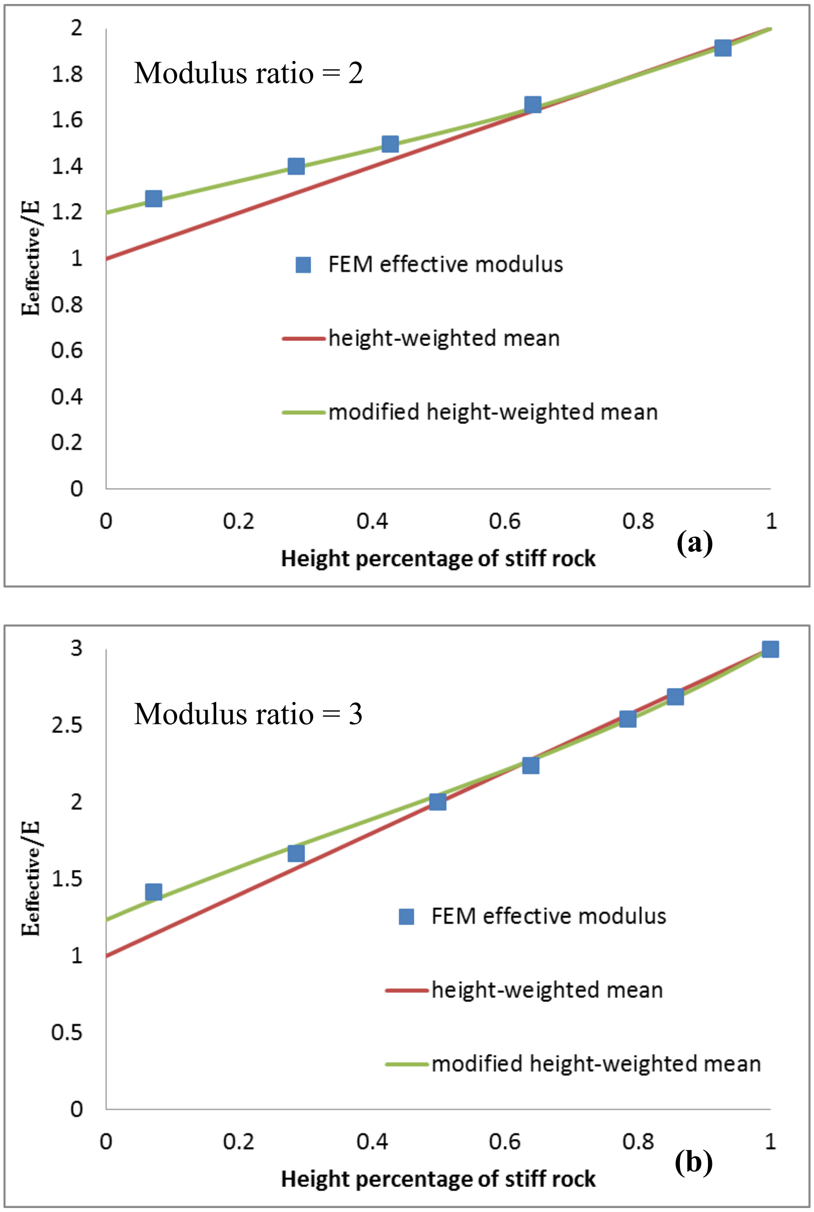

Figure 3.9. Comparison between FEM effective modulus, heighted-weighted modulus, and modified height-weighted mean with respect to height percentage of stiff rock when (a) the modulus ratio is two; (b) the modulus ratio is three.

Thus, in order to reduce the error in height-weighted mean when the height percentage of stiff rocks is low, a modified height-weighted mean was developed as

$$\bar{E} = [bE_h + (1-b)E_l] * (1 + \left(\frac{E_h}{E_l} - 1\right)^{0.1} (0.22 - 0.57b + 0.35b^2)) \qquad (3.15)$$

where b is the height percentage of stiff rock layer. The term $bE_h + (1-b)E_l$ in equation (3.15) is equivalent to the height-weighted mean. Following the form of the correction factors for the height-weighted harmonic average, a modulus factor $\left(\frac{E_h}{E_l} - 1\right)^{0.1}$ and a geometry factor $(0.22 - 0.57b + 0.35b^2)$ were empirically derived. The comparison of effective moduli in Figure 3.9b also demonstrates that the modified height-weighted mean yields a good match with the FEM effective modulus for various height percentages when the modulus ratio is three.

As discussed in the above section, the modified height-weighted mean and height-weighted harmonic average were developed with respect to height percentages of each rock layer when the modulus ratios are two and three. I ran cases with modulus ratios between one and ten to test the accuracy of the effective modulus approximations. Figure 3.10 illustrates the comparison between FEM effective modulus (blue dots), modified height-weighted mean (solid red curve), modified height-weighted harmonic average (solid green curve), height-weighted mean (dashed black curve), and height-weighted harmonic average (dashed purple curve) with respect to various modulus ratios when the height percentages of middle layer is 0.93, 0.64, 0.43, and 0.07. The results demonstrate that the modified height-weighted mean is a good match with the FEM effective modulus for various height percentages and modulus ratios less than five when the fracture tip lies in the stiff layer. When the fracture tip lies in the soft layer, the modified height-weighted harmonic average yields a good match with the FEM effective modulus for various height percentages and modulus ratios less than five. As illustrated in Figure 3.10b, the effective modulus approximation derived in this study does not match FEM effective modulus when the modulus ratio is ten. In order to obtain better accuracy for modulus ratio larger than five, the modulus factor in equation (3.12) needs to be modified to take into account more than one term.

The comparison between basic and modified effective moduli indicates that the unmodified height-weighted mean yields reasonable accuracy when fracture tips lie in the stiff layer. The error induced by unmodified effective moduli when fracture tips lie in the stiff layer is not as significant as when the tips were in the soft layer. The results also show that the actual FEM effective modulus is not within the unmodified height-weighted mean (Voigt average) and height-weighted harmonic modulus (Reuss average), whereas the ratio of average stress to average strain within the composite is bounded by Voigt and Reuss averages. In fact, the modified height-weighted mean is larger than the unmodified height-weighted mean and the modified height-weighted harmonic average is smaller than the unmodified height-weighted harmonic average. The difference might be mainly due to the effect of fracture, as the FEM effective modulus is defined as the ratio between fracture net pressure and fracture average width (equation 3.2). However, as shown in Figure 3.3, the conceptual models of height-weighted mean and the height-weighted harmonic average of layered systems consider displacement affected by two extreme cases of interface properties, neglecting the displacement affected by fracture opening.

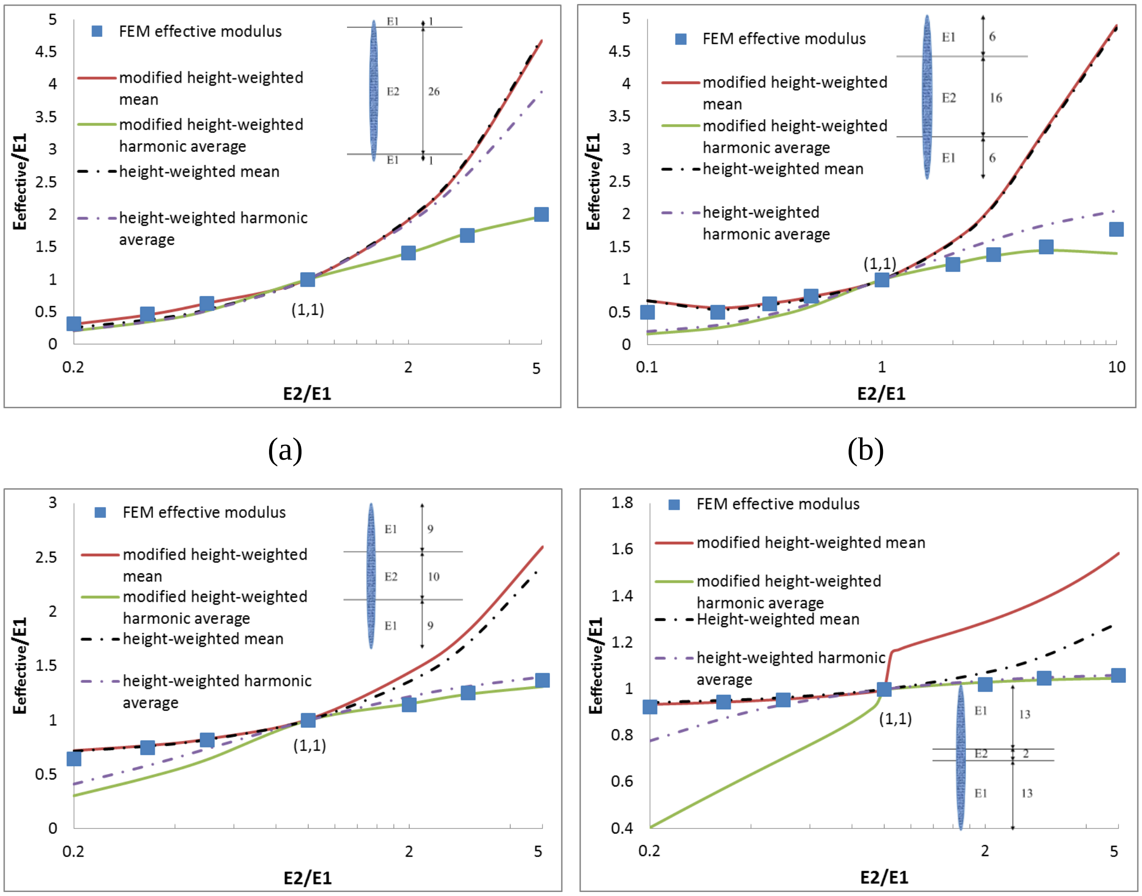

(a) (b)

(c) (d)

Figure 3.10. Comparison between FEM effective modulus (blue dots), modified height-weighted mean (solid red curve), modified height-weighted harmonic average (solid green curve), height-weighted mean (dashed black curve), and height-weighted harmonic average (dashed purple curve) with respect to various modulus ratios when the height percentages of middle layer is (a) 0.93, (b) 0.64, (c) 0.43, and (d) 0.07.

3.4.1.3 Effect of Layer Location

In the previous section, we developed effective modulus equations using symmetric three-layer geometries. In this section, we ran cases with five layers and unsymmetrical layer arrangements, with various layer locations, to test the accuracy of the effective modulus approximations. In Figure 3.11, the moduli of soft and stiff layers are 1 and 2 Mpsi, respectively. Moreover, the height percentage of soft rock is fixed as 0.64. The distance between the stiff layer and fracture tip reduces as can be seen from Figure 3.11a – d. As indicated by Table 3.3, there is less than 1% variation between the three layer and various five layer cases, suggesting the details of the layering is not important.

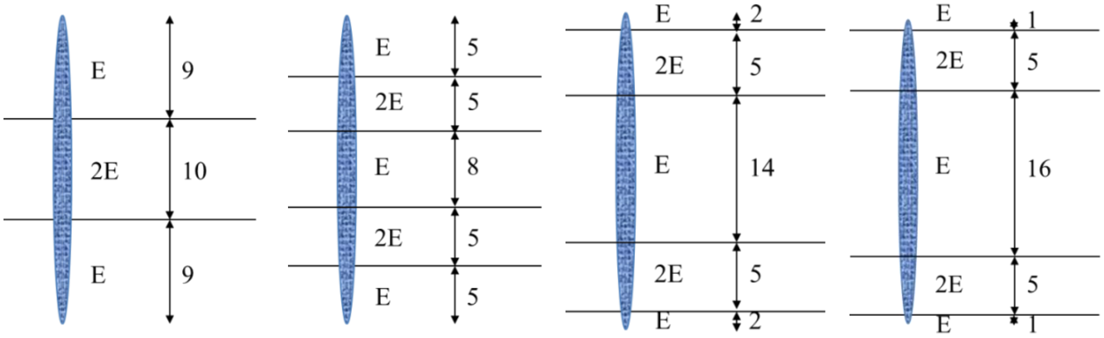

(a) (b) (c) (d)

Figure 3.11. Illustration of layered reservoir-analog models with various layer locations when fracture tips are in the soft layer. The distance between stiff layers and fracture tip reduces from a to d. (E = 1 Mpsi)

Table 3.3. FEM effective modulus values of models in Figure 3.11 (The modified height-weighted harmonic average is 1.14 Mpsi)

Case number	(a)	(b)	(c)	(d)
FEM effective modulus, Mpsi	1.14	1.14	1.13	1.13

Figure 3.12 shows unsymmetrical models with various layer locations, whereas the models in Figure 3.11 are symmetric. From Figure 3.12a – d, the distance between the stiff layer and fracture tip reduces, whereas the height percentage of soft layer is fixed. As illustrated in Table 3.4, there is less than 1% variation between the symmetric three

layer and various unsymmetrical three layer cases, suggesting the details of the layering is not important. The results reveal that the modified height-weighted harmonic average is a good approximate of the FEM effective modulus when the fracture tips lie in the soft layer, and the value of effective modulus is independent of layer location.

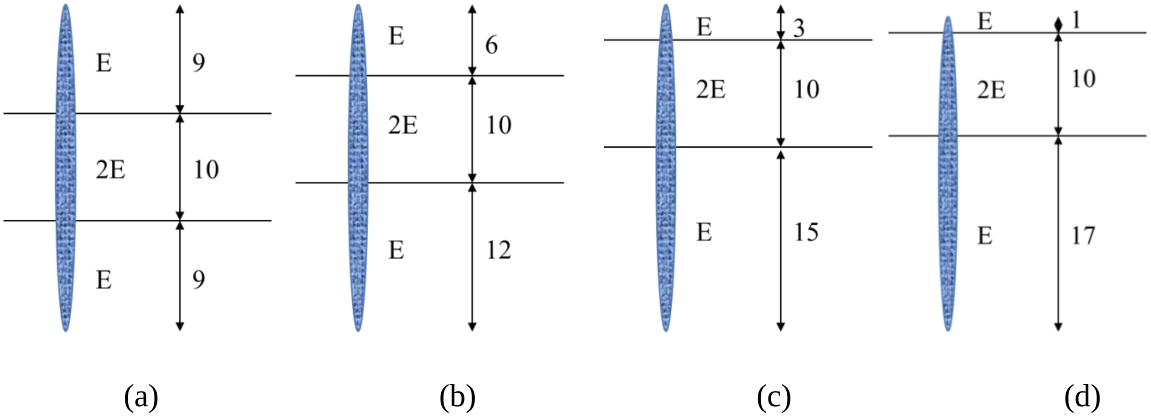

Figure 3.12. Illustration of layered reservoir-analog models with various layer locations when fracture tips are in the soft layer (a) the stiff layer lies in the middle; (b) the height ratio of top, middle, and bottom layers is 6:10:12; (c) the height ratio of top, middle, and bottom layers is 3:10:15; (d) the height ratio of top, middle, and bottom layers is 1:10:17. (E = 1 Mpsi)

Table 3.4. FEM effective modulus values of models in Figure 3.12 (The modified height-weighted harmonic average is 1.14 Mpsi)

Case number	(a)	(b)	(c)	(d)
FEM effective modulus, Mpsi	1.14	1.14	1.14	1.13

Figure 3.13 and 3.14 illustrate models with various layer locations when the fracture tips lie in stiff layers. In these models, the height percentage of stiff rocks is fixed and the moduli of soft and stiff layers are 1 and 2 Mpsi, respectively. As indicated in

Table 3.5 and 3.6, there is less than 1% variation among the symmetric three layer case, various five layer cases, and various unsymmetrical three layer cases, suggesting the details of the layering is not important. The estimated effective modulus based on the modified height-weighted approach is 1.66 Mpsi, which is a good approximate of the FEM effective modulus. The results reveal that the modified height-weighted mean is a good approximate of FEM effective modulus when the fracture tips lie in the stiff layer, and the details of layering are not important.

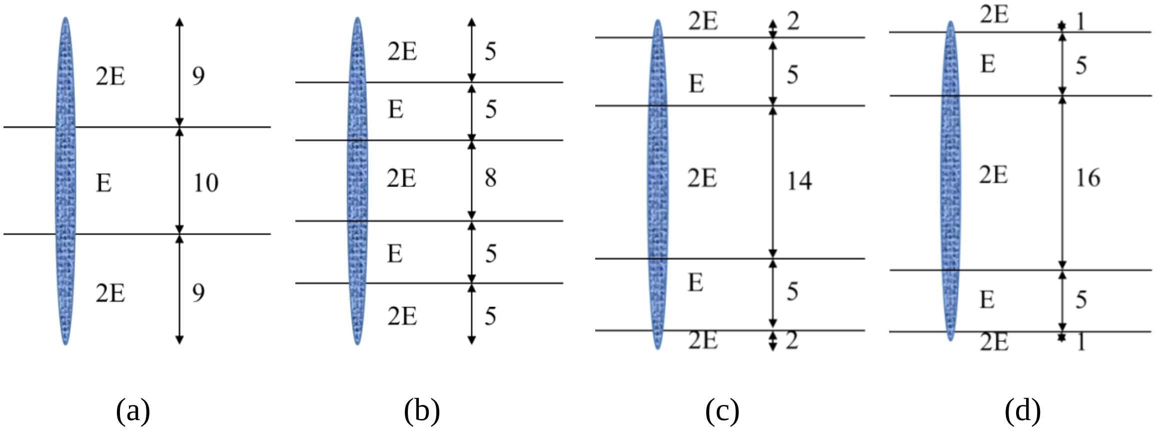

Figure 3.13. Illustration of layered reservoir-analog models with various layer locations when fracture tips are in the stiff layer. The distance between soft layers and fracture tip reduces from a to d. (*E* = 1 Mpsi)

Table 3.5. FEM effective modulus values of models in Figure 3.13 (The modified height-weighted mean is 1.66 Mpsi)

Case number	(a)	(b)	(c)	(d)
FEM effective modulus, Mpsi	1.67	1.67	1.66	1.65

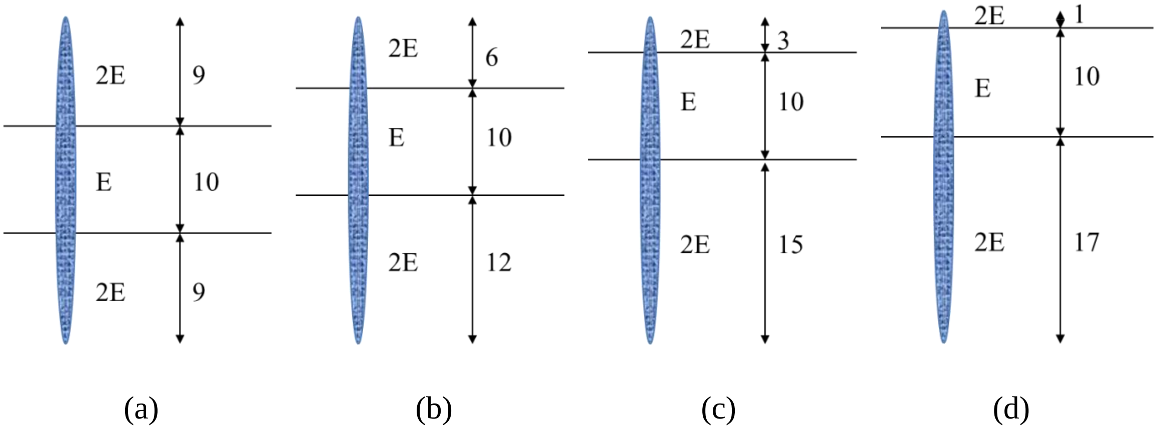

(a) (b) (c) (d)

Figure 3.14. Illustration of layered reservoir-analog models with various layer locations when fracture tips are in the soft layer (a) the soft layer lies in the middle; (b) the height ratio of top, middle, and bottom layers is 6:10:12; (c) the height ratio of top, middle, and bottom layers is 3:10:15; (d) the height ratio of top, middle, and bottom layers is 1:10:17. (*E* = 1 Mpsi)

Table 3.6. FEM effective modulus values of models in Figure 3.14 (The modified height-weighted mean is 1.66 Mpsi)

Case number	(a)	(b)	(c)	(d)
FEM effective modulus, Mpsi	1.67	1.67	1.66	1.65

3.4.1.4 Effect of the Number of Layers

In the previous section, we already showed that the details of layering are not important in three and five layer cases. In this section, you will further explore the impact of the number of layers on the effective modulus. Figure 3.15a shows a multi-layer reservoir analog model with alternating stiff and soft layers. Blue and red blocks represent stiff and soft layers, respectively. The stiff and soft layers have the same thickness and the moduli of soft and stiff layers are 1 and 2 Mpsi, respectively. Figure 3.15b shows the values of effective modulus with respect to fracture height when fracture is initiated in the soft layer. The blue dots show the values of the FEM effective modulus determined from numerical analysis. The red curve shows the analytical approximations of the effective modulus as fracture height increases. The effective modulus is estimated as the modified height-weighted mean (equation 3.15) when the fracture tip lies in the stiff layer, whereas the effective modulus is approximated as the modified height-weighted harmonic average (equation 3.14) when the fracture tip lies in the soft layer. As illustrated in the figure, the effective modulus jumps to a lower value when the fracture tip propagates from the stiff layer to the soft layer, whereas the effective modulus jumps to a higher value when the fracture tip penetrates into the stiff layer. Moreover, the effective moduli based on the modified height-weighted and modified harmonic averaging methods yield a good match with the FEM effective modulus.

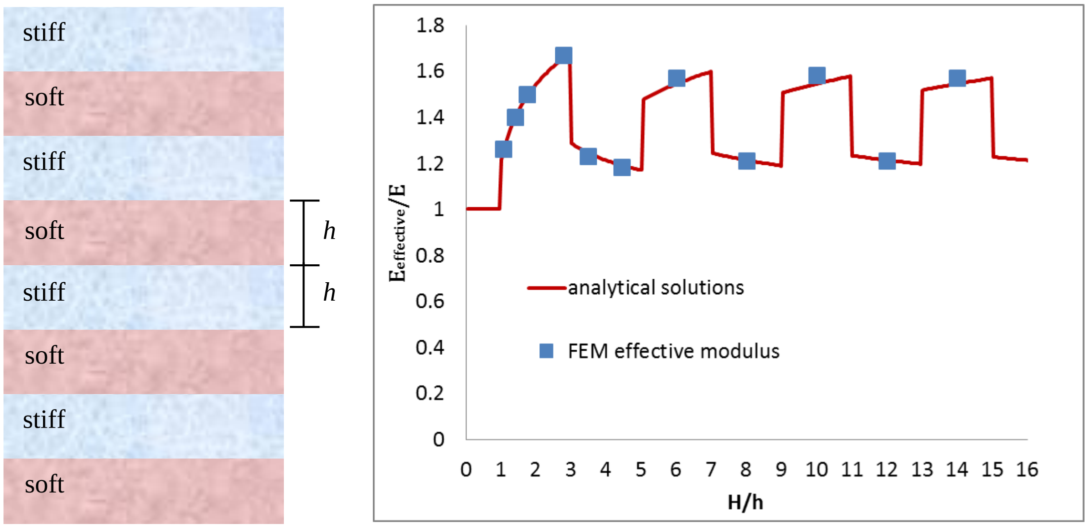

(a) (b)

Figure 3.15. (a) A multi-layer reservoir analog model with alternating soft and stiff layers. The moduli of soft and stiff layers are 1 and 2 Mpsi, respectively. The thickness of soft and stiff layers is equal to *h*. (b) Comparison of effective modulus between FEM and analytical approximations respective to number of layers. Fracture is initiated at the soft layer. (*E* = 1 Mpsi and *H* is fracture height)

3.4.2 Effect of Modulus Contrast on Fracture Height Growth

The effective modulus approximations, which are dependent on fracture tip location, can provide insight into fracture height containment due to modulus contrast. A flowchart that explains fracture height containment at soft layers is shown in Figure 3.16b. Considering a case of fluid-driven fracture propagating from a stiff layer to a soft layer (Figure 3.16a), the effective modulus of the layered reservoir decreases after the hydraulic fracture penetrates the interface because the fracture tip is freer to open in the soft layer that enhances fracture opening everywhere (Figure 3.5), yielding a lower effective modulus. Considering the change of fracture volume and height is negligible, the average fracture width remains the same after fracture penetrating the interface. According to equation (3.2), it could be concluded that the net pressure decreases due to the reduced effective modulus after hydraulic fracture penetrating into the soft layer. According to equation (3.16), the reduced net pressure leads to a smaller stress intensity factor after hydraulic fracture propagating from the stiff layer to the soft layer

$$K = P_{net}\sqrt{\pi H / 2} \tag{3.16}$$

According to LEFM, hydraulic fractures are expected to propagate if the stress intensity factor reaches the fracture toughness. Van Eekelen (1982) pointed out that the ranges of fracture toughness measured from laboratory testing are narrow for various kinds of rocks (siltstone, sandstone, limestone, and shale) and the values of fracture toughness are in the order of 1 MPa$\sqrt{m}$. Thus, fracture toughness of the stiff layer is considered equal to the fracture toughness of the soft layer. As a result, soft layers will inhibit hydraulic fracture propagation due to a reduced stress intensity factor.

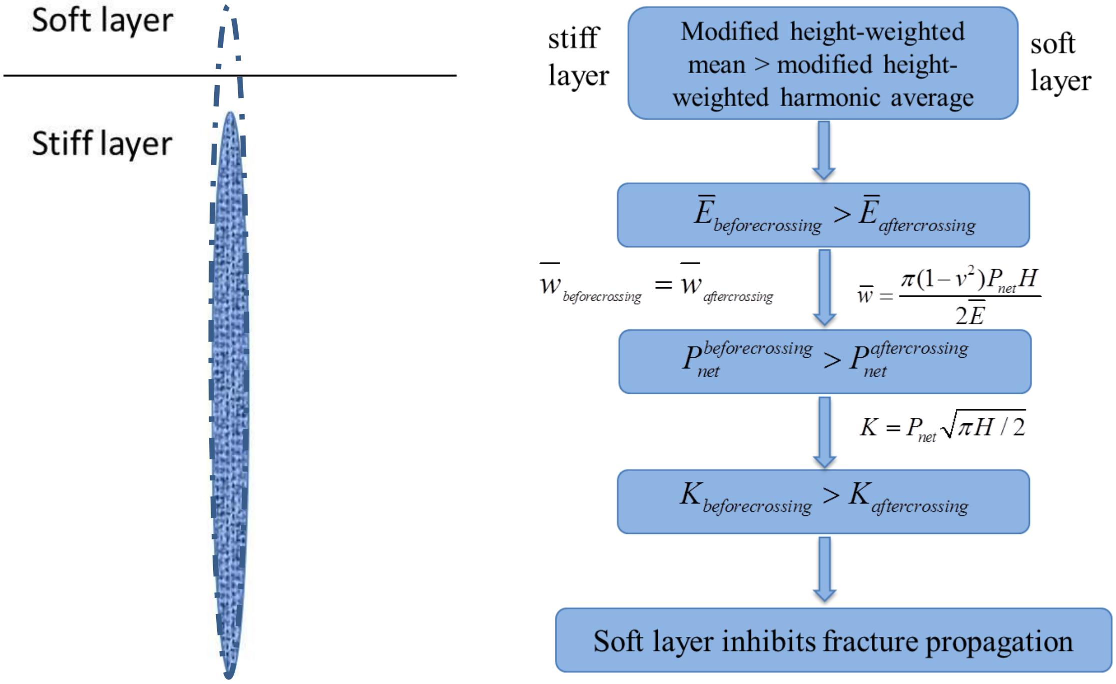

(a) (b)

Figure 3.16. (a) Illustration of a fracture propagating from the stiff layer to the soft layer. The dashed line indicates the fracture geometry after penetrating the interface, whereas the solid line indicates the fracture geometry before propagating into the soft layer. (b) Flow chart utilized in illustrating fracture height containment by the soft layer. The reduced effective modulus yields smaller net pressure when the fracture tip lies in the soft layer. Thus, the stress intensity factor is reduced, which contributes to the containment of fracture height at the soft layer.

3.4.3 Effect of Injection Location on Fracture Height Growth

The effect of injection location on fracture height growth could be evaluated based on the newly developed approximations of effective modulus. In this study, we are only considering fracture height growth in a two-dimensional plane strain system. Fracture length growth is being neglected but could be important for the results of a real case. A number of numerical simulations were performed with various fracture initiation locations. Because this study focuses on the effect of modulus, the variations of in-situ stress and fracture toughness between layers are neglected and the interface is considered to be perfectly bonded. In addition, leak-off effect is neglected, and thus injected fluid volume is equal to fracture volume. Figure 3.17 illustrates the work flow for fracture height growth in a layered reservoir. The fluid net pressure can be calculated based on equation (3.2), which yields

$$P_{net} = \frac{2\bar{E}V}{\pi(1-v^2)H^2} \tag{3.17}$$

where $\bar{E}$ is the effective modulus, V is fracture volume and H is the fracture height. As indicated in equation (3.17), net pressure increases with fracture volume and effective modulus, but decreases with fracture height. In this study, fracture propagation and height growth is evaluated if the stress intensity factor (K) reaches the fracture toughness (K_c). According to LEFM, the stress intensity factor can be expressed as

$$K = P_{net}\sqrt{\pi H/2} \tag{3.18}$$

If the stress intensity factor is greater than fracture toughness, fracture height will increase without the increase of fracture volume. However, if the stress intensity factor is less than fracture toughness, fracture height growth is inhibited. In that case, in order to make fracture propagate, fracture volume should be increased to yield higher net pressure. The critical net pressure could be calculated based on equation (3.18), which yields

$$P_{net}^{critical} = \frac{K_c}{\sqrt{\pi H/2}} \tag{3.19}$$

Thus, as indicated in equation (3.17), the required fracture volume can be calculated in terms of the critical net pressure and fracture height, which yields

$$V^{critical} = \frac{\pi(1-v^2)P_{net}^{critical}H^2}{2\bar{E}} = \frac{\sqrt{\pi}(1-v^2)K_c H^{3/2}}{\sqrt{2}\bar{E}} \tag{3.20}$$

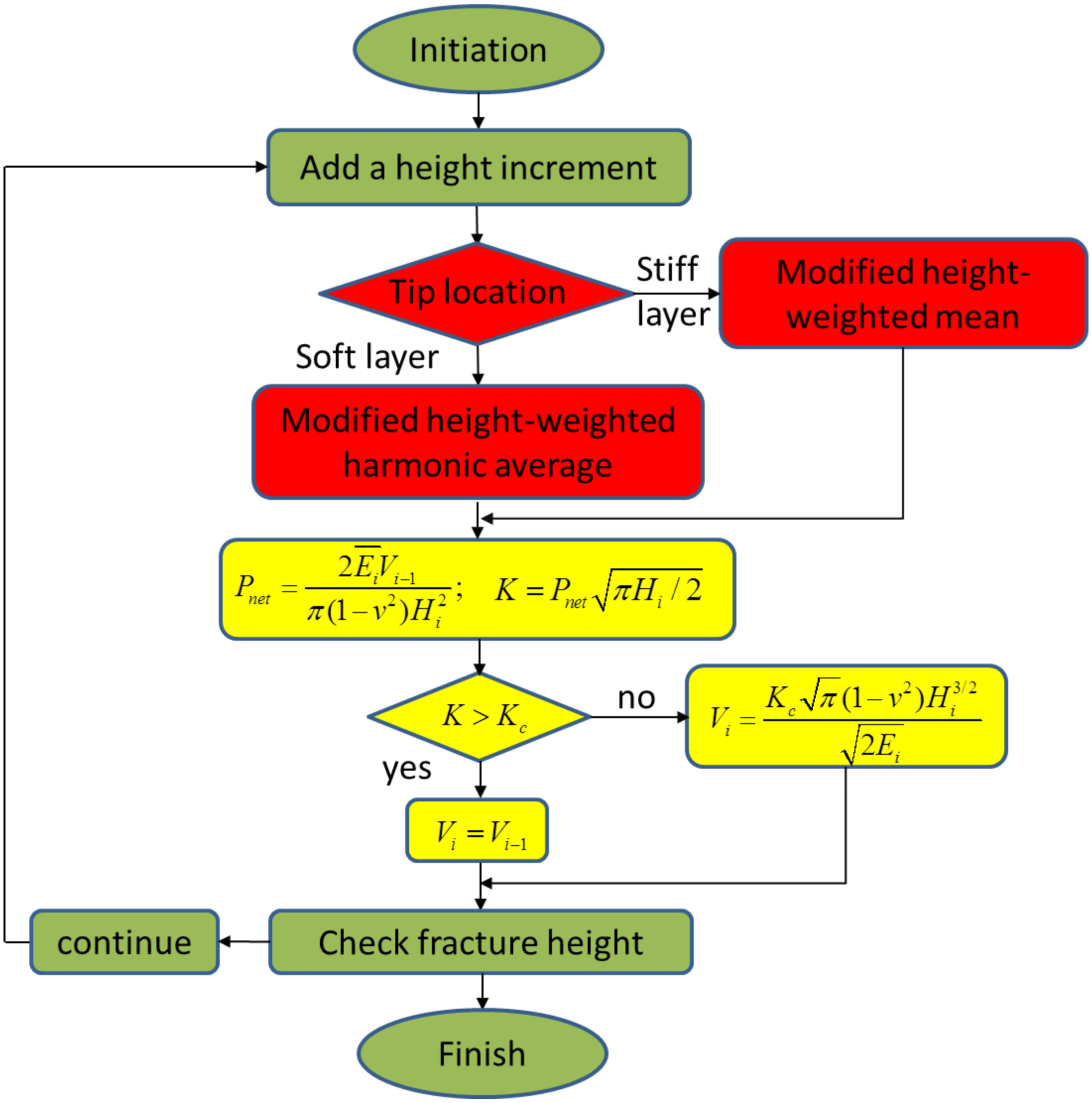

Figure 3.17. Flow chart for fracture height growth in layered medium. (*i* is the step number)

Figure 3.18 shows the comparison between analytical solutions and FEM results with respect to the relationship between the normalized fracture height and the normalized fluid volume when the fracture is initiated in the soft layer of a laminated reservoir (Figure 3.14a). In this case, the thicknesses of soft and stiff layers are both equal to h. The Young's moduli of the soft and stiff layers are 1 and 2 Mpsi, respectively. As illustrated in Figure 3.18, fracture height does not increase gradually, and instead it propagates unstably or is contained at the layer contact. For instance, at point A, the fracture tip is located at the contact surface between the soft and stiff layers (the outer layer is stiff), and the fracture height is $13h$. As illustrated in Figure 3.14b, the effective modulus increases at the fracture height of $13h$ when the fracture propagates from the soft layer to the stiff layer. As a result, the fluid net pressure exceeds the critical value when fracture penetrates into the stiff layer. Thus, the fracture height jumps from point A to B while the injected fluid volume does not change.

At point B, the fracture tip is at the contact between the stiff and soft layers (the outer layer is soft), and the fracture height is $15h$. As illustrated in Figure 3.14b, the effective modulus of a layered medium decreases at the fracture height of $15h$ when the fracture propagates from the stiff layer to the soft layer. As discussed in the previous section, fracture height growth is inhibited by the soft layer. Thus, from point B to C, the fracture height is contained at the contact between the stiff and soft layer until the fluid net pressure reaches the critical net pressure. From point C to D, fracture tips are in the soft layer and the fracture height gradually increases with the fluid volume until the fracture tip reaches the layer contact.

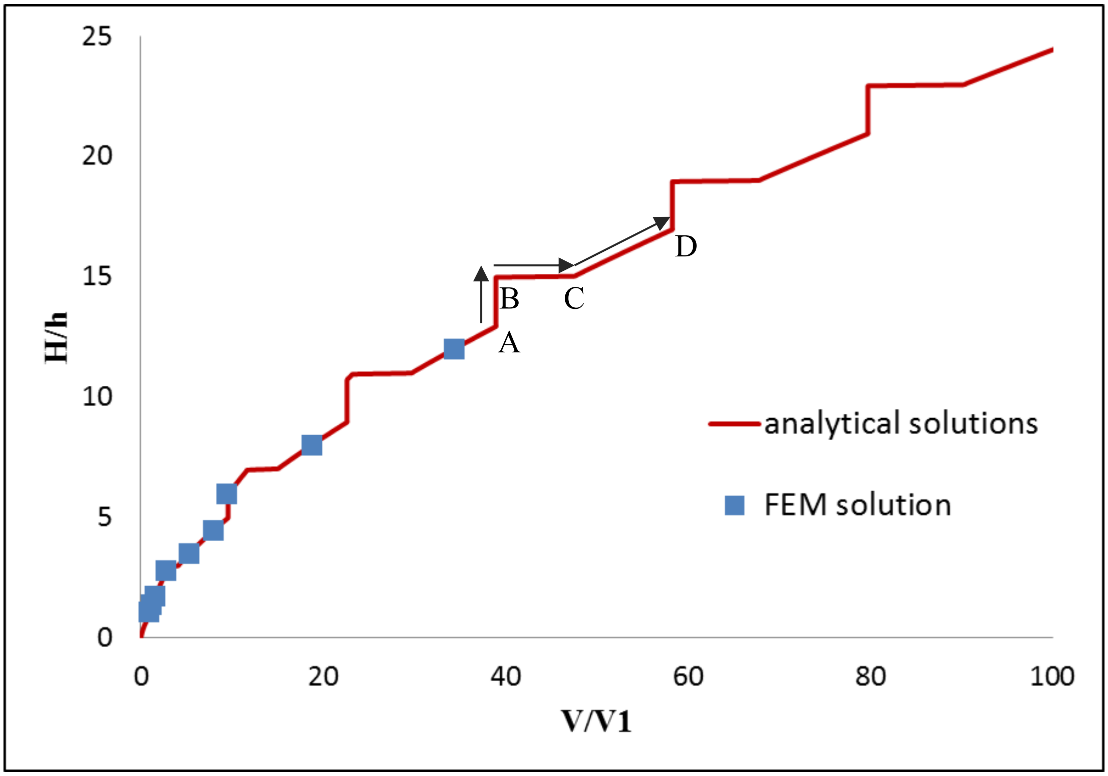

Figure 3.18. Normalized fracture height with respect to the normalized fluid volume when the fracture is initiated in the soft layer. Fracture height (H) is normalized by the layer thickness (h). Fracture volume (V) is normalized by V_1, which is the fracture volume when the fracture thickness is h. ($V_1 = \frac{\sqrt{\pi}(1-v^2)K_c h^{3/2}}{\sqrt{2}E}$).

Figure 3.19a illustrates the relationship between the normalized fracture height and the normalized fluid volume at different injection locations. In this case, the thicknesses of the stiff and soft layers are equal to *h*. The red curve shows fracture height with respect to injected fluid volume when the fracture is initiated in the stiff layer, whereas the blue curve shows the case when the fracture is initiated in the soft layer. By comparing the results at different injection locations, it is evident that injection location does not have the impact on fracture height if the effect of modulus contrast is considered.

Figure 3.19b shows the relationship between the normalized fracture height and the normalized fluid volume at different injection locations when the volume ratio of the stiff to soft rocks is equal to 0.25, 1, and 4. In these cases, the moduli of the soft and stiff layers are 1 and 2 Mpsi, respectively. The result reveals that fracture height is independent of injection location. However, the fracture height will increase with the height percentage of stiff rock.

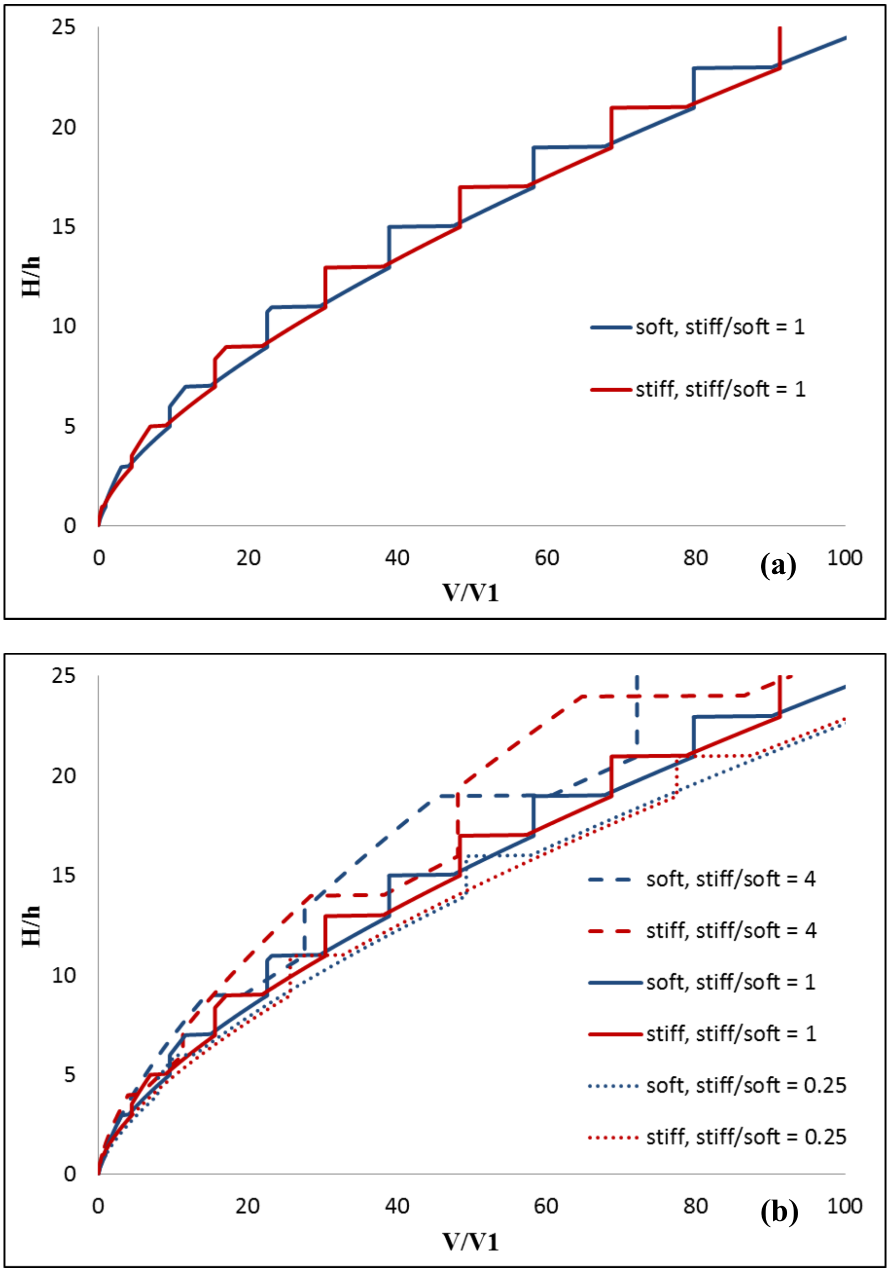

Figure 3.19. Relationship between the normalized fracture height and the normalized fluid volume at different injection locations (a) when volume ratio of the stiff to soft layer is equal to 1 (b) when volume ratios of stiff to soft layers are equal to 0.25 (dotted curve), 1 (solid curve), and 4 (dashed curve). ($V_1 = \frac{\sqrt{\pi}(1-v^2)K_c h^{3/2}}{\sqrt{2}E}$, The blue and red curves show fracture initiation at the soft and stiff layers, respectively.)

3.5 Discussion

3.5.1 Effect of Mechanical Anisotropy

In this study, the approximations of effective modulus are empirically derived by assuming homogeneous mechanical properties of layers. However, rocks in unconventional reservoirs exhibit significant mechanical anisotropy due to the organized distribution of compliant organic materials (Vernik and Liu, 1997; Vernik and Milovac, 2011) and clay minerals (Johnston and Christensen, 1995). Sone and Zoback (2013) conducted laboratory measurements to calculate the ratio of horizontal to vertical Young's moduli for rocks from various shale plays. Figure 3.20 shows that the degree of mechanical anisotropy increases with soft component volume. The ratio of horizontal to vertical Young's modulus varies between 1 and 4 for rocks from various unconventional reservoirs.

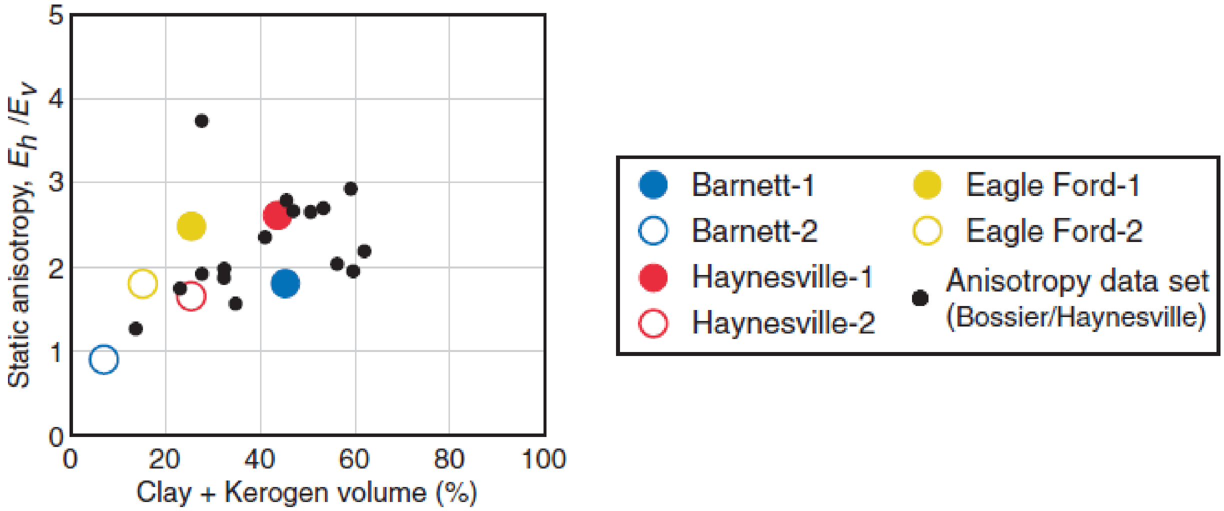

Figure 3.20. The ratio of horizontal to vertical Young's modulus with respect to the sum of clay and kerogen volume. (Sone and Zoback, 2013)

In this section, finite element analysis was utilized to investigate the effect of mechanical anisotropy on effective modulus. The numerical model is illustrated in Figure 3.1. A net pressure of 300 psi is applied on the fracture surface and the horizontal Young's modulus is fixed to be 4 Mpsi. To take into account the effect of mechanical anisotropy, various vertical Young's moduli were utilized: 1, 2, 3, and 4 Mpsi. Figure 3.21a shows the comparison of fracture width profiles between various ratios of horizontal to vertical Young's moduli. The results show that fracture width increases as the level of mechanical anisotropy increases when the horizontal Young's modulus is fixed. The comparison of fracture width profiles also shows that fracture opening is mainly affected by the horizontal Young's modulus and the effect of mechanical anisotropy is small.

The values of effective modulus are calculated based on the fracture width profiles illustrated in Figure 3.21a. Figure 3.21b illustrates the normalized effective moduli with respect to the ratios of horizontal to vertical Young's modulus. According to Figure 3.21b, the difference between the effective modulus and horizontal modulus increases as the level of mechanical anisotropy increases. When the ratio of horizontal to vertical moduli is four, the effective modulus yields a difference of 9% relative to the horizontal modulus. The results indicate that it is appropriate to neglect the effect of mechanical anisotropy in the derivation of effective modulus.

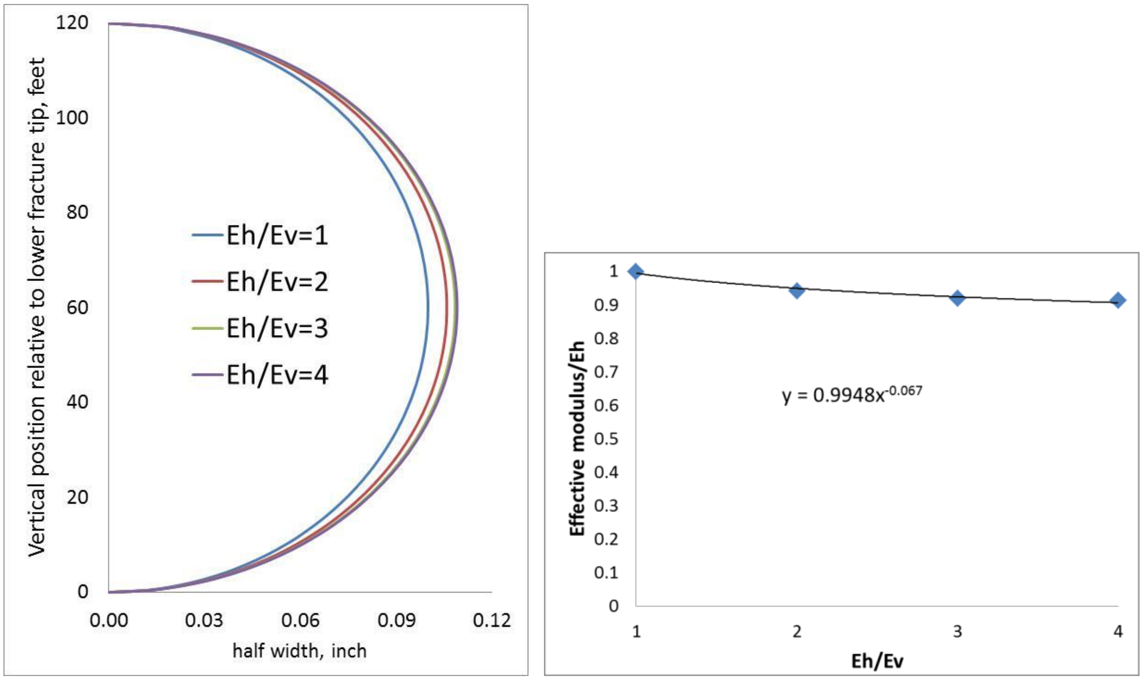

(a) (b)

Figure 3.21. (a) Comparison of fracture width profiles between various levels of mechanical anisotropy. The ratios of horizontal to vertical Young's moduli are 1, 2, 3, and 4. (b) Effective modulus with respect to the ratio of horizontal to vertical Young's moduli.

3.5.2 Arbitrary Modulus

The approximation of effective modulus derived in this study only considers two types of layers with contrasting modulus values. This might be a good approximation of the layer properties of the transgressive-regressive cycles within the layered formation (Donovan and Staerker, 2010; Workman, 2013; Ferrill et al., 2014). However, for more practical application, the effective moduli require further modification by considering more than two types of layers. In this section, we provide guidelines to derive effective modulus approximation for cases with arbitrary modulus.

Figure 3.22a and b show two layered models with arbitrary modulus when fracture tips lie in soft and stiff layers, respectively. These models contain fourteen layers with five types of moduli. Other than layers 1 and 14, layers 2-13 are in random order. Models in Figure 3.22a and b contain the same distribution of layers 2-13. However, fracture tips in Figure 3.22a lie in layers with modulus of 1 Mpsi, whereas fracture tips in Figure 3.22b lie in layers with modulus of 5 Mpsi. As indicated in the previous section, the effective modulus of a layered system is not affected by details of layering. As a result, the first step of our approach in deriving the approximation of effective modulus of a layered system with arbitrary modulus is to obtain the effective modulus of the fracture body (layers 2-13). In this manner, the layered model with arbitrary modulus can be transformed to a three-layer model. The second step is to apply the modified height-weighted mean or modified height-weighted harmonic average to evaluate the effective modulus of the three-layer model, depending on the fracture tip location.

In this study, we utilized three types of approximation to calculate the effective modulus of layers 2-13, namely height-weighted mean, height-weighted harmonic average, and the mean of height-weighted mean and harmonic average. Table 3.7 and 3.8 show the effective modulus values of models in Figure 3.22a and b, respectively. The height-weighted mean and harmonic average of layers 2-13 are 2.8 and 2.2 Mpsi, respectively. The mean of height-weighted mean and harmonic average of layers 2-13 is 2.5 Mpsi. Based on the numerical analysis, the FEM effective moduli for models in Figure 3.22a and b are 1.5 and 3.3 Mpsi, respectively. As indicated in Table 3.7 and 3.8, if the mean of height-weighted mean and harmonic average is utilized as the effective modulus of layers 2-13, the effective moduli of models in Figure 3.22a and b are approximated to be 1.5 and 3.3 Mpsi, respectively. The results show that the mean of height-weighted mean and harmonic average is a good approximate to calculate the effective modulus of layers inside the fracture body with arbitrary modulus. The approach proposed in this study is a good starting point to develop the effective modulus of layered systems with arbitrary modulus.

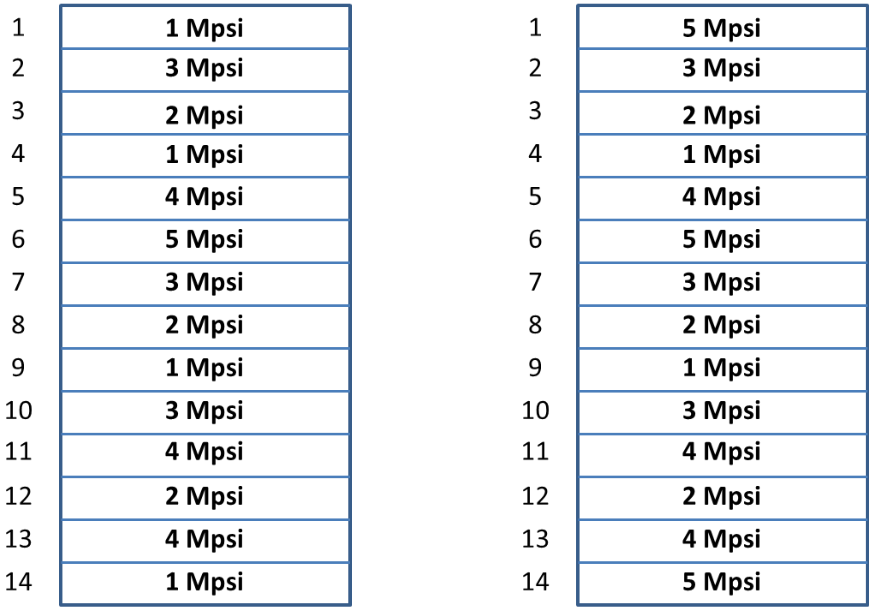

(a) (b)

Figure 3.22. Illustration of layered systems with arbitrary modulus when fracture tips lie in (a) soft and (b) stiff layers.

Table 3.7. Effective modulus values of models in Figure 3.22a

Effective modulus approximation of Layer 2-13		
Height-weighted mean	Height-weighted harmonic average	½(height-weighted mean + harmonic average)
2.8 Mpsi	2.2 Mpsi	2.5 Mpsi
Modified height-weighted harmonic average of Layer 1-14		
1.6 Mpsi	1.4 Mpsi	1.5 Mpsi

Table 3.8. Effective modulus values of models in Figure 3.22b

Effective modulus approximation of Layer 2-13		
Height-weighted mean	Height-weighted harmonic average	½(height-weighted mean + harmonic average)
2.8 Mpsi	2.2 Mpsi	2.5 Mpsi
Modified height-weighted mean of Layer 1-14		
3.6 Mpsi	3 Mpsi	3.3 Mpsi

3.6 Conclusions

In this study, finite element analysis was applied to investigate the effective modulus of a layered reservoir. Modified averaging methods were empirically derived to evaluate the effective modulus by comparing to the FEM effective modulus. The results showed that the height-weighted mean and height-weighted harmonic average predicted effective modulus well for their perspective tip location at stiff and soft layers, respectively, given a three layer case with the 9: 10: 9 layer thickness ratio. The basic averages did not work as well at different layer thickness ratios, but we were able to empirically derive a set of correction factors that gave very good accuracy over a wide range of height percentages of soft layers between 0.07 and 0.93 and modulus ratios of stiff to soft rocks between one and five. This study also showed that the details of layering did not impact the value of effective modulus and the only important parameters were fracture tip locations, modulus values, and the height percentage of each rock layer.

This study also investigated the effect of mechanical anisotropy on the effective modulus, given the ratio of horizontal to vertical Young's modulus as one, two, three, and four. The results showed that the difference between the effective modulus and horizontal modulus increases as the level of mechanical anisotropy increases. When the ratio of horizontal to vertical moduli is four, the effective modulus only yields a difference of 9% relative to the horizontal modulus. Thus, fracture opening is mainly affected by the horizontal modulus and it is appropriate to neglect the effect of mechanical anisotropy in the derivation of effective modulus.

The averaging methods developed in this work could also contribute to the evaluation of hydraulic fracture height containment. This study suggested that soft layers inhibit hydraulic fracture propagation in layered reservoirs. As a result, hydraulic fracture height containment within a stratified rock stack can be better evaluated by comparing the modulus contrast between adjacent layers.

The results also suggested that hydraulic fracture height growth in a well-laminated reservoir is not affected by fracture initiation location, and instead fracture height will increase with the height percentage of stiff rock layers. In this study, the effect of fracture initiation and inelastic effects were not considered but could be important for the real cases.

CHAPTER 4: NUMERICAL INVESTIGATION OF FRACTURE OFFSET AT A FRICTIONAL BEDDING PLANE UNDER IN-SITU STRESS CONDITIONS

4.1 Introduction

Rock heterogeneity occurs in many oil and gas formations (Rodrigues et al. 2009; Ferrill et al. 2014; Wang and Gale, 2016). Due to sedimentary lamination, the variations of in-situ stresses and mechanical properties of rocks in the vertical direction are more significant compared to the horizontal variations, which contributes to the noticeable restriction of fracture height growth.

Understanding fracture height growth across bedding planes is of great interest in hydraulic fracturing. Given its importance, hydraulic fracture propagation in the vertical direction and height containment have been extensively studied by numerical modeling (Simonson et al. 1978; Zhang et al. 2007; Zhang and Jeffrey, 2008; Gu and Siebrits, 2008; Ouchi, 2016), laboratory testing (Daneshy, 1976; Teufel and Clark, 1984; ALTammar and Sharma, 2017), and mine-back tests (Warpinski et al. 1982). The results indicate that fracture geometry is complex and fracture height is mainly affected by the heterogeneities of both in-situ stresses and mechanical properties, as well as the interface properties of bedding planes. Among all the factors, the variation of in-situ stresses between adjacent layers is considered to be the dominant mechanism on fracture height containment in the majority of field cases (Jeffrey and Bunger, 2007), whereas interface sliding and fracture termination are expected at weak interfaces.

When hydraulic fractures meet bedding planes, fractures can either penetrate through bedding planes or may be arrested at the interface due to tip blunting (Thiercelin et al. 1987). Other than the above extreme cases, hydraulic fractures may be deflected into the interface or may reinitiate a new fracture at the opposite layer to form an offset pattern. According to Daneshy (1976), fracture termination is possibly associated with shear slip at the interface. Based on Renshaw and Pollard (1995), fracture propagation through frictional interfaces will be inhibited if shear slip occurs before the initiation of new fractures at the opposite layer. Moreover, according to numerical analysis (Zhang and Jeffrey, 2008; Abbas et al. 2014), offsets in the propagation path could contribute to fracture height containment. Once an offset is created, the reduced opening at the offset may result in proppant bridging or plugging (Daneshy, 2003). In addition, the offset may also act as a barrier for fluid flow, and thus fracture height growth is limited compared to a planar fracture. Thus, limited fracture height growth is influenced by fracture offset and shear slip at the interface.

Numerous studies have evaluated fracture offset at a bedding plane (Cooke and Underwood, 2000; Zhang et al. 2007; Zhang and Jeffrey, 2008; Ouchi, 2016; Ouchi et al, 2017; Al Tammar and Sharma, 2017). However, few studies investigated fracture offset under the in-situ stress condition, where hydraulic fractures are initiated at a depth of a few thousand meters. Furthermore, few studies were available to investigate the effect of modulus contrast independently because the difference of modulus would yield in-situ stress contrast between layers (Zhang and Jeffrey, 2008).

In this study, a two-dimensional finite element model was utilized to investigate fracture offset at a bedding plane under the in-situ stress state. Various factors are investigated: in-situ stress contrast between adjacent layers, modulus contrast between adjacent layers, interface strength, reservoir depth, pore pressure, and fracture toughness. By examining fracture offset and shear slip at a bedding plane, this study can provide insight into massive fracture height containment in the field.

4.2 Methodology

This approach is developed based on Cooke and Underwood (2000)'s study, in which the impact of interface sliding and opening on fracture termination and offset at the interface were studied. Once the interface opens or slips, the distribution of the maximum tensile stress along the top and bottom interface surfaces might be different due to the anti-symmetry of stresses along the interface (Lawn et al. 1993). According to Cooke and Underwood (2000), the potential of fracture crossing, termination at, or offset at a bedding plane is investigated by examining the distribution of the maximum tensile stress along the top surface of the interface. If the greatest maximum tensile stress exceeds the tensile strength of the rock, a new fracture will be initiated, resulting in fracture propagating across or offset at the interface; otherwise the parent fracture is contained. If the maximum tensile stress develops at either side of the parent fracture, new fractures are expected to initiate away from the direction of the parent fracture, yielding fracture offset. Moreover, shear slip along the interface would promote fracture offset and might yield fracture containment at the interface.

In this study, the commercial finite element software ABAQUS (Dassault Systèmes, 2013) was utilized to evaluate the maximum tensile stress and interface failure at the interface. Compared to the Boundary Element Method (BEM) that was utilized in Cooke and Underwood (2000)'s study, Finite Element Method (FEM) is more capable in dealing with material heterogeneity and discontinuous problems (Jing, 2003). BEM only discretizes the boundary with a finite number of elements and solutions inside the domain are continuous, whereas FEM discretizes the whole domain and solutions inside the domain can be discontinuous. Thus, BEM is suitable in solving homogenous and linear elastic problems, whereas FEM is more powerful in solving inhomogeneous and nonlinear problems, which is the case in our study.

Figure 4.1 illustrates a two-dimensional plane strain model with an opening-mode fracture approaching an interface between two dissimilar layers. Owing to geometric symmetry, only half of the model is simulated with a symmetric displacement constraint. Fracture propagation towards the interface is simulated by decreasing the distance between fracture tip and interface, *S*. Propagation of the vertical fracture is driven by a uniform compressive stress, which is utilized to mimic fluid pressure inside the hydraulic fracture. In our study, fluid flow inside fracture and viscous dissipation in the fluid is neglected. Uniform compressive stress is applied on top of the model to simulate the overburden stress and the bottom of the model is constrained in the vertical displacement. In addition, remote compressive stresses are applied on the right side of the model to simulate in-situ horizontal stresses. The effect of modulus contrast between adjacent layers is investigated by varying the modulus values between layers, whereas the effect of in-situ stress contrast between adjacent layers is investigated by changing the horizontal stresses acting on layers.

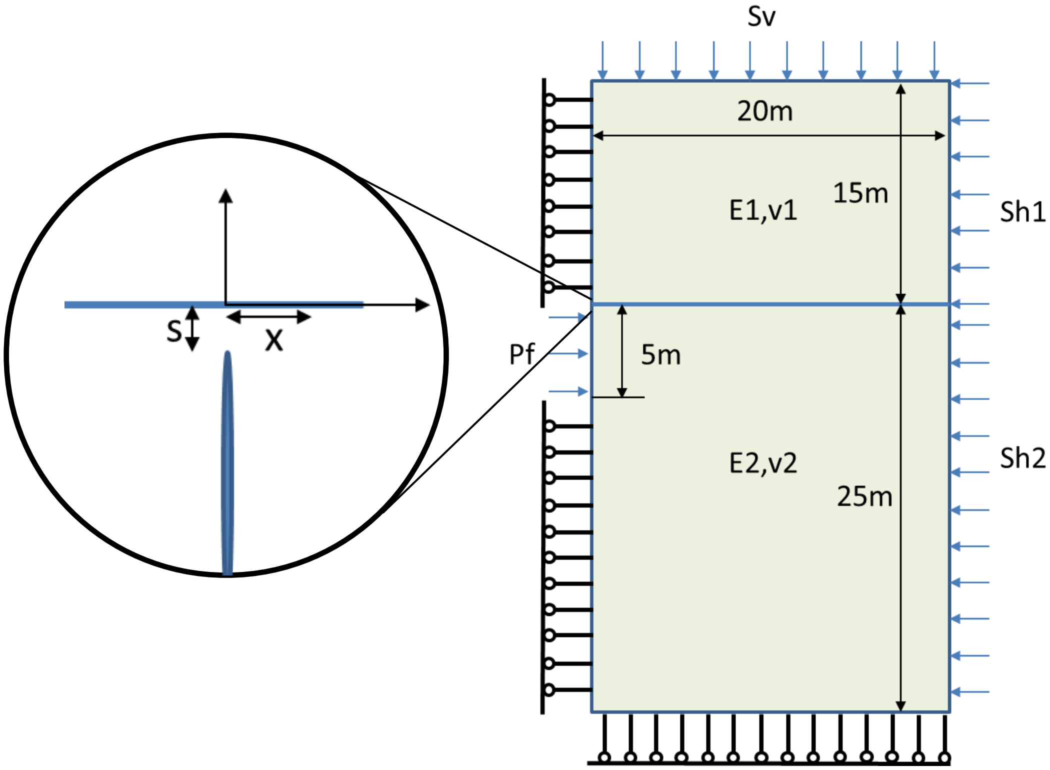

Figure 4.1. Configuration of a two-dimensional model. An opening-mode fracture approaches an interface. *S* is the distance between the fracture tip and the interface, *x* is the distance relative to the parent fracture in the horizontal direction. The boundary condition on the left side of model is only free to slide in the vertical direction, whereas the bottom of model is only free to slide in the horizontal direction.

In this study, a user subroutine is developed to simulate interface sliding and opening. Compared to the implemented interface model in ABAQUS, this subroutine also takes into account cohesion and tensile strength. In the interface model, the constitutive parameters include friction coefficient μ, interface tensile strength T, and interface cohesion c. Shear slip and debonding of the interface are dependent on the stress state. In the meanwhile, shear slip and debonding at the interface will also alter the stress state along the interface. The interface will open if the normal stress acting on the interface exceeds the tensile strength of the interface, which yields

$$\sigma > T \tag{4.1}$$

where σ is tensile stress normal to the interface (this study utilizes the compression negative sign convention). When debonding occurs, normal and shear tractions on the debonded interface elements become zero. In addition, shear slip will occur if the Coulomb friction criterion is satisfied,

$$|\tau| > c - \mu\sigma \tag{4.2}$$

where τ is the shear stress acting on the interface. Once shear slip occurs, the cementation or bonding of the interface will break, yielding zero cohesion and tensile strength along the interface elements. When debonding or shear slip occurs, the stress state of the whole system must be recalculated because the failure of the interface element may alter the stress state of the adjacent elements. Moreover, change of stress state in the adjacent interface elements may yield additional debonding or shear slip along the interface. In ABAQUS, the calculation process is automatically repeated until a convergent solution is obtained.

As illustrated in Table 4.1, the overburden stress is -55 MPa, corresponding to a depth of burial of about 2400 meters. The initial reservoir pore pressure is usually abnormally high in shale formations (Xiong et al. 2015). In the base case, the pore pressure gradient is chosen to be 0.7 psi/ft, which is a good estimate of Eagle Ford formation. Thus, the initial pore pressure is 38 MPa. The value of the minimum horizontal stress is calculated to be -44 MPa based on the critically stressed fault theory (Zoback, 2007). According to the experimental results in Schmidt and Huddle (1976), fracture toughness of rocks increases with confining pressure and the value is on the order of 3 MPa$\sqrt{\mathrm{m}}$ under the confining stress of -44 MPa. Thus, the fracture toughness is chosen to be 3 MPa$\sqrt{\mathrm{m}}$, yielding an applied pressure of 45.08 MPa acting on the fracture surface. The modulus and Poisson's ratio of layers are 13.8 GPa (2 Mpsi) and 0.2, respectively.

Figure 4.2 shows the comparison of shear stress along the interface between the numerical and analytical near-tip solutions, which is given as

$$\sigma_{xy} = \frac{P_{net}\sqrt{l}}{\sqrt{2r}} sin\frac{\theta}{2} cos\frac{\theta}{2} cos\frac{3\theta}{2} \tag{4.3}$$

where σ_{xy} is shear stress, *r* is the distance relative to the fracture tip, θ is the angle relative to the fracture propagation direction in the polar coordinate, P_{net} is the fracture net pressure, and *l* is the fracture half-height. Figure 4.2 illustrates the comparison of shear stress along the interface when the distance between the fracture tip and the interface is 0.5, 1, and 2 cm for a bonded interface. Figure 4.2a shows the comparison of the near-tip shear stresses, whereas Figure 4.2b shows the comparison of the far-field shear stresses along the interface. The solid and dotted curves show the numerical and analytical solutions, respectively. The results show that the numerical results of the near-tip region yield a good agreement with the analytical near-tip solutions. In this study, only the stress values near the fracture tip, where the high stress concentration occurs, are utilized to evaluate fracture crossing behavior at a bedding plane. The near tip stress field in this study is based on LEFM, which is limited to the small scale yielding (SSY) condition. For the SSY condition, the requirement of fracture half-length is expressed as (Ouchterlony, 1990)

$$l \geq 15.6R_c \tag{4.4}$$

where l is fracture half-length and R_c is the process zone size. When the condition is satisfied, fracture toughness is independent of fracture length. In this study, the stress intensity factor is considered to be equal to fracture toughness, thus, the near-tip stress state is also independent of fracture length.

As discussed in Chapter 2, LEFM is an appropriate approach to evaluate the near-tip stress field outside the process zone for fluid-driven fractures under confining stress. When the confining stress exceeds the tensile strength of rocks, the process zone size is mainly dependent on the confining pressure and fracture toughness, which is given as

$$R_c \approx \frac{\pi}{8}(\frac{K_c}{S})^2 \tag{4.5}$$

where K_c is fracture toughness, and S is the confining stress. The size of process zone is on the order of 0.2 cm when the fracture toughness and confining stress are 3 MPa$\sqrt{\mathrm{m}}$ and -44 MPa, respectively. Thus, the minimum fracture half-length is calculated to be 3cm. As illustrated in Table 4.1, the initial fracture length is five meters, which exceeds the minimum fracture length. As a result, the near-tip stress state in our study is mainly dependent on fracture toughness and independent of fracture length.

Table 4.1. Parameters of the fracture model

Parameters	Values
Sh_1/Sh_2 (MPa)	44; ~0.8 psi/ft
E_1, E_2 (GPa)	13.8
v_1, v_2	0.2
S_v (MPa)	55; ~ 1 psi/ft
Depth (meters)	2400
Pore pressure (MPa)	38; ~0.7 psi/ft
Fracture toughness (MPa$\sqrt{m}$)	3
Fracture pressure (MPa)	45.08

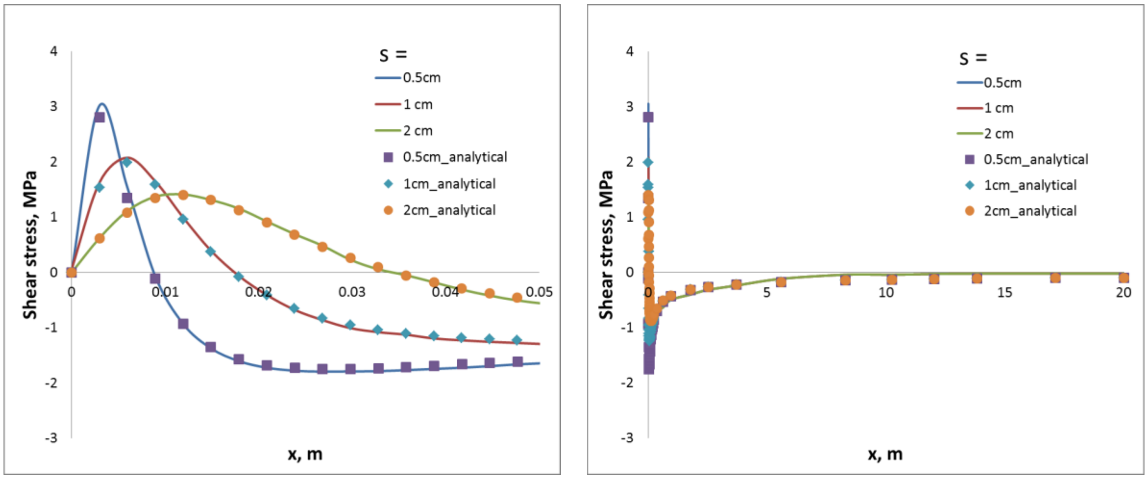

(a) (b)

Figure 4.2. Comparison of shear stresses at the interface between analytical and numerical results for (a) near-tip and (b) far field solutions when the distance between fracture tip and interface is 0.5, 1, and 2 cm. (*S* is the distance between fracture tip and interface)

In this study, one of the biggest challenges lies in applying the correct in-situ stresses for each layer. When using stress boundary conditions in a model with layers of different Young's modulus, there will be a discrepancy in displacement between layers, yielding residual stresses near the frictional interface. Thus, the stresses in the layers are not equal to the applied remote stresses. In order to overcome this challenge, the geostatic analysis in ABAQUS is utilized to compute the correct in-situ stress state before simulating the opening-mode fracture.

The geostatic procedure is normally utilized as the first step to establish the initial equilibrium under the in-situ stress state. In the geostatic procedure, the interface is frictionless, while the remote in-situ stresses and pore pressure are applied. Moreover, the compressive stress applied on the fracture surface is equal to the remote horizontal stress. In the model, the pore pressure is 38 MPa and the horizontal compressive stresses in the top and bottom layers are -49 and -44 MPa, respectively. At the end of the geostatic step, the stress state is in equilibrium and the stresses in the layers are equal to the effective stresses, which are the difference between the applied remote stresses and pore pressure. Figure 4.3 shows the effective stress state after the geostatic step. The effective overburden stress is -17 MPa; whereas the effective horizontal stresses in the top and bottom layers are -11 and -6 MPa, respectively. After the geostatic step, the interface is changed to be frictional and the opening-mode fracture is pressurized, thus the stress state due to fracture can be investigated.

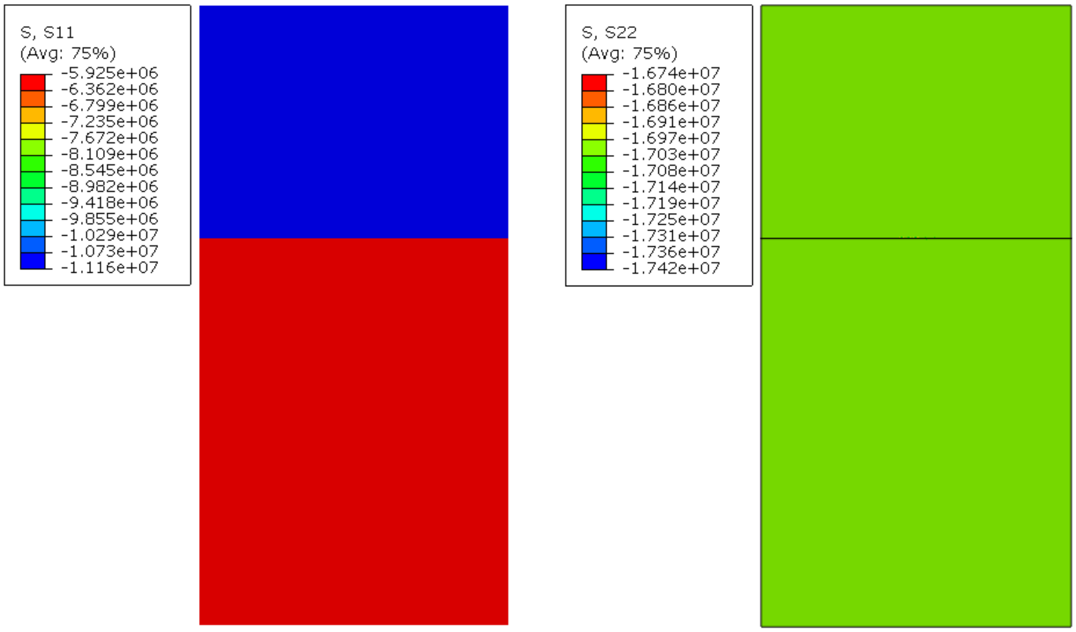

(a) (b)

Figure 4.3. Illustration of the stress state after the geostatic step: (a) S_{11} (S_{xx}) and (b) S_{22} (S_{yy}). (The effective overburden stress is -17 MPa. The effective horizontal stresses in the top and bottom layers are -11 and -6 MPa, respectively)

Based on the previous analysis, the process zone size is on the order of 0.2 cm based on the provided fracture toughness and confining stress. Thus, in our study, the distance between the fracture tip and interface is greater than 0.2 cm. Figure 4.4a illustrates the contour of the maximum principal tensile stress when the distance between the fracture tip and interface is 1 cm. Figure 4.4b shows the distribution of the maximum principal tensile stress along the interface when the distance between the fracture tip and interface is 0.5, 1, 2, 3, 5, 8, and 12 cm for a bonded interface. Fracture propagation is simulated by decreasing the distance between the fracture tip and interface. Based on the stress criterion of fracture initiation, a new fracture will be initiated when the maximum tension exceeds the tensile strength of the rock. Thus, a new fracture is most likely to occur at the location of the greatest maximum tension.

In Figure 4.4b, the dashed curve shows the distribution of the greatest maximum tensile stress along the top surface of the interface as fracture tip approaches the interface. As shown in the figure, the greatest value of the maximum tensile stress increases as the distance between the fracture tip and interface decreases. When the distance between the fracture tip and interface is greater than 5cm, the greatest maximum principal stress is compression and thus fracture initiation will not occur. According to the tensile stress criterion, the offset distance decreases with increasing the tensile strength of top layer rock. According to the experimental results in Weinberger et al. (1994), the tensile strength of rocks depends slightly on the confining pressure and the mean value of tensile strength is on the order of 5 MPa for various types of rocks. For the sake of simplicity, the tensile strength of rocks is chosen to be 5 MPa in this study and the value is assumed independent of confining pressure. Thus, the initiation of a new fracture occurs when the distance between the fracture tip and interface is between 1 and 2 cm. The results indicate that a new fracture is initiated at the top surface of interface before the fracture tip reaches the interface. For the base case, the distribution of the maximum principal tensile stress is analyzed when the distance between the fracture tip and interface is 1, 2, and 3 cm.

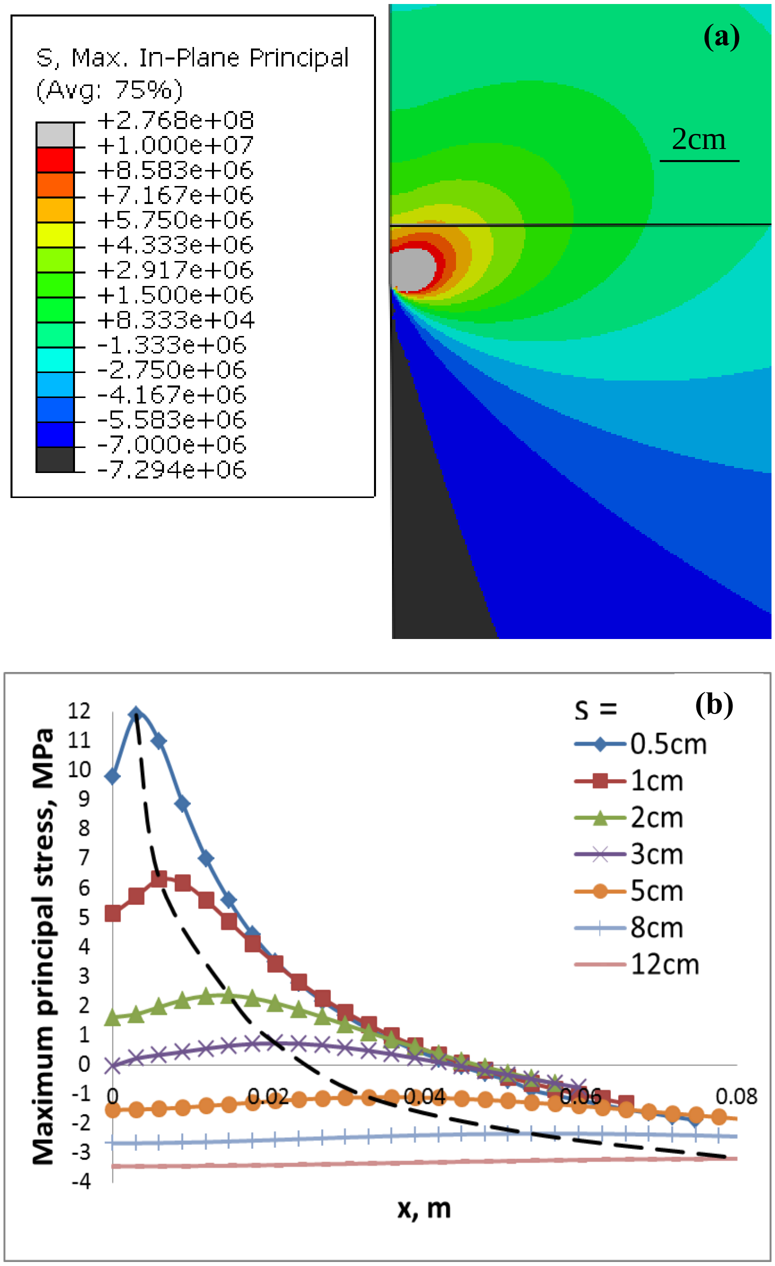

Figure 4.4. (a) Contour of the maximum principal tensile stress along the top surface of the interface when the distance between the fracture tip and interface is 1 cm. (b) The distribution of the maximum principal tensile stress along the interface when the distance between the fracture tip and interface is 0.5, 1, 2, 3, 5, 8, and 12 cm. The dashed curve shows the distribution of the greatest maximum tension as fracture tip approaches the interface. (*S* is the distance between fracture tip and interface)

4.3 Numerical Results

4.3.1 The Effect of Interface Strength

In this section, we investigate the effect of interface strength on fracture crossing, offset, and termination at a bedding plane. As illustrated in Table 4.2, three types of interface are investigated in this study. The strong interface is bonded, whereas the weak interface has a friction coefficient of 0.2. According to Bastola and Chugh (2015), the average friction coefficient and cohesion of various types of bedding planes are around 0.6 and 0.4 MPa, respectively. Thus, the friction coefficient and cohesion of the moderate-strength interface are chosen to be 0.6 and 0.4 MPa, respectively. If a linear Mohr-Coulomb envelope is assumed (Cooke and Underwood, 2000), the tensile strength is estimated based on equation (4.1) and (4.2), which yields

$$T = \frac{c}{\mu} \tag{4.6}$$

Thus, the tensile strength of the moderate-strength interface is chosen to be 0.7 MPa.

Table 4.2. Parameters of various types of interface

Interface types	Friction coefficient	Tensile strength, MPa	Cohesion, MPa
strong	infinite	infinite	infinite
moderate	0.6	0.7	0.4
weak	0.2	0	0

Figure 4.5a shows the distribution of normal stress along the interface as the fracture approaches the strong interface. When the interface is perfectly bonded, the least compressive stress occurs at $x = 0$, due to the tensile stress induced by the opening-mode fracture. When the distance between fracture tip and interface is 1 cm, the least compressive stress is around -5.6 MPa, which indicates that debonding is unlikely to occur ahead of the fracture tip. The results also show that normal stress decays as x increases and finally reaches -17 MPa, which is the difference between the overburden stress and pore pressure. Figure 4.5b shows the distribution of shear stress along the interface as the fracture approaches the strong interface. The shear stress at $x = 0$ is zero and the direction of shear stress changes as x increases. When the distance between the fracture tip and interface is 1 cm, the maximum shear stress is 2.1 MPa and the corresponding compressive stress is -9.2 MPa. The results indicate that shear failure is unlikely to occur if the friction coefficient is greater than 0.2. Thus, shear failure does not occur at the moderately strong interface, whereas shear failure occurs at the weak interface.

Figure 4.5c illustrates the distribution of the maximum principal tensile stress along the strong interface. The results show that the location of the greatest maximum principal tensile stress is coincidence with the location of peak shear stress, which is illustrated in Figure 4.5b. Flaws on either side of the parent fracture experience larger tensile stress than the flaw ahead of the fracture tip. When the greatest value of the maximum tensile stress exceeds the tensile strength of rocks, a new fracture will be initiated at the interface. As the fracture approaches the interface, the greatest value of the maximum tensile stress increases and the location of the peak is closer to $x = 0$. Take the tensile strength as 5 MPa for rocks, the offset distance x is around 6 mm if the interface is perfectly bonded. The offset distance at the strong interface is in a good agreement with Cooke and Underwood (2000)'s study, in which the offset distance at the strong interface is around 1 cm.

Figure 4.5d shows the distribution of S_{xx}, S_{yy}, and S_{xy} along the strong interface when the distance between the fracture tip and interface is 1 cm. The result indicates that the initiation of new fractures is mainly driven by the layer-parallel tensile stress. At the location of the greatest maximum principal stress, the values of S_{xx}, S_{yy}, and S_{xy} are 6, -9.2, and 2.1 MPa, respectively. Thus, the new fracture is oriented at an angle of 7.6 degrees clockwise from the vertical direction.

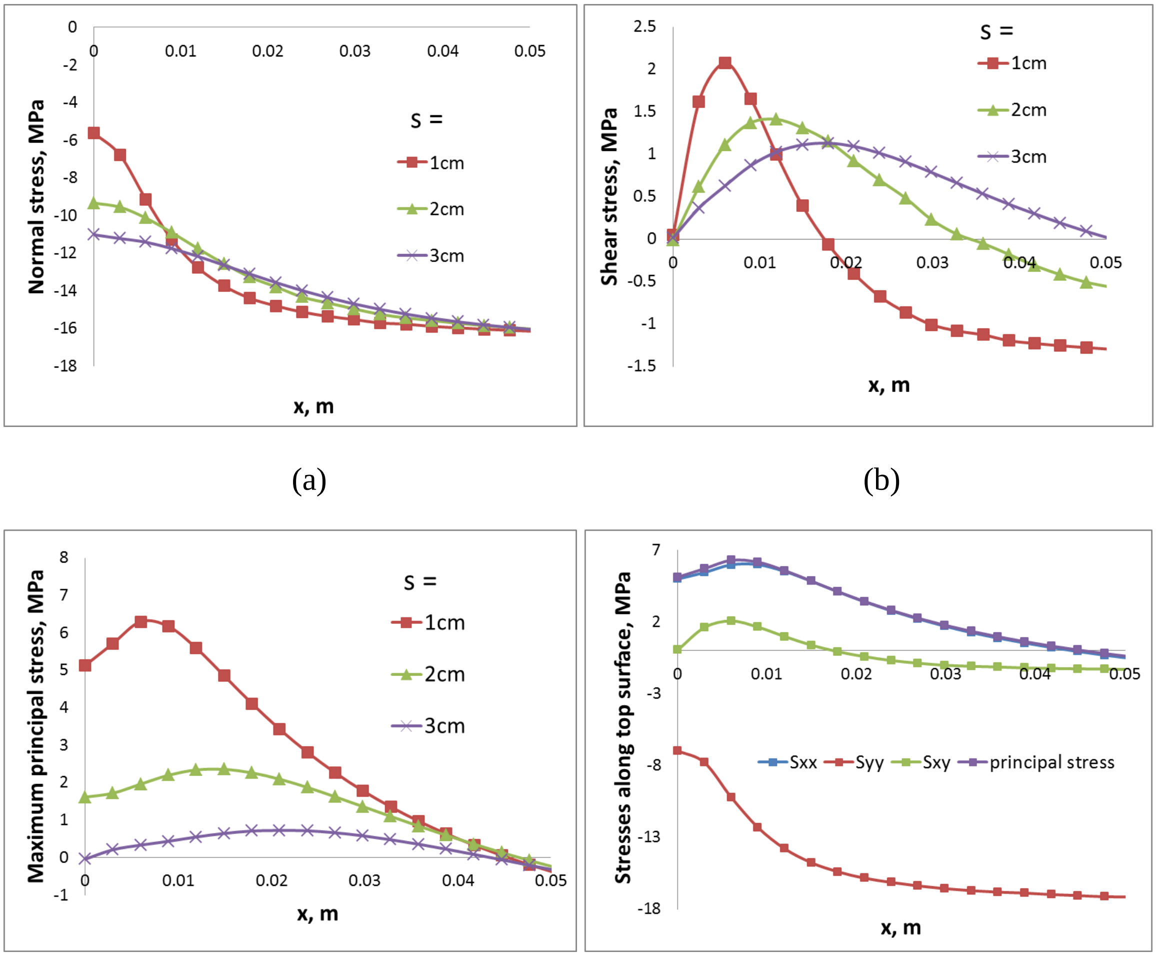

(a) (b)

(c) (d)

Figure 4.5. The distribution of (a) normal stress, (b) shear stress, and (c) the maximum principal tensile stress along the strong interface when the distance between the fracture tip and interface is1, 2, and 3 cm. (d) The distribution of various stress values (S_{xx}, S_{xy}, S_{yy}) and the maximum tensile stress along the top surface of the strong interface when the distance between the fracture tip and interface is 1 cm.

According to the stress analysis at the bonded interface under the in-situ stress condition, shear failure does not occur at the moderate-strength interface under the stress condition shown in Table 4.1. Thus, the stress state at the moderately strong interface is identical to the stress state at the bonded interface. At the in-situ stress condition where the reservoir is at the depth of two thousand meters, there is extremely high confining stress acting on the bedding plane. Thus, shear slip at the interface will be inhibited due to the friction caused by large overburden stress. It is unlikely to generate shear slip when fracture crossing or offset occurs at the interface. The only exception might be the extremely weak interface. When the distance between the fracture tip and interface is 1 cm, shear slip does not occur at the strong or moderate-strength interface, whereas shear slip occurs at the weak interface (Figure 4.6), which might yield fracture termination or larger offset at the interface.

Thus, the weak interface mechanism might be considered to be the most important factor on hydraulic fracture height containment in shallow depth where the friction at bedding planes is not sufficient to resist interface sliding (Warpinski et al. 1982; Teufel and Clark, 1984; Cooke and Underwood, 2000; Fisher and Warpinski, 2012). However, shear slip is unlikely to occur at deep reservoirs unless extremely weak interfaces are present. Thus, interface strength might not be considered as an important mechanism for fracture height containment at the in-situ condition.

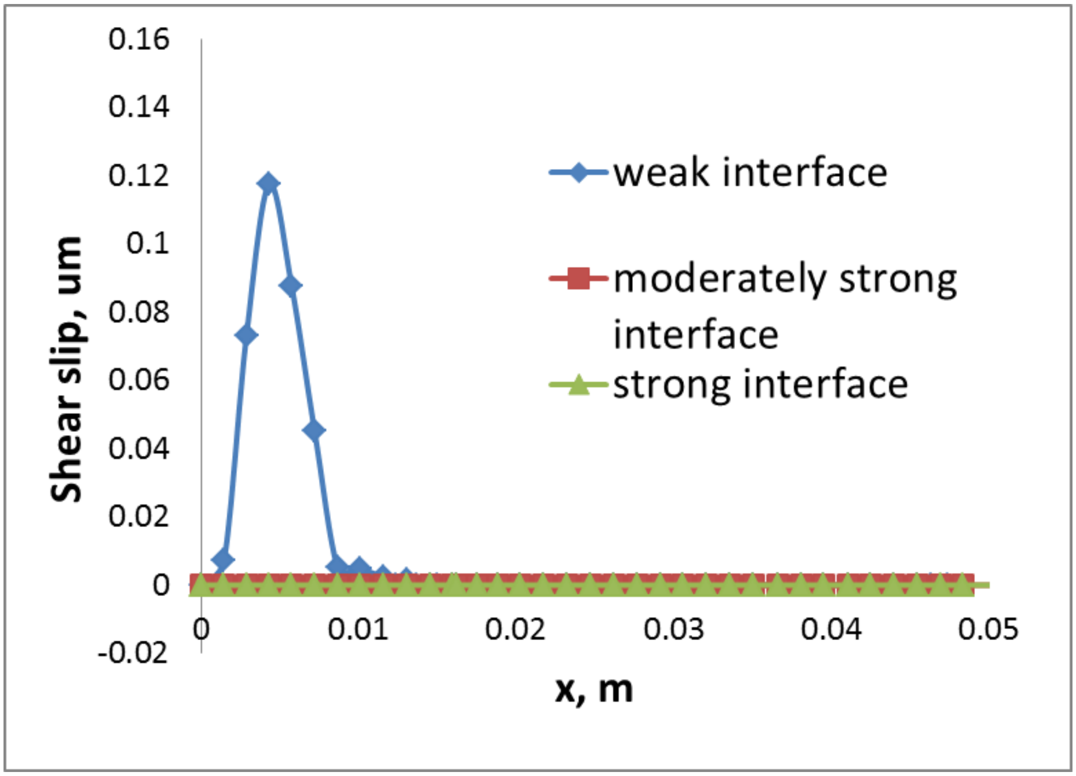

Figure 4.6. Comparison of shear slip with respect to interface strength when the distance between the fracture tip and interface is 1 cm. (The shear slip at *S* of 1 cm is investigated because fracture initiation occurs when *S* is close to 1 cm)

4.3.2 The Effect of Modulus Contrast between Layers

Differences in modulus can contribute to in-situ stress contrast between different layers. For instance, modulus contrast in Zhang and Jeffery (2008) not only affect stress concentration ahead of fracture tip but also affect the remote compressive stress acting on layers. The resulting horizontal stress contrast between adjacent layers has a strong influence on fracture crossing behavior at bedding planes (Bourne, 2003). However, as presented in section 4.2, the geostatic analysis in ABAQUS provides an effective approach to investigate the effect of modulus contrast independently while having the same horizontal stresses on the top and bottom layers. Thus, only the effect of stress concentration due to modulus contrast is investigated in this section and the effect of in-situ stress contrast will be discussed in section 4.3.3.

In the analysis, the stress state is shown in Table 4.1. The remote horizontal stresses acting on layers are the same and the interface is moderately strong. Contrast of Poisson's ratio between layers is neglected and only the modulus effect is investigated. Three cases with various modulus contrasts between adjacent layers are investigated: larger modulus in the top layer, smaller modulus in the top layer, and the homogeneous case. Results of the homogeneous modulus case have been discussed in the previous section (Figure 4.6a and b). Based on log and core data, Mullen (2010) discovered that the values of Young's Modulus vary between 6.9 and 13.8 GPa for a well drilled in the gas-condensate window of Eagle Ford play. In this study, a modulus ratio of two is utilized for the inhomogeneous case to examine the effect of modulus contrast on fracture propagation at the interface.

When the rock in the top layer is softer, the moduli of the top and bottom layers are 6.9 and 13.8 GPa, respectively. Figure 4.7a shows the distribution of shear stress along the interface, whereas Figure 4.7b shows the distribution of maximum tensile stress along the interface when the top layer is softer. As described in the previous section, the stress state at the moderately strong interface is identical to the stress state at the bonded interface. Compared to the homogeneous case (Figure 4.5b and c), the value of shear stress increases when the top layer is softer. It might be due to the fact that the softer layer is more compliant and exerts less restriction on interface deformation. However, the increased shear stress at the modulus contrast of 2 is not sufficient to induce shear slide along the moderate-strength interface at the in-situ condition. Figure 4.7b shows that the greatest value of maximum tension at the top surface decreases compared to the homogeneous case.

When rock in the top layer is stiffer, the moduli of the top and bottom layers are chosen to be 13.8 and 6.9 GPa, respectively. Figure 4.7c and d show the distribution of shear stress and the maximum tensile stress along the interface when the top layer is stiffer. Compared to the homogeneous case (Figure 4.5b and c), the value of shear stress decreases when the top layer is stiffer. It might be due to the fact that the stiffer layer yields less deformation and exerts more restriction on interface deformation. Thus, the greatest value of maximum tension increases (Figure 4.7d) and it indicates that stiffer rocks promote the initiation of a new fracture at the top layer.

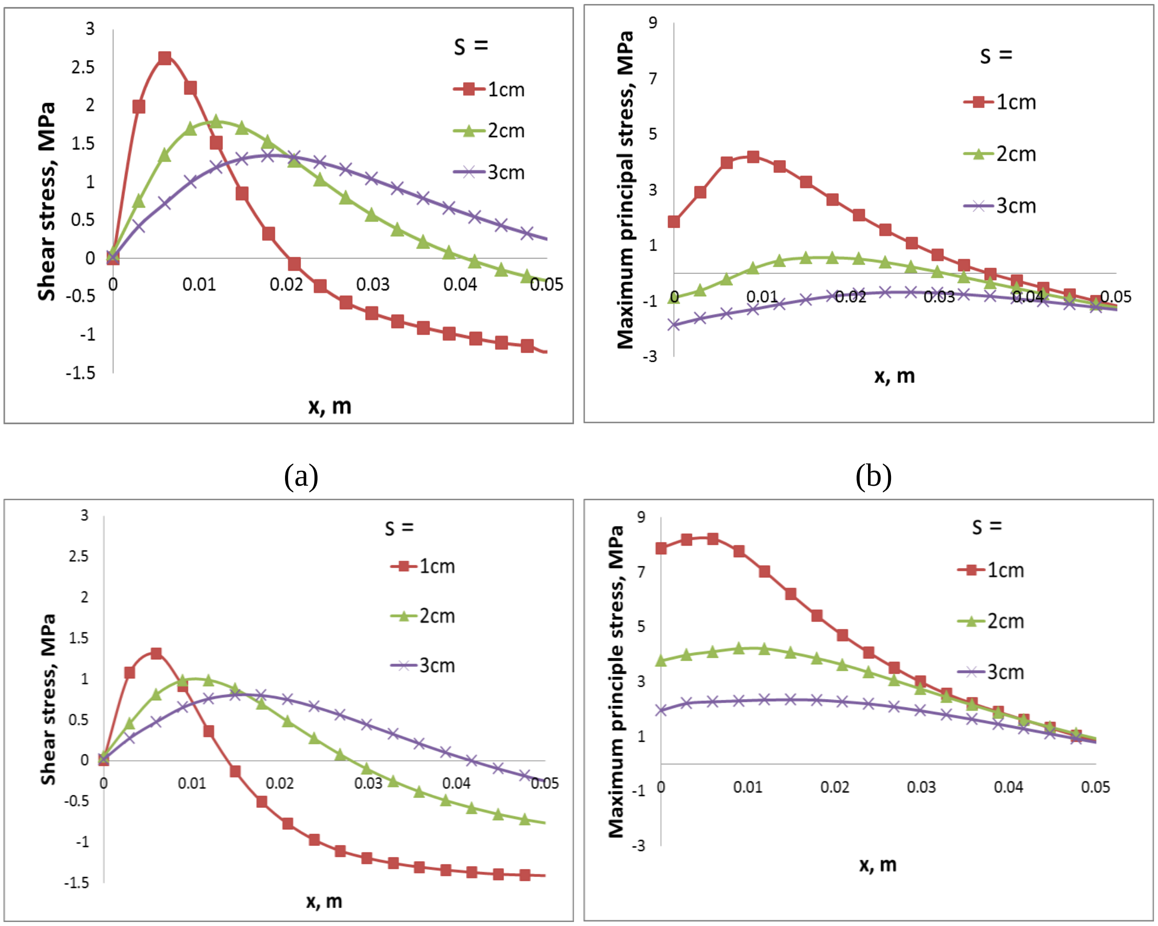

(a) (b)

(c) (d)

Figure 4.7. The distribution of (a) shear stress and (b) the maximum principal tensile stress along the moderate-strength interface as fracture tip approaches the interface when the top layer is softer. The distribution of (c) shear stress and (d) the maximum principal tensile stress along the moderate-strength interface as fracture tip approaches the interface when the top layer is stiffer.

In summary, the comparison of shear stress at various modulus contrasts indicates that soft rock in the bounding layer promotes shear sliding at the interface due to the increase of shear stress. Furthermore, Figure 4.8a illustrates the comparison of the greatest values of maximum tensile stress with respect to the distance between fracture tip and interface at various modulus contrasts between adjacent layers. The result shows that the greatest value of maximum principal stress increases when the rock in the top layer is stiffer. Taking the tensile strength of 5 MPa, a new fracture is initiated when S is equal to 1.8 cm in the case of stiff top layer, whereas a new is initiated when S is equal to 0.8 cm in the case of soft top layer. Thus, the stiff top layer promotes the initiation of a new fracture because the stiff rock enhances the stress concentration ahead of the fracture tip.

Figure 4.8b illustrates the comparison of the greatest values of maximum tensile stress with respect to the corresponding distance relative to the parent fracture as fracture tip approaches the interface. The offset distance is picked based on the tensile strength. The results indicate that the offset distances are almost the same for various modulus ratios if the tensile strength is taken as 5 MPa. Thus, modulus contrast alone does not play an important impact on fracture offset pattern at the interface under the in-situ condition.

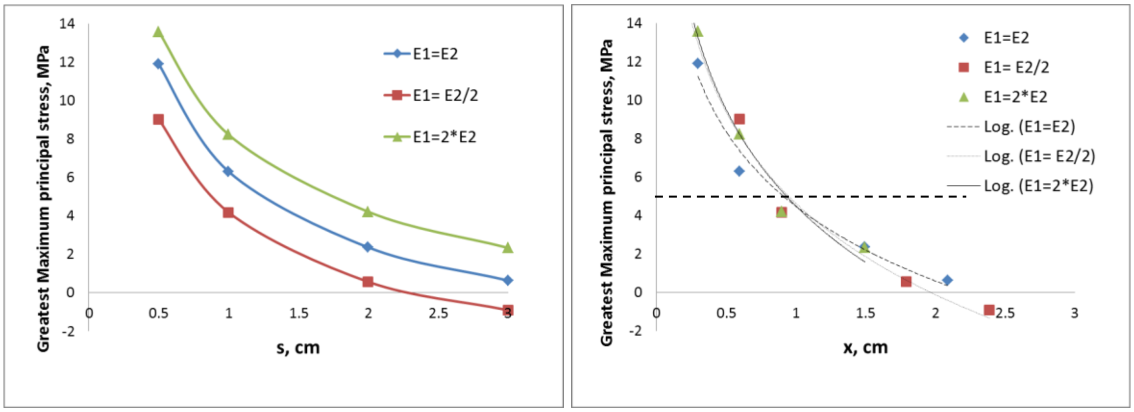

(a) (b)

Figure 4.8. Comparison of the greatest maximum principal stress with respect to (a) the distance between the fracture tip and interface, and (b) the offset distance for various modulus contrasts between adjacent layers. (E_1 is the modulus in the top layer, whereas E_2 is the modulus in the bottom layer; the dashed black curve indicates the tensile strength of 5 MPa)

4.3.3 The Effect of In-situ Stress Contrast between Layers

The effect of in-situ stress contrast between adjacent layers on fracture crossing behavior is investigated by applying different remote horizontal stresses on top and bottom layers. In this section, the modulus contrast between layers is neglected and the interface is moderately strong. The pore pressure gradient is chosen to be 0.7 psi/ft. Three cases with various in-situ stress contrasts between adjacent layers are considered: higher horizontal confining stress in the top layer, lower horizontal confining stress in the top layer, and the same confining stress. The results of the same confining stress case have been shown in the previous section (Figure 4.5b and c). In this study, the minimum horizontal stress gradient is considered 0.8 psi/ft for the low confining layer, whereas the horizontal stress gradient is considered 0.9 psi/ft for the high confining layer. Thus, the horizontal confining stresses at the low and high confining layer are 44 and 49 MPa, respectively.

The comparison between Figure 4.9a and Figure 4.9c indicates that the shear stress along the interface is not affected by the in-situ stress contrast between adjacent layers. Figure 4.9b illustrates the distribution of the maximum tensile stress as the fracture tip approaches the interface when the confining stresses at the top and bottom layers are 44 and 49 MPa, respectively. The distribution of maximum tensile stress is the same with the homogeneous case where the confining stresses at the top and bottom layers are 44 MPa. The results indicate that fracture crossing behavior at the interface is not dependent on the in-situ stress contrast between adjacent layers but the in-situ stress state at the bounding layer. Figure 4.9d illustrates the distribution of maximum tensile stress as the fracture tip approaches the interface when the confining stresses at the top and bottom layers are 49 and 44 MPa, respectively. As illustrated in Figure 4.5d, the magnitude of maximum tensile stress is mainly influenced by the layer-parallel tensile stress. Thus the value of maximum tensile stress decreases as the confining stress in the bounding layer increases.

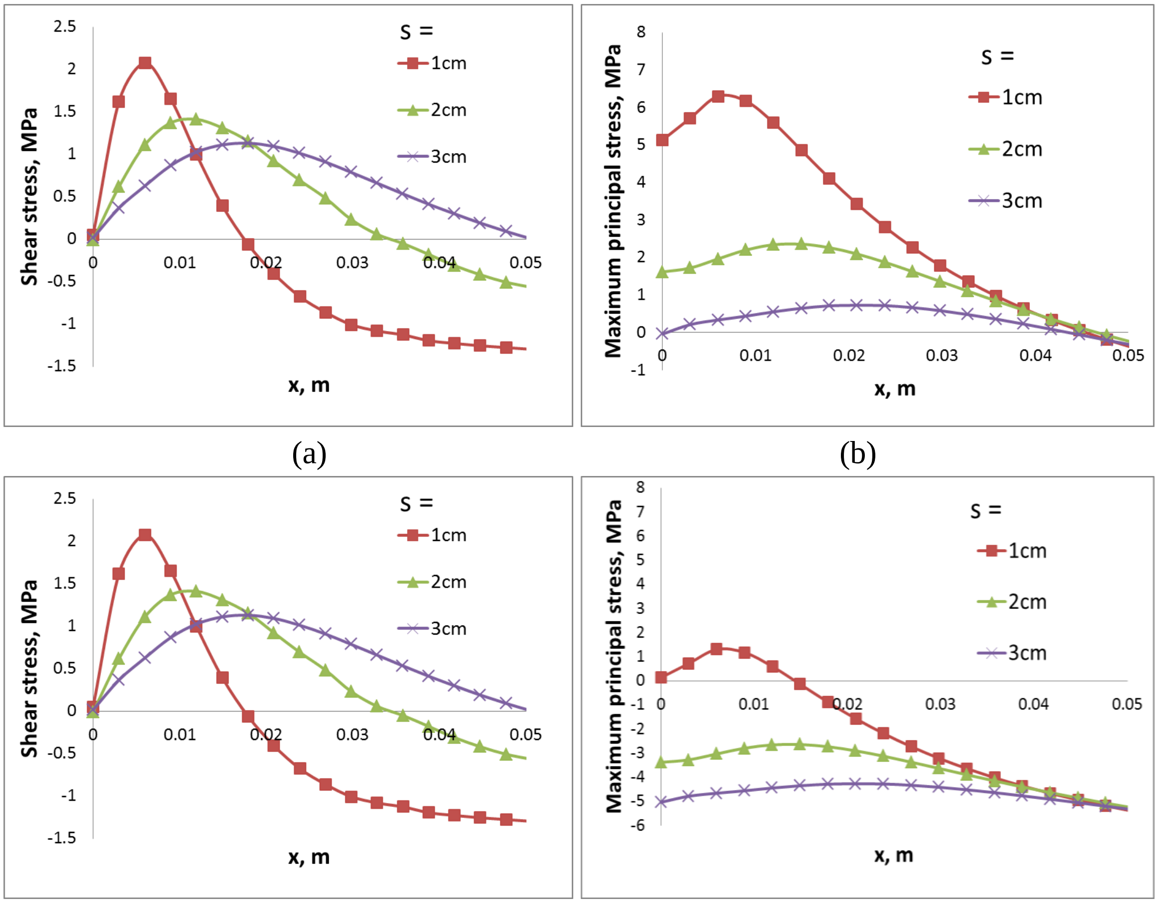

(a) (b)

(c) (d)

Figure 4.9. The distribution of (a) shear stress and (b) the maximum principal tensile stress along the interface at various distances between fracture tip and interface when the confining stresses at the top and bottom layers are 44 and 49 MPa, respectively; The distribution of (c) shear stress and (d) the maximum principal tensile stress along the interface when the confining stresses at the top and bottom layers are 49 and 44 MPa, respectively.

To summarize, Figure 4.10a shows the greatest maximum tensile stress with respect to the distance between the fracture tip and interface when the confining stresses in the top layer are 44 and 49 MPa, respectively. At the same distance between the fracture tip and interface, the greatest value of the maximum principal stress is higher when the top layer is less-pressured. Because the initiation of new fracture is based on the tensile stress criterion, larger confining stresses in the bounding layer yields smaller effective tensile stress. The results indicate that low horizontal confining stress would promote the initiation of a new fracture at the top layer. Figure 4.10b illustrates the greatest maximum tensile stress with respect to the corresponding distance relative to the parent fracture as fracture tip approaches the interface. If the tensile strength is considered 5 MPa, the offset distance is around 0.4 cm when the horizontal in-situ stress is 49 MPa, whereas the offset distance is around 0.9 cm when the horizontal in-situ stress is 44 MPa. The results indicate that the offset distance is larger when the horizontal confining stress is less in the bounding layer.

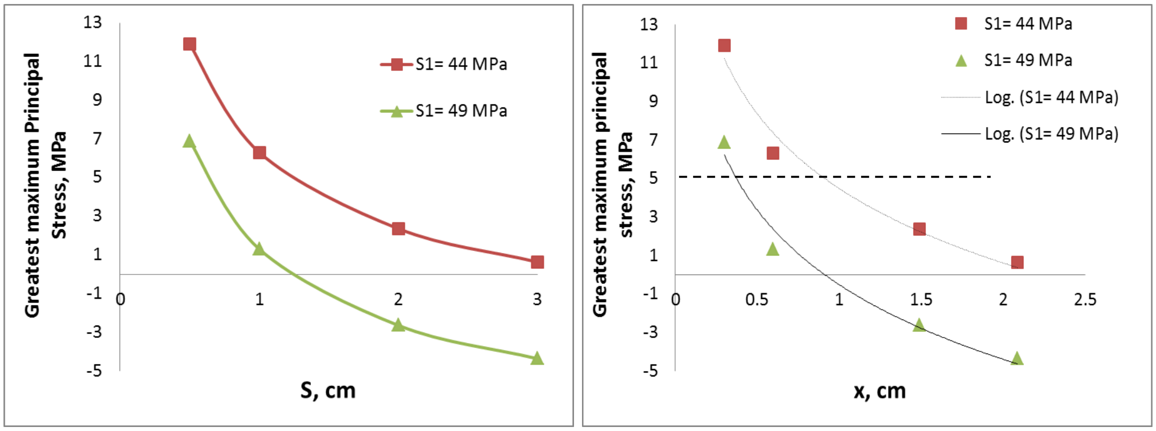

(a) (b)

Figure 4.10. Comparison of the greatest maximum tensile stress with respect to (a) the distance between fracture tip and interface and (b) the corresponding distance relative to the parent fracture. (S_1 is the in-situ horizontal stress at the top layer; the dashed black curve indicates the tensile strength of 5 MPa)

4.3.4 The Effect of Reservoir Depth

The effect of reservoir depth on fracture crossing, offset, and termination at the interface is investigated. As reservoir depth increases, pore pressure and confining stresses acting on the layers will also increase. To be consistent with our previous analysis, the stress gradients of horizontal stresses and pore pressure are 0.8 and 0.7 psi/ft, respectively, which are the same as those used in section 4.3.1. Moreover, the interface is moderately strong and there is no modulus contrast between adjacent layers. In this section, three cases with various reservoir depths are investigated and compared: 600, 1200, and 2400 meters.

The results at the reservoir depth of 2400 meters have been illustrated in Figure 4.5b and c. Figure 4.11e and f show the distribution of the maximum principal stress as the fracture tip approaches the interface when the reservoir depths are at 1200 and 600 meters, respectively. Compared to Figure 4.5b, the change of the maximum principal stresses distribution along the interface at 600 and 1200 meters is mainly due to the shear slip and debonding at the interface. There is no interface debonding or shear slip for the moderate-strong interface at the depth of 2400 meters. However, debonding (Figure 4.11b) and shear slip (Figure 4.11d) occur at *S* of 1, 2, and 3 cm when the reservoir depth is 600 meters; whereas debonding (Figure 4.11a) and shear slip (Figure 4.11c) only occurs at *S* of 1 cm when the reservoir depth is 1200 meters. When shear slip occurs, as indicated in Figure 4.11d and f, the greatest maximum principle stress occurs near the tips of the sliding segment and the local stress concentration is associated with changes in the slip magnitude at the tips of the sliding segment. The results also show that the shear slip zone decreases as the fracture tip approaches the interface, which is associated with the fact that the location of the maximum shear stress becomes closer to the parent fracture when the fracture tip approaches the interface (Figure 4.5b).

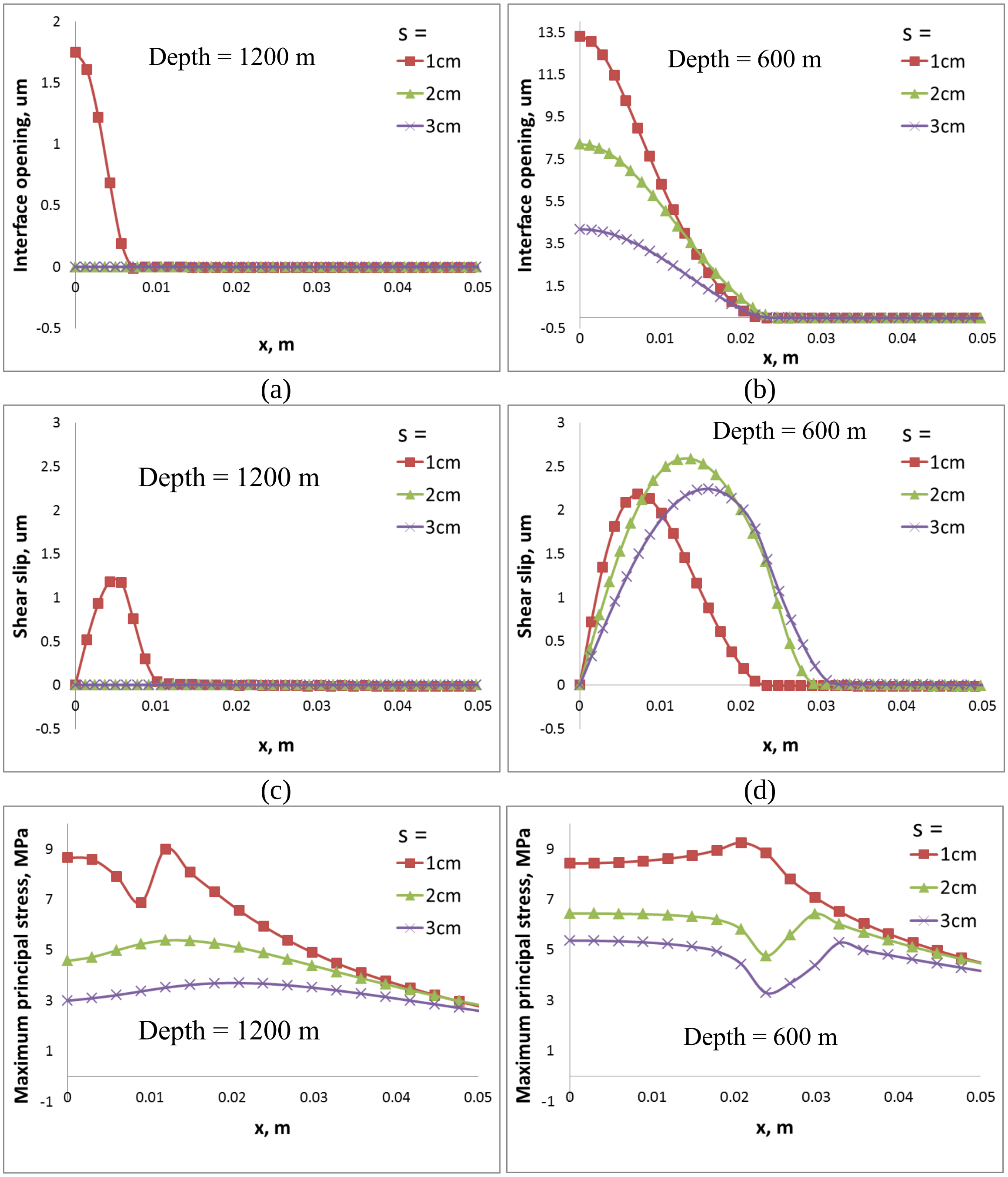

(a) (b)

(c) (d)

(e) (f)

Figure 4.11. The distribution of (a) interface opening, (c) sliding, and (e) the maximum principal stress along the interface as the fracture tip approaches the interface when the reservoir depth is 1200 meters. The distribution of (b) interface opening, (d) sliding, and (f) the maximum principal stress along the interface when the reservoir depth is 600 meters.

Figure 4.12a shows the distribution of the greatest maximum tensile stress with respect to the corresponding distance relative to the parent fracture as fracture tip approaches the interface under various overburden stresses. The results show that the offset distance is highly dependent on the reservoir depth and the value of the offset distance is larger when the reservoir depth is shallower. Taking the tensile strength of rocks as 5 MPa, the offset distance is around 1.5 cm at the depth of 1200 meters, whereas the offset distance is around 3.3 cm at the depth of 600 meters. This behavior can be attributed to shear slip under low confining stresses (Figure 4.12b). Because the overburden stress is smaller at shallower reservoir depth, it is easier for shear slip to occur. In addition, the effective confining stress at bounding layer decreases as reservoir depth decreases. Thus, it is more likely for offset to occur at shallower depth and hydraulic fracture height growth might be better inhibited. In addition, hydraulic fractures are more likely to be contained at the shallow depth due to shear slip at the interface.

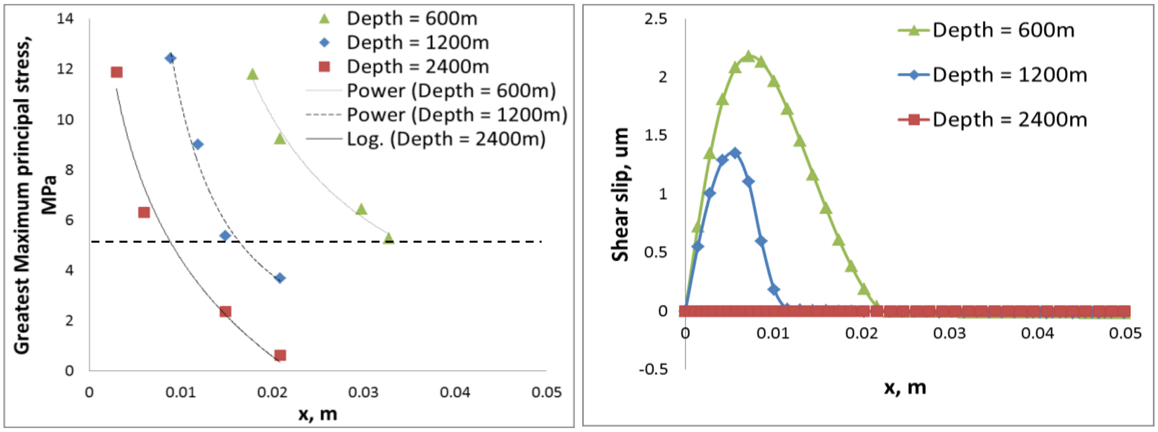

(a) (b)

Figure 4.12. (a) Comparison of the greatest maximum tensile stress with respect to the corresponding distance relative to the parent fracture as fracture tip approaches the interface under various overburden stresses; (b) Comparison of shear slip with respect to depth when the distance between the fracture tip and interface is 1 cm. (the dashed black curve indicates the tensile strength of 5 MPa)

4.3.5 The Effect of Pore Pressure

In this section, the effect of pore pressure on fracture crossing, offset or termination at the interface is investigated. Unconventional reservoir formations are usually over-pressured. In the base case, the pore pressure gradient is chosen to be 0.7 psi/ft. However, some formations such as Vaca Muerta shale reservoir are highly over-pressured and the pore pressure gradient could be over 0.8 psi/ft (Garcia et al. 2013). Thus, another case with the pore pressure gradient of 0.8 psi/ft is analyzed to investigate the effect of pore pressure on fracture crossing behavior at the interface. The overburden stress and interface strength are the same as those utilized in section 4.3.1.2. The in-situ horizontal stress is calculated based on the critically stressed fault theory. When the pore pressure gradient is 0.8 psi/ft at the depth of 2400 meters, the pore pressure and the in-situ horizontal stress are 44 and 48 MPa, respectively. Figure 4.13a and b show the distribution of shear slip and the maximum principal stress along the interface as the fracture tip approaches the interface when the pore pressure gradient is 0.8 psi/ft.

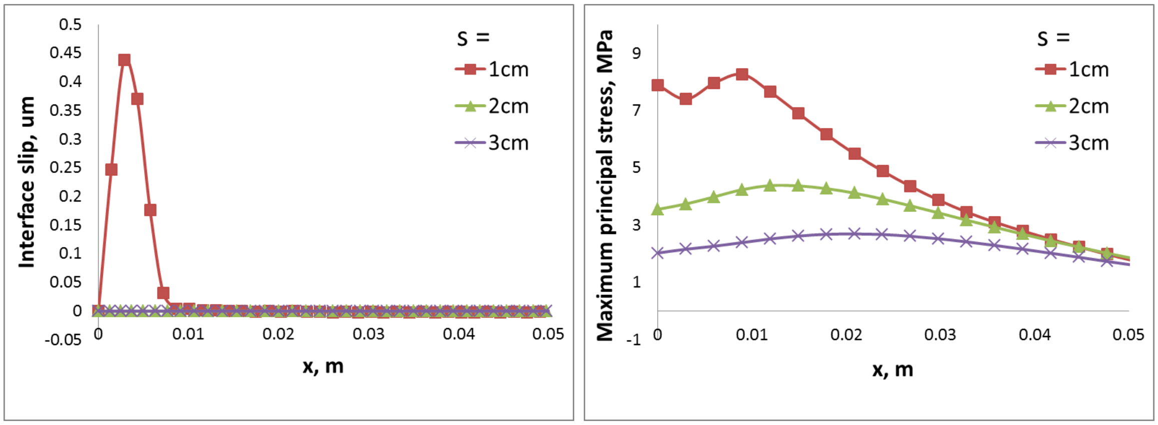

(a) (b)

Figure 4.13. The distribution of (a) shear slip and (b) the maximum principal tensile stress along the interface as the fracture tip approaches the interface when the pore pressure gradient is 0.8 psi/ft.

Figure 4.14 shows the greatest maximum tensile stress with respect to the corresponding distance relative to the parent fracture as fracture tip approaches the interface when the pore pressure gradient is 0.7 and 0.8 psi/ft, respectively. The offset distance is determined based on the tensile strength. The results show that the offset distance is highly dependent on the pore pressure gradient and a new fracture is expected to initiate at a larger offset distance when the pore pressure is larger. This behavior can be mainly attributed to shear slip at a large pore pressure gradient. When the pore pressure is larger, the effective compressive stress on the interface is smaller and thus it is easier for shear slip to occur (Figure 4.13a). Furthermore, the effective confining stress at bounding layer also decreases as pore pressure increases. Thus, when the pore pressure gradient is larger, it is more likely for offset and shear slip to occur, and thus hydraulic fracture will be better contained. As indicated in this study, the extremely high pore pressure would contribute to the existence of T-shape fracture and the extensive fracture height containment in Vaca Muerta shale reservoir (Varela and Maniere, 2016).

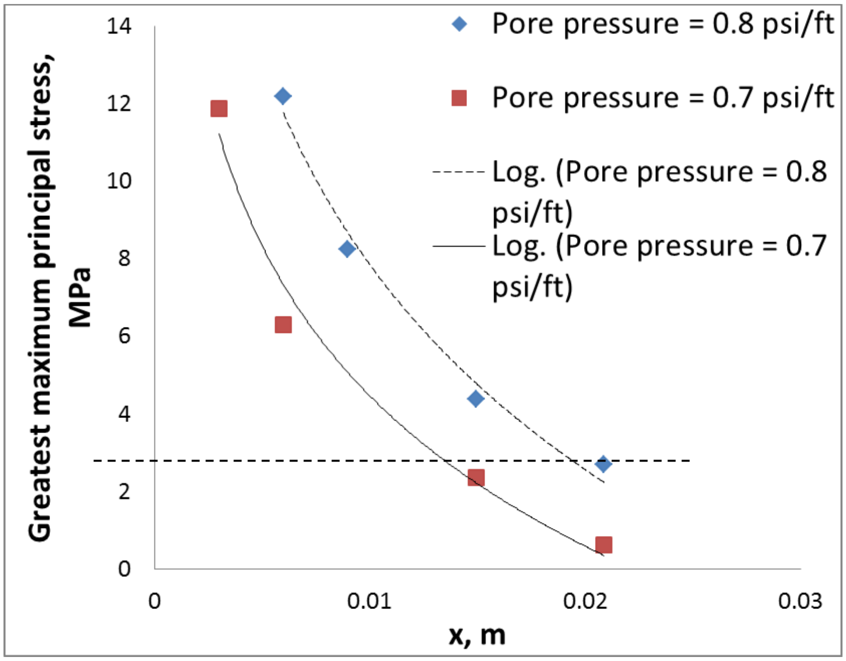

Figure 4.14. Comparison of the greatest maximum tensile stress with respect to the offset distance at various pore pressure gradients when the distance between the fracture tip and interface is 1 cm. (the dashed black curve indicates the tensile strength of 5 MPa)

4.3.6 The Effect of Fracture Toughness

In this section, the effect of fracture toughness on fracture crossing, offset, and termination at the interface is investigated. As discussed in section 2.6 in chapter 2, the apparent fracture toughness increases with fluid viscosity. Thus, the effect of fracture toughness discussed in this section would provide insight into the effect of fluid viscosity on fracture crossing behavior at the bedding plane. In this study, fracture toughness of the base model is considered 3 MPa$\sqrt{m}$. However, fracture toughness calibrated from hydraulic fracturing treatments (Shlyapobersky, 1985) is on the order of 10 MPa$\sqrt{m}$. Based on Equation 4.5, the size of process zone is on the order of 2 cm when the fracture toughness and confining stress are 10 MPa$\sqrt{m}$ and -44 MPa, respectively. Thus, in our analysis, the distance between the fracture tip and interface is greater than 2 cm in the case of large fracture toughness. Figure 4.15a illustrates the distribution of the maximum principal tensile stress along the interface as the fracture tip approaches the interface when the fracture toughness is 10 MPa$\sqrt{m}$. For comparison, the distribution of the maximum principal tensile stress at the fracture toughness of 3 MPa is shown in Figure 4.5c. When the fracture toughness is 3 MPa$\sqrt{m}$, the greatest maximum tensile stress is around 6.5 MPa when the distance between the fracture tip and interface is 1 cm. However, when the fracture toughness is 10 MPa$\sqrt{m}$, the greatest maximum tensile stress is around 7 MPa when the distance between the fracture tip and interface is 7 cm. The results indicate that larger fracture toughness promotes the initiation of a new fracture at the interface.

Figure 4.15b shows the comparison of the greatest maximum tensile stress with respect to the corresponding distance relative to the parent fracture as fracture tip approaches the interface. The results show that the offset distance is highly dependent on fracture toughness and the value of offset distance is larger when the fracture toughness is larger. This might be due to the fact that the tensile stress induced by the opening-mode fracture increases if the fracture toughness is larger. Thus, as the fracture toughness increases, fracture offset distance increases and hydraulic fracture height growth might be inhibited due to larger offset.

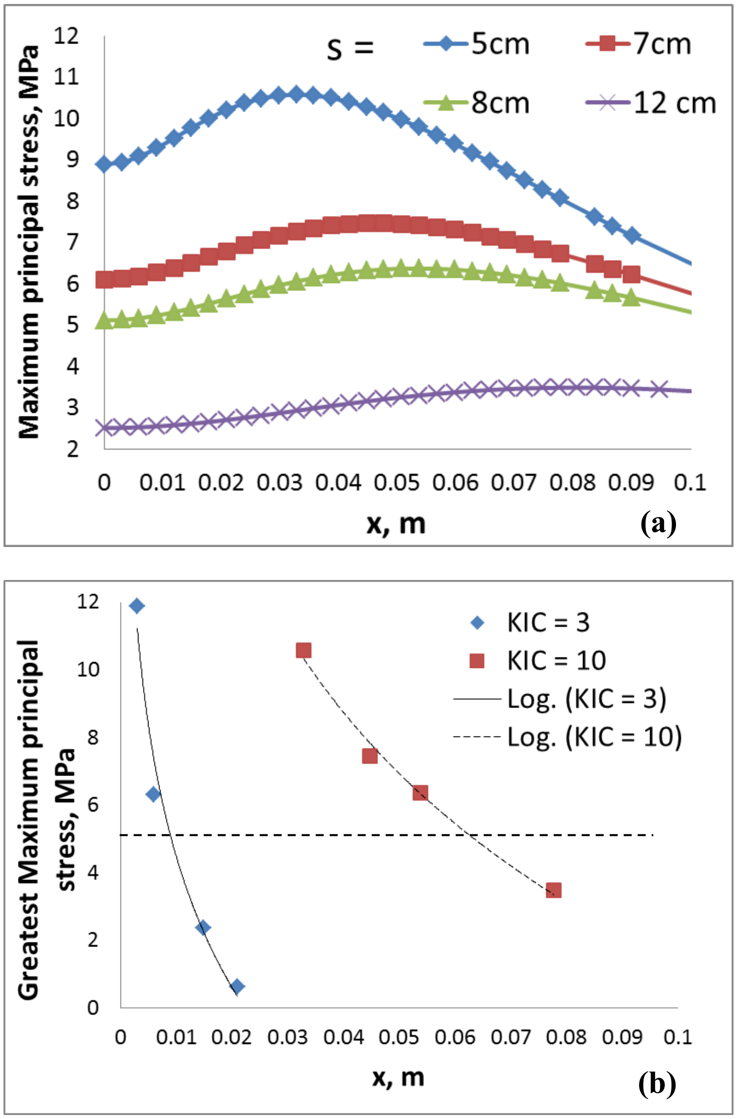

Figure 4.15. (a) The distribution of the maximum principal stress along the interface as the fracture tip approaches the interface when the fracture toughness is 10 MPa$\sqrt{m}$. (b) Comparison of the greatest maximum tensile stress with respect to the corresponding distance relative to the parent fracture at various fracture toughness. (The dashed black curve indicates the tensile strength of 5 MPa)

4.3.7 A Case Study of Eagle Ford

Unconventional reservoirs are often stratified with layers of different mechanical properties. For example, Eagle Ford shale is laminated with alternating soft shale layers and stiff limestone layers (Breyer et al. 2013). In this section, a combination of various factors on fracture height containment is investigated by considering fracture crossing behavior at the interface between shale and limestone layers. Figure 4.16a shows the model with shale layer on top, whereas Figure 4.16b shows the model with limestone layer on top. Table 4.3 shows the properties of shale and limestone layers in the model. In this study, the moduli of shale and limestone are 1 and 2 Mpsi, respectively (Mullen, 2010). The difference of Poisson's ratio between limestone and shale is neglected. The interface between limestone and shale layers is moderately strong. The reservoir depth is 2400 meters (Fisher and Warpinski, 2012) and the pore pressure gradient is about 0.7 psi/ft (Xiong et al. 2015). The in-situ horizontal stress acting on the shale layer is 49 MPa (~0.9 psi/ft), whereas the in-situ horizontal stress in the limestone layer is 44 MPa (~0.8 psi/ft). Two types of fracture toughness are utilized: 3 and 10 $\mathrm{MPa}\sqrt{\mathrm{m}}$.

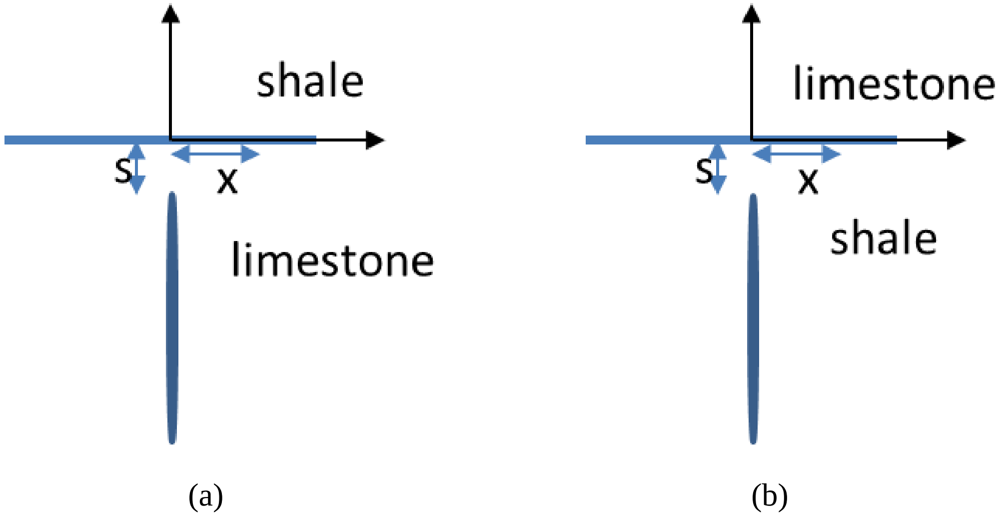

Figure 4.16. (a) A hydraulic fracture propagates towards a shale layer; (b) a hydraulic fracture propagates towards a limestone layer.

Table 4.3. Properties of shale and limestone layers

Parameters	Shale layer	Limestone layer
Shmin (MPa)	49; ~0.9 psi/ft	44; ~0.8 psi/ft
E_1, E_2 (GPa)	6.9	13.8
v_1, v_2	0.2	0.2
S_v (MPa)	55	55
Depth (meters)	2400	2400
Pore pressure (MPa)	38, ~0.7 psi/ft	
Fracture toughness (MPa$\sqrt{m}$)	3, 10	

4.3.7.1 Small Fracture Toughness

In this section, the fracture toughness is chosen to be 3 $\text{MPa}\sqrt{\text{m}}$. Figure 4.17a illustrates the distribution of the maximum principal stress along the interface as the fracture tip approaches the interface when the top layer is limestone, whereas Figure 4.17b illustrates distribution of the maximum principal stress along the interface as the fracture tip approaches the interface when the top layer is shale. Due to the effect of lower modulus and higher confining stress in the shale layer, the maximum tensile stress along the interface is smaller when the opposite layer is shale. For instance, when the distance between the fracture tip and interface is 1 cm, the greatest maximum tensile stresses are 8.22 MPa and -0.76 MPa when the top layers are limestone and shale, respectively.

Taking the tensile strength as 5 MPa for shale and limestone, a new fracture will be initiated when distances between the fracture tip and interface are around 2 and 0.5 cm when the opposite layers are limestone and shale, respectively. In order to initiate a new fracture at the shale layer, the fracture tip should be closer to the interface. Thus, a higher shear stress would occur when a new fracture is initiated if the opposite layer is shale, which might induce shear slip at the interface. As indicated in Figure 4.18, shear slip occurs when the opposite layer is shale. Due to the shear slip at the interface, fracture may be contained at the interface. As a result, larger fracture offset would occur when the opposite layer is limestone, whereas fracture may be contained due to shear slip at the interface when the opposite layer is shale.

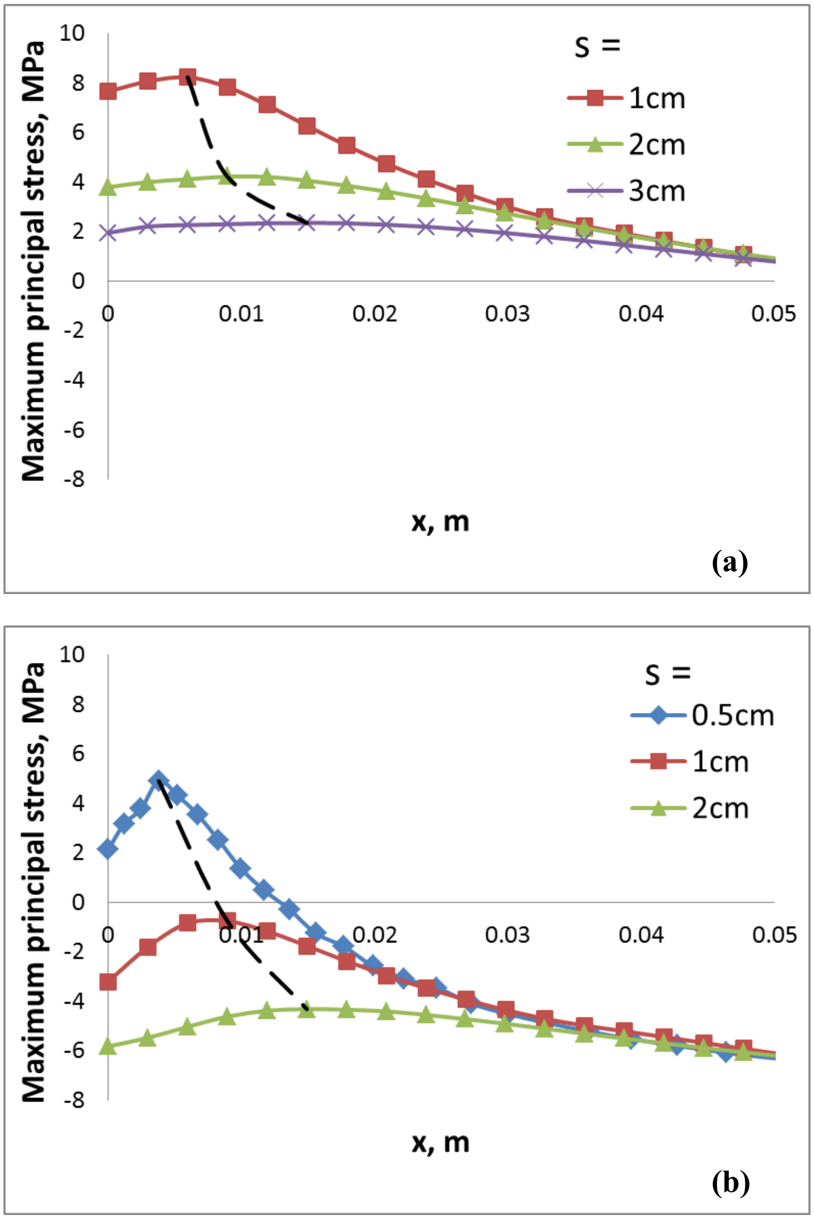

Figure 4.17. The distribution of the maximum principal stress along the interface as the fracture tip approaches (a) the limestone layer and (b) the shale layer when the fracture toughness is 3 $\mathrm{MPa}\sqrt{\mathrm{m}}$. The dashed curve shows the distribution of the greatest maximum tension as fracture tip approaches the interface.

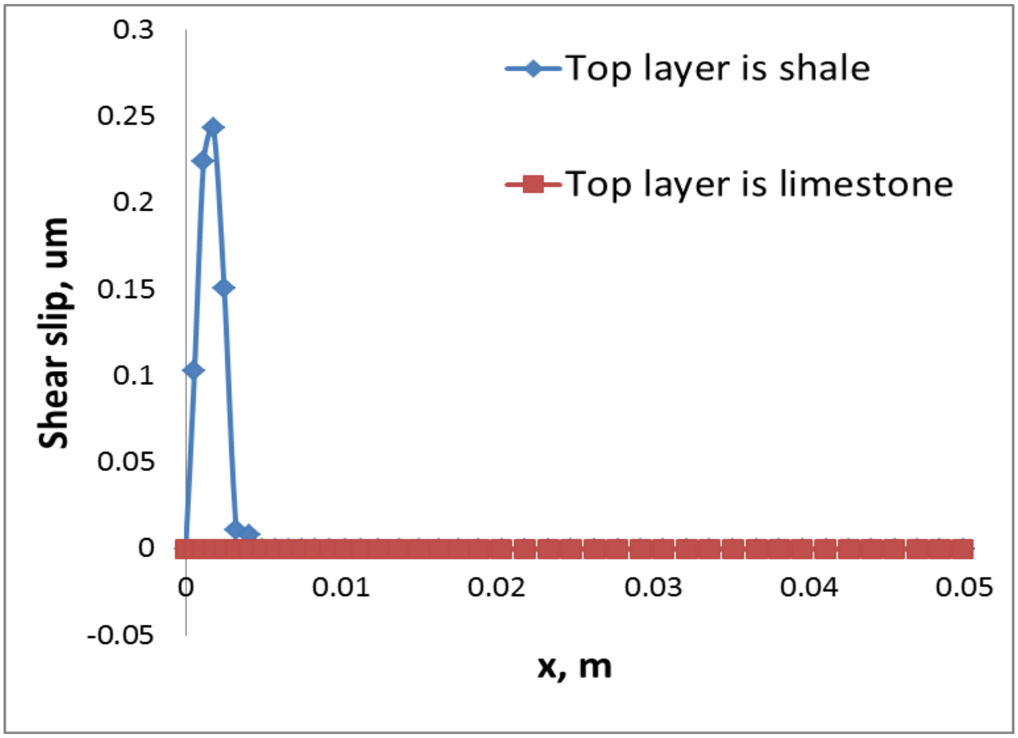

Figure 4.18. The distribution of shear slip along the interface when the greatest maximum tensile reaches rock strength (5 MPa).

4.3.7.2 Large Fracture Toughness

In this section, fracture toughness is chosen to be 10 MPa$\sqrt{\text{m}}$. Figure 4.19a illustrates the distribution of the maximum principal stress along the interface as the fracture tip approaches the interface when the opposite layer is limestone, whereas Figure 4.19b illustrates the distribution of the maximum principal stress along the interface as the fracture tip approaches the interface when the opposite layer is shale. Due to the effect of lower modulus and higher confining stress in the shale layer, the maximum tensile stress along the interface is smaller when the top layer is shale. Taking the tensile strength as 5 MPa for shale and limestone, a new fracture will be initiated when distances between the fracture tip and interface are around 15 when the opposite layer is limestone, whereas a new fracture will be initiated at the distance of 3.5 cm when the opposite layer is shale. In addition, a new fracture would be initiated with an offset distance of 6 and 2.4 cm when the top layers are limestone and shale, respectively. Compared to the cases with small fracture toughness, the results show that fracture toughness promotes fracture offset at the interface. Thus, hydraulic fracture height growth will be better contained due to larger offset as fracture toughness increases.

As indicated in Figure 4.19, fracture tip needs be closer to the interface in order to initiate a new fracture at the shale layer. Furthermore, as indicated in section 4.3.2, soft rock in the bounding layer promotes shear sliding at the interface due to the increase of shear stress. Thus, a higher shear stress would occur when a new fracture is initiated if the top layer is shale, which might induce shear slip at the interface (Figure 4. 20). Due to the shear slip at the interface, fracture may be contained at the interface.

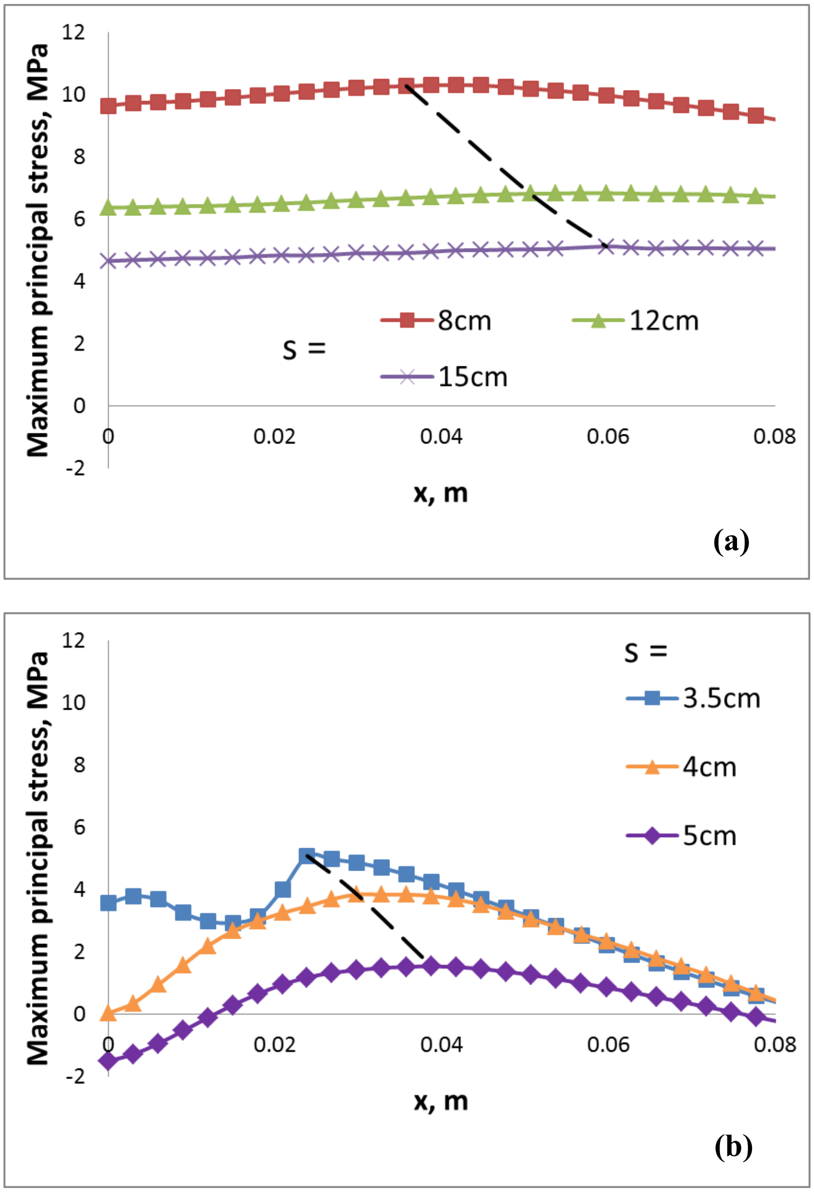

Figure 4.19. The distribution of the maximum principal stress along the interface as the fracture tip approaches (a) the limestone layer and (b) the shale layer when the fracture toughness is 10 MPa$\sqrt{\text{m}}$. The dashed curve shows the distribution of the greatest maximum tension as fracture tip approaches the interface.

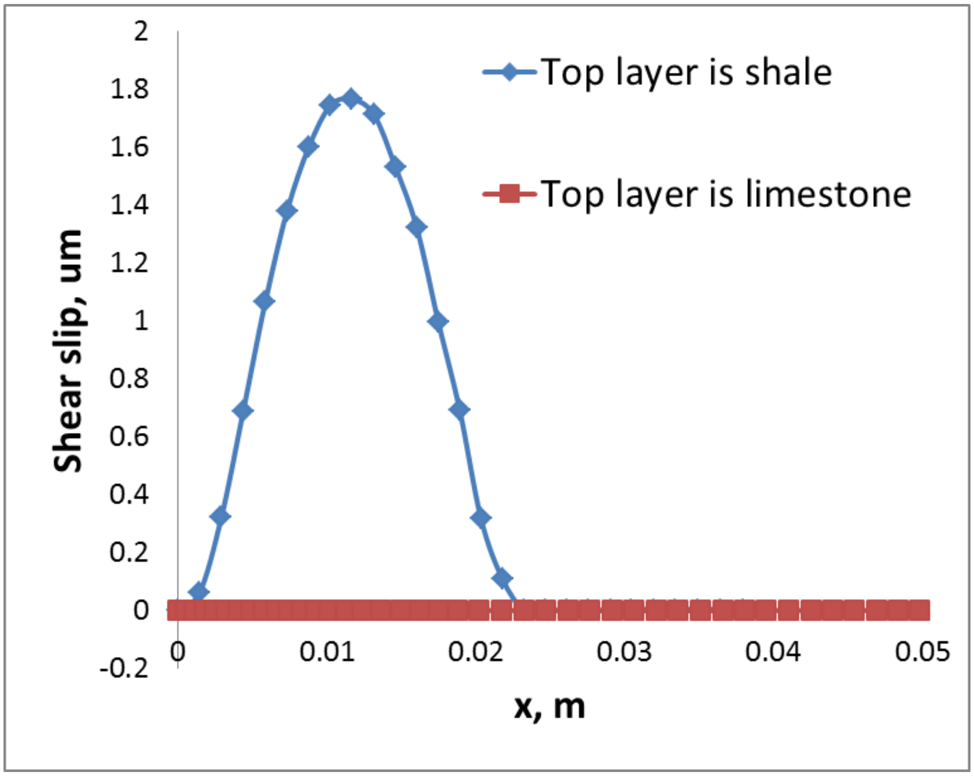

Figure 4.20. The distribution of shear slip along the interface when the greatest maximum tensile reaches rock strength (5 MPa).

In summary, the results in sections 4.3.7.1 and 4.3.7.2 show that fracture height growth might be inhibited at the interface due to shear slip when the bounding layer is softer, whereas fracture offset would be encouraged when the bounding layer is stiffer. Our conclusion is consistent with the field observations in Helgeson and Aydin (1991). By investigating a composite joint in the alternating siltstone and shale turbidite sequence of the Genesee Group of the Appalachian Plateau, they noted that joint offset is widely present at the interface when the bounding layer is shale (shale has higher Young's modulus than siltstone in this study). In addition, the observed fracture offset distances in the outcrop are on the order of a few centimeters, which is consistent with our predictions.

4.4 Discussion

This study investigated the physical mechanisms on fracture offset under the in-situ condition. However, this work did not examine fluid flow and fracture propagation once hydraulic fracture intersects the interface. Although, hydraulic fracture propagation is driven by fluid pressure and a coupled analysis of fluid flow and fracture interaction with bedding planes may be more illustrative. For instance, fluid flow through offset into the new fracture is affected by fluid viscosity (Zhang and Jeffrey, 2008). Cook and Underwood (2000) also pointed out that fluid pressures may encourage fracture termination by facilitating interface opening. However, the effect of fluid flow mainly occurs after the intersection of hydraulic fracture with the interface. According to our results and the previous analysis (Cooke and Underwood, 2000), initiation of new fractures occurs prior to the intersection between hydraulic fractures and bedding planes. Thus, fracture initiation and shear slip along bedding planes are mainly affected by the mechanical properties of layers and bedding planes.

The results presented above would provide insight into the experimental and field observations of fracture crossing behavior at bedding planes. In our analysis, limited fracture height growth can be explained by fracture offset and shear slip at the interface. The predicted fracture offset distances are on the order of a few centimeters, which are consistent with previous numerical analysis (Cooke and Underwood, 2000; Zhang and Jeffrey, 2008) and field observations (Helgeson and Aydin, 1991). Some important factors that control fracture interaction with bedding planes were investigated.

This study shows that shear sliding occurs at weak interface and it might cause fracture height containment at the interface. Our results are consistent with experimental testing (Daneshy, 1976; Teufel and Clark, 1984; ALTammar and Sharma, 2017) and numerical analysis (Cooke and Underwood, 2000; Zhang and Jeffrey, 2008). However, compared to the case of moderate-strength interface under low confining in Cook and Underwood (2000), this study shows that shear slip is unlikely to occur except for extremely weak interfaces (friction coefficient is less than 0.2) when the reservoir is buried at a depth of 2400 meters (~8000 ft). For a moderate-strength interface, shear sliding along the interface starts to occur if reservoir depth is less than 1200 meters, which is usually the shallowest depth of hydraulic fracture operations in various unconventional reservoirs (Fisher and Warpinski, 2012). Thus, shear sliding and fracture termination is unlikely to occur due to the moderate-strong interface in unconventional reservoirs.

This study also shows that initiation of new fractures at the top of interface is inhibited due to higher confining stress in the bounding layer. This result is consistent with the laboratory experimental studies and finite element analysis (Teufel and Clark, 1984). It should be noted that confining stresses in the bounding layer not only inhibit initiation of new fractures at interface, but also affect fracture propagation in layers (Simonson et al., 1978). Thus, in-situ stress contrast between adjacent layers is generally considered to be the most important factor on fracture height containment in a layered sequence (Cleary, 1980; Warpinski et al. 1982a; Warpinski et al. 1982b; Teufel and Clark, 1984; Jeffrey and Bunger, 2007).

This study also shows that small modulus contrast ($0.5 < E_1/E_2 < 2$) does not play an important role on fracture crossing behavior at the in-situ condition. Our analysis is consistent with numerical results in Ouchi (2016). He also observed that the effect of Young's modulus contrast on fracture crossing behavior is not as significant. However, our conclusions are in contrary to the experimental analysis (ALTammar and Sharma, 2017). Based on their analysis, fractures tend to cross the interface from a stiff to soft material in a straight path, whereas fractures tend to offset at the interface from a soft to stiff material. The discrepancy might be due to the difference of confining stresses. As discussed in section 4.3.4, fracture crossing behaviors are different at various reservoir depths. The effective confining stresses perpendicular to the interface in our analysis and Ouchi (2016) are on the order of 17 and 40 MPa, respectively, whereas the confining stress in ALTammar and Sharma (2017) is on the order of 0.5 MPa, which is not sufficient to prevent interface failure. For unconventional reservoirs which are buried in a depth of a few thousand meters, modulus contrast ($0.5 < E_1/E_2 < 2$) alone does not play an important role on fracture crossing behavior at the interface.

Fracture offset and shear slip at the interface is not due to a single mechanism but a bundled effect of all the mechanisms. For instance, shear slip occurs at the moderate-strength interface when the top layer is shale in the field case study (section 4.3.7), in which the coupled effect of modulus and in-situ stress contrasts between adjacent layers is investigated. However, shear slip does not occur prior to the initiation of new fractures when only the effect of the modulus contrast (section 4.3.2) or in-situ contrast (section 4.3.3) is considered. When the top layer is shale, soft modulus of the top layer increases the shear stress in the interface but reduces the layer-parallel tensile stress. Furthermore, higher horizontal confining at the soft shale inhibits new fracture initiation. Thus, in order to initiate a new fracture at the soft shale layer, fracture tip should be closer to the interface. Because these two effects play the same role in new fracture nucleation and growth, shear slip occurs when the top layer is shale. This concept illustrated in this study is similar to the "composite layer effect" in Fisher and Warpinski (2012).

4.5 Conclusions

In this study, fracture height containment in layered reservoirs is evaluated based on fracture crossing behavior at bedding planes. A two-dimensional finite element model is applied to investigate fracture crossing, offset, and termination at a bedding plane. Limited fracture height growth is explained by fracture offset and shear slip at the interface. This study shows that shear slippage and fracture termination will be encouraged by larger tensile strength of rocks in the bounding layer, higher horizontal confining stress and smaller rock stiffness in the bounding layer, weak interface strength, higher pore pressure, and lower reservoir depth. Fracture offset is encouraged by smaller tensile strength of rocks in the bounding layer, lower horizontal confining stress and high rock stiffness in the bounding layer, weak interface strength, higher pore pressure, lower reservoir depth, and larger fracture toughness. Based on the numerical results presented in this study, we observed the following:

1. For unconventional reservoirs which are usually buried in a depth of a few thousand meters, shear slip is unlikely to occur except for extremely weak interfaces. Thus, interface strength could not be considered as an important mechanism for fracture height containment at the in-situ condition.

2. At the in-situ condition of unconventional reservoirs, soft rocks in the bounding layer would enhance shear stress in the interface and reduce stress concentration at the bounding layer. However, modulus contrast ($0.5< E_1/E_2 < 2$) alone does not exert an important fact on fracture height containment at the interface.

3. The results indicate that larger layer-parallel confining stress at the bounding layer would restrict initiation of new fractures at the interface. In addition, fracture offset distance is larger when the horizontal confining stress is smaller in the bounding layer.

4. It is more likely for offset to occur at shallower depth and hydraulic fracture height growth will be inhibited. In addition, hydraulic fractures are more likely to be contained at shallow depth due to shear slip at the interface.

5. When the pore pressure is larger, the effective compressive stress on the interface is smaller and thus it is easier for shear slip to occur. In addition, fracture offset

distance is highly dependent on the pore pressure gradient and a new fracture is expected to initiate at a larger offset distance when pore pressure is larger. Thus, when the pore pressure gradient is larger, it is more likely for offset and shear slip to occur and hydraulic fracture will be better contained.

6. Fracture offset distance is highly dependent on fracture toughness and the value of offset distance is larger when the fracture toughness is larger. As the fracture toughness increases, fracture offset distance increases and hydraulic fracture height growth might be better eliminated.

7. According to the case study of Eagle Ford, stiff rock layers promote fracture offset at the interface. However, fracture might be contained at the interface due to shear slip at the interface when the top layer is soft.

CHAPTER 5: CONCLUSIONS AND RECOMMENDATIONS

5.1 Conclusions

The primary objective of this study was to investigate the physical mechanisms of hydraulic fracture height containment in layered reservoirs. This study mainly focused on examining fracture height containment due to modulus contrast between adjacent layers and quantifying the physical mechanisms on fracture offset at bedding planes under the in-situ stress condition. In addition, we verified the approach of LEFM with the apparent fracture toughness in the analysis of hydraulic fracturing.

5.1.1 LFEM with the Apparent Fracture Toughness

Following Rubin (1993)'s analysis, this study investigated the effect of confining stress and fluid lag on fracture net pressure and the apparent fracture toughness. This study also demonstrated the validity of LEFM with the apparent fracture toughness in hydraulic fracturing analysis, by comparing the near-tip stress state and fracture energy. This study could contribute to explain the discrepancy of fracture toughness between laboratory measurements and field calibration. Compared to the complicated and computationally expensive cohesive zone model, LEFM with the apparent fracture toughness provides a highly computationally efficient approach in hydraulic fracturing analysis. The following is a list of main findings.

- This study defined the apparent fracture toughness in terms of fluid lag length and in-situ confining stress, by using the Dugdale-Barenblat (DB) cohesive zone model.
- The results showed that fracture toughness is not a material constant, and instead the magnitude increases with the length of fluid lag and the magnitude of the in-situ confining stress.
- This study showed that K-dominated stress state is a good measurement of the near-tip stress state outside the fluid lag and cohesive zone of fluid-driven fractures if the apparent fracture toughness is utilized. However, LEFM with the fracture toughness measured from standard laboratory tests underestimates the near-tip stress state.
- This study also proved that fracture energy of fluid-driven fractures calculated by DB model is the same as the fracture energy based on LEFM by utilizing the apparent fracture toughness.

5.1.2 Effective Modulus of a Layered Medium

This study developed a new averaging method to evaluate the effective modulus of a layered reservoir by calibrating the fracture width profiles from the finite element analysis. Layered modulus leads to significant complication and computation cost in fracture modeling. However, the effective modulus developed in this study could preserve material balance and significantly reduces the computation cost in hydraulic fracturing simulation. The following is a list of main findings.

- The numerical results showed that the effective modulus is mainly dependent on modulus values, the height percentage of each rock layer, and fracture tip location, whereas the value of effective modulus is independent of the number of layers and layer location.
- Two novel approximations of effective modulus were developed depending on the fracture tip location, namely modified height-weighted mean (equation 3.15) and modified height-weighted harmonic average (equation 3.14).
- The sensitivity analysis showed that the modified height-weighted mean yields a good approximation of the effective modulus if the fracture tip lies in the stiff layer, whereas the modified height-weighted harmonic average is a good estimation of the effective modulus if the fracture tip lies in the soft layer.

5.1.3 Effect of Modulus Contrast on Fracture Height Growth

The effect of modulus contrast between adjacent layers was generally considered of secondary importance in terms of direct control of fracture height containment (Van Eekelen, 1982; Smith et al. 2001). For the first time, this study utilized the effective modulus to examine the effect of modulus contrast on hydraulic fracture height containment. Height containment of hydraulic fractures is the primary application of this study, but this mechanism can be applicable to height containment of any fluid-driven fractures, such as arrested veins at soft layers (Philipp et al. 2013). The following is a list of main findings.

- By examining a fluid-driven fracture propagating from a stiff layer to a soft layer, this study showed that fracture net pressure decreases due to the decreased effective modulus after the fracture tip propagates into the soft layer. Thus, the stress intensity factor decreases and hydraulic fracture height growth in the layered media will be inhibited by the soft layer.
- This study showed that fracture initiation location does not impact fracture height growth in the layered medium.

5.1.4 Fracture Offset

This study utilized a two-dimensional finite element model to investigate the physical mechanisms of fracture offset at a bedding plane under the in-situ stress state. The stress criterion from Cook and Underwood (2001) was employed to quantify the initiation of a new fracture along bedding planes. The application of this work is to understand physical mechanisms of fracture height containment due to fracture offset and provide insights for operators to design fracturing treatments and maximize the production. The following is a list of main findings.

- The results showed that the offset distance is on the order of centimeters for hydraulic fractures at the depths of thousands of meters.
- Fracture offset is encouraged by smaller tensile strength of rocks and lower horizontal confining stress in the bounding layer.

- Fracture offset and shear slip are encouraged at the weak interface. However, shear slip is unlikely to occur at a moderately strong bedding plane for hydraulic fractures at the depth of thousands of meters.
- At the in-situ stress condition, small modulus contrast ($0.5 < E_1/E_2 < 2$) between adjacent layers does not have significant impact on fracture crossing behavior at the bedding plane.
- Fracture depth and pore pressure have significant impact on fracture crossing behavior and interface failure at bedding planes. Fracture offset and shear slip are encouraged at shallower depth or over-pressured reservoirs, which would promote fracture height containment.
- Larger fracture toughness would promote the initiation of fracture and fracture offset at the bedding planes.

5.2 Recommendations

There are many interesting topics that could be extended based on the work presented in this dissertation. These topics include (1) modification of the effective modulus, (2) coupling with fluid flow, and (3) incorporating the effect of modulus contrast in the existing fracture height growth models.

One limitation of the effective moduli is that the modified heighted-weighted and harmonic moduli are dependent on fracture tip locations, which requires both fracture tips lying in the same type of layer (either stiff or soft). The current effective moduli developed in this study are not valid when two fracture tips lie in different types of layers. Future works are necessary to expand the current effective moduli, to be valid in any fracture tip location. Furthermore, this study only considers two types of layers with contrasting modulus values. This might be a good approximation of the layer properties of the transgressive-regressive cycles within the formation (Donovan and Staerker, 2010; Workman, 2013; Ferrill et al., 2014). However, observation of downhole measurements indicates that formations generally have significantly contrasting stiffness among different layers. Thus, for practical application, the effective moduli require further modification from the simplified approximation.

Hydraulic fracture propagation is a coupled process of fluid flow and rock deformation. One drawback in the analysis of fracture offset is that fluid flow is neglected, and instead a constant compressive stress is assumed to mimic fluid pressure acting on the fracture surface. However, Kresse et al. (2013) showed that fluid viscosity and pumping rate are important factors on fluid pressure, as well as hydraulic fracture crossing scenario at discontinuities. In addition, this study only simulated hydraulic fracture approaches bedding planes, neglecting fracture propagation after fracture tip reaches bedding planes. Zhang and Jeffrey (2008) showed that fluid flow through offset into the new fracture is affected by fluid viscosity. Thus, the future goal is to couple fluid flow with the existing fracture offset model to examine the effect of fluid flow on hydraulic fracture crossing behaviors at bedding planes and to simulate fracture growth from the offset location.

Understanding fracture height growth in layered reservoirs is of great importance in the success of hydraulic fracturing design. There are three main physical mechanisms related with fracture height growth, namely stress contrast between adjacent layers, modulus contrast between adjacent layers, and interface strength. As discussed in other studies (Teufel and Clark, 1984; Fisher and Warpinski, 2012) and this project, the effect of interface failure is only dominant in shallow or over-pressured reservoirs. In the existing fracture height growth models (Simonson et al. 1978; Fung, et al. 1987; Economides and Nolte, 2000; Liu and Valko, 2015), stress contrast is considered to the dominant factor and the effect of modulus contrast on fracture height growth is generally neglected (Van Eekelen, 1982; Smith et al. 2001). However, this study showed that the effect of modulus contrast can be significant, by affecting fracture net pressure. Future work could develop a new fracture height growth model to couple the effect of stress and modulus contrast.

References

Abbas, S., E. Gordeliy, A. Peirce, B. Lecampion, D. Chuprakov, and R. Prioul. 2014. Limited Height Growth and Reduced Opening of Hydraulic Fractures due to Fracture Offsets: an XFEM Application. In *Proceedings of the SPE Hydraulic Fracturing Technology Conference, Woodlands, Texas, 4–6 February*, SPE 168622.

Al-Shayea, N.A., K. Khan, and S.N. Abduljauwad. 2000. Effects of Confining Pressure and Temperature on Mixed-Mode (I–II) Fracture Toughness of a Limestone Rock. *International Journal of Rock Mechanics and Mining Sciences* 37, 4: 629–643.

AI Tammar, M., and M.M. Sharma. 2017. Effect of Geological Layer Properties on Hydraulic Fracture Initiation and Propagation: An Experimental Study. In *Proceedings of the SPE Hydraulic Fracturing Technology Conference, Woodlands, Texas, 24–28 January,* SPE 184871.

Barenblatt, G.I. 1962. The Mathematical Theory of Equilibrium Cracks in Brittle Fracture. *Advances in Applied Mechanics*, 7:55–129.

Barree, R.D. 1983. A Practical Numerical Simulator for Three-dimensional Fracture Propagation in Heterogeneous Media. In *Proceedings of the SPE Symposium on Reservoir Simulation*, *San Francisco, CA, 15–18 November*, SPE 12273.

Barree, R.D., and P.H. Winterfeld. 1998. Effects of Shear Planes and Interfacial Slippage on Fracture Growth and Treating Pressures. In *Proceedings of the SPE 73rd Annual Technical Conference and Exhibition*, *New Orleans, Louisiana. 27-30 September,* SPE 48926.

Bastola, S. and Y.P. Chugh. 2015. Shear Strength and Stiffness Properties of Bedding Planes and Discontinuities in the Immediate Roof Rocks Overlying the No 6 Coal Seam in Illinois. In *Proceedings of 13th International Congress of Rock Mechanics, Montreal, Canada, 10–13 May*.

Bourne, S.J. 2003. Contrast of Elastic Properties between Rock Layers as a Mechanism for the Initiation and Orientation of Tensile Failure under Uniform Remote Compression, *Journal of Geophysical Research*, 108, B8: 2395.

Boussinesq, M. J. 1885. Application des potentiels a l'etude de l'equilibre et du mouvement des solides elastiques, principalement au calcul des deformations et des pressions que produisent, dans ces solides, des efforts quelconques exerces sur une petite partie de leur surface ou de leur interieur: Memoire suivi de notes etendues sur divers points de physique mathematique et d'analyse, *GauthierVillars, Paris*: 722.

Breyer, J.A., R.A. Denne, J. Funk, T. Kosanke, and J. Spaw. 2013. Stratigraphy and Sedimentary Facies of the Eagle Ford Shale (Cretaceous) between the Maverick Basin and the San Marcos Arch, Texas, USA. *In Proceedings of AAPG Annual Convention and Exhibition, Pittsburgh, Pennsylvania, 19-22 May.*

Breyer, J. A., R. A. Denne, T. Kosanke, J. M. Spaw, J. Funk, P. Christianson, D. A. Bush, and R. A. Nelson. 2016. Facies, Fractures, Pressure, and Production in the Eagle Ford Shale (Cretaceous) between the San Marcos Arch and the Maverick Basin, Texas, U.S.A., *The Eagle Ford Shale: A renaissance in U.S. oil production: AAPG Memoir* 110: 363–384.

Bunger, A.P., E. Detournay, and R.G. Jeffrey. 2005. Crack Tip Behavior in near-Surface Fluid-Driven Fracture Experiments. *Comptes Rendus Mecanique* 333: 299–304.

Chen, Z. 2012. Finite Element Modelling of Viscosity Dominated Hydraulic Fractures. *Journal of Petroleum Science and Engineering*, 88, 89: 136–44.

Chen, Z., A. P. Bunger, X. Zhang, and R.G. Jeffrey. 2009. Cohesive Zone Finite Element-Based Modeling of Hydraulic Fractures. *Acta Mechanica Solida Sinica* 22, 5: 443–52.

Chuprakov, D. 2015. Hydraulic Fracture Height Growth Limited by Interfacial Leakoff. *Hydraulic Fracturing Journal* 2, 4: 21-35.

Chuprakov, D., O. Melchaeva, and R. Prioul. 2014. Injection-sensitive Mechanics of Hydraulic Fracture Interaction with Discontinuities. *Rock Mech Rock Eng* 47:1625-1640.

Chuprakov, D., and R. Prioul. 2015. Hydraulic Fracture Height Containment by Weak Horizontal Interface. In *Proceedings of the SPE Hydraulic Fracturing Technology Conference, Woodlands, Texas, 3–5 February,* SPE 173337.

Cleary, M.P. 1980. Analysis of Mechanisms and Procedures for Producing Favorable Shapes of Hydraulic Fractures. In *Proceedings of SPE Annual Technical Conference and Exhibition, Dallas, Texas, 21–24 September*, SPE 9260.

Clifton, R.J. and J.J. Wang. 1988. Multiple Fluids, Proppant Transport, and Thermal Effects in Three-dimensional Simulation of Hydraulic Fracturing. In *Proceedings of SPE Annual Technical Conference and Exhibition, Houston, Texas, 2–5 October,* SPE 18198.

Comer, J. B. 1991. Stratigraphic analysis of the Upper Devonian Woodford formation, Permian basin, west Texas and New Mexico. *University of Texas at Austin, Bureau of Economic Geology, Report of Investigations* 201.

Cooke, M., and C. Underwood., 2001. Fracture Termination and Offset at Bedding Interfaces due to Frictional Slip and Interface Opening. *Journal of Structural Geology* 23, 2: 223–238.

Curry, M., T. Maloney, R. Woodruff, and R. Leonard. 2010. Less Sand May Not be Enough. In *Proceedings of the SPE Unconventional Gas Conference, Pittsburgh, Pennsylvania, USA, 23–25 February*, SPE 131783.

Dahi-Taleghani, A., and J.E. Olson. 2011. Numerical Modeling of Multi-stranded Hydraulic Fracture Propagation: Accounting for the Interaction between Induced and Natural Fractures. *SPE Journal* 16, 3: 575–581.

Daneshy, A.A., 1976. Hydraulic Fracture Propagation in Layered Formations. In *Proceedings of the SPE-AIME 51st Annual Fall Technical Conference and Exhibition. New Orleans. 3-6 October,* SPE 6088

Daneshy, A. A. 1978. Hydraulic Fracture Propagation in Layered Formations. *SPE Journal* 18, 1: 33–41.

Daneshy, A.A., 2003. Off-balance Growth: a New Concept in Hydraulic Fracturing. *Journal of Petroleum Technology,* 78:78-85.

Daneshy, A.A. 2009. Factors Controlling the Vertical Growth of Hydraulic Fractures. In *Proceedings of the 2009 SPE Hydraulic Fracturing Technology Conference*. *Woodlands, Texas. 19-21 January,* SPE 118789.

Dassault Systèmes. 2013. ABAQUS 6.13 documentation.

Delaney, P.T., and D.D. Pollard. 1981. Deformation of Host Rocks and Flow of Magma during Growth of Minette Dikes and Breccia-Bearing Intrusions near Ship Rock, New Mexico. *USGS Numbered Series. Professional Paper. U.S. G.P.O*.

De Peter, J. Cornelis, and Y. Dong. 2009. Fracture Containment in Soft Sands by Permeability or Stress Contrast. In *Proceedings of the 2009 SPE Hydraulic Fracturing Technology Conference*. *Woodlands, Texas. 19-21 January*, SPE 119634.

Detournay, E., and D. I. Garagash. 2003. The Near-Tip Region of a Fluid-Driven Fracture Propagating in a Permeable Elastic Solid. *Journal of Fluid Mechanics* 494: 1–32.

Detournay, E. 2016. Mechanics of Hydraulic Fractures. *Annual Review of Fluid Mechanics* 48, 1: 311–39.

Donovan, A. D., and T. S. Staerker. 2010. Sequence Stratigraphy of the Eagle Ford (Boquillas) Formation in the Subsurface of South Texas and Outcrops of West Texas. *Gulf Coast Association of Geological Societies Transactions*, 60: 861-899.

Dugdale, D.S. 1960. Yielding of Steel Sheets Containing Slits. *Journal of the Mechanics and Physics of Solids* 8, 2: 100–104.

Economides, M.J. and K.G. Nolte. 2000. Reservoir Stimulation. Chichester, England; New York, Wiley.

Ferrill, D.A., R.N. McGinnis, A.P. Morris, and M.A. Evans. 2014. Control of Mechanical Stratigraphy on Bed Restricted Jointing and Normal Faulting: Eagle Ford Formation, South Central Texas. *AAPG Bulletin* 98, 11: 2477–2506.

Fisher, K., and N. Warpinski. 2012. Hydraulic Fracture Height Growth: Real Data. In *Proceedings of the SPE Annual Technical Conference and Exhibition, Denver, 30 October–2 November,* SPE 145949.

Fung, R.L., S. Vilayakumar, and D.E. Cormack. 1987. Calculation of Vertical Fracture Containment in Layered Formations. *SPE Formation Evaluation* 2, 4: 518-522.

FracproPT, 2007. Mannual for FracproPT.

Garagash, D., and E. Detournay. 1999. The Tip Region of a Fluid-Driven Fracture in an Elastic Medium. *Journal of Applied Mechanics* 67, 1: 183–92.

Garagash, D. 2006. Propagation of a Plane-Strain Hydraulic Fracture with a Fluid Lag: Early-Time Solution. *International Journal of Solids and Structures* 43, 18–19: 5811–5835.

Garcia, M.N., F. Sorenson, J.C. Bonapace, F. Motta, C. Bajuk, and H. Stockman. 2013. Vaca Muerta Shale Reservoir Characterization and Description: The Starting Point for Development of a Shale Play with Very Good Possibilities for a Successful Project. In *Proceedings of the Unconventional Resources Technology Conference, Denver, Colorado, 12–14 August*, SPE 1508336.

Garcia, X., N. Nagel, F. Zhang, M. Sanchez-Nagel, and B. Lee. 2013. Revisiting Vertical Hydraulic Fracture Propagation through Layered Formations - A Numerical Evaluation. In *Proceedings of the 47th US Rock Mechanics / Geomechanics Symposium. San Francisco, 23-26 June*, ARMA 13-203.

Griffith, A.A. 1921. The Phenomena of Rupture and Flow in Solids. *Philosophical Transactions of the Royal Society of London Series A* 221: 163–198.

Groenenboom, J., and D.V. Dam. 2000. Monitoring Hydraulic Fracture Growth: Laboratory Experiments. *GEOPHYSICS* 65, 2: 603–11.

Gu, H., and E. Siebrits. 2008. Effect of Formation Modulus Contrast on Hydraulic Fracture Height Containment. *SPE Production and Operations* 23, 2: 170–176.

Gu, H., E. Siebrits, and A. Sabourov. 2008. Hydraulic Fracture Modeling with Bedding Plane Interfacial Slip. In *Proceedings of the 2008 SPE Eastern Regional/AAPG Eastern Section Joint Meeting, Pittsburgh, Pennsylvania, 11-15 October*, SPE 117445.

Gu, H., and X. Weng. 2010. Criterion for Fractures Crossing Frictional Interfaces at Non-orthogonal Angles. In *Proceedings of Rock Mechanics Symposium and 5th U.S. Canadian Rock mechanics Symposium. Salt Lake City, UT, June 27–30*, ARMA 10-198.

Guo, H., N. I. Aziz, and L. C. Schmidt. 1993. Rock Fracture-Toughness Determination by the Brazilian Test. *Engineering Geology* 33, 3: 177–88.

Hanson, M.E., R.J. Shaffer, and G.D. Anderson. 1981. Effects of Various Parameters on Hydraulic Fracturing Geometry. *SPE Journal* 21, 4: 435–441.

He, M., and J. Hutchinson. 1989. Crack Deflection at an Interface between Dissimilar Elastic Materials. *International Journal of Solids and Structures*. 25, 9: 1053-1067.

Helgeson, D.E. and A. Aydin. 1991. Characteristics of Joint Propagation across Layer Interfaces in Sedimentary Rocks. *Journal of Structural Geology*, 13, 8: 897–911.

Hunsweck, M.J., Y. Shen, and A.J. Lew. 2013. A Finite Element Approach to the Simulation of Hydraulic Fractures with Lag. *International Journal for Numerical and Analytical Methods in Geomechanics* 37, 9: 993–1015.

Irwin, G.R. 1948. Fracture Dynamics. *Fracturing of Metals, pp. 147-166. American Society for Metals, Cleveland.*

Irwin, G.R. 1957. Analysis of Stresses and Strains near the End of a Crack Traversing a Plate, *Journal of Applied Mechanics* 24: 361-364.

Jaeger, J.C., and N.G.W. Cook. 1979. Fundamental of Rock Mechanics, 3rd edition. *Chapman and Hall, New York.*

Jeffrey, R. G. 1989. The Combined Effect of Fluid Lag and Fracture Toughness on Hydraulic Fracture Propagation. *In Proceedings of Low Permeability Reservoirs Symposium, Denver, Colorado, 6-8 March.*

Jeffrey, R.G. Jr, R.P. Brynes, P.J. Lynch, and D.J. Ling. 1992. An Analysis of Hydraulic Fracture and Mineback Data for a Treatment in the German Creek Coal Seam. In *Proceedings of SPE Rocky Mountain Regional Meeting, Casper, Wyoming, 18–21 May*, SPE 24362.

Jeffrey, R.G., and A. Bunger. 2007. A Detailed Comparison of Experimental and Numerical Data on Hydraulic Fracture Height Growth through Stress Contrasts. In *Proceedings of the SPE Hydraulic Fracturing Technology Conference, College Station, Texas, 29–31 January,* SPE 106030.

Jeffrey, R.G., X. Zhang, and M.J. Thiercelin. 2009. Hydraulic Fracture Offsetting in Naturally Fractured Reservoirs: Quantifying a Long-Recognized Process. In *Proceedings of the SPE Hydraulic Fracturing Technology Conference. Woodlands, Texas. 19-21 January,* SPE 119351.

Jing, L., 2003. A Review of Techniques, Advances and Outstanding Issues in Numerical Modelling for Rock Mechanics and Rock Engineering. *International Journal of Rock Mechanics and Mining Sciences* 40, 3: 283–353.

Johnson, E., and M.P. Cleary. 1991. Implications of Recent Laboratory Experimental Results for Hydraulic Fractures. *In Proceedings of Low Permeability Reservoirs Symposium, Denver, Colorado, 15-17 April.*

Johnston, J. E., and N. I. Christensen, 1995, Seismic Anisotropy of Shales. *Journal of Geophysical Research*, 100: 5991–6003

Jones, R.M. 1975. Mechanics of Composite Materials, New York: *Hemisphere Publishing Corporation*.

King, G.E. 2012. Hydraulic Fracturing 101: What Every Representative, Environmentalist, Regulator, Reporter, Investor, University Researcher, Neighbor and Engineer Should Know About Estimating Frac Risk and Improving Frac Performance in Unconventional Gas and Oil Wells. In *Proceedings of the SPE Hydraulic Fracturing Technology Conference. Woodlands, Texas. 6-8 February*, SPE 152596.

Khazan, Y.M., and Y.A. Fialko. 1995. Fracture Criteria at the Tip of Fluid-Driven Cracks in the Earth. *Geophysical Research Letters* 22, 18: 2541–44.

Kresse, O., X. Weng, D. Chuprakov, R. Prioul, and C. Cohen. 2013. Effect of Flow Rate and Viscosity on Complex Fracture Development in UFM Model. In *Proceeding of the ISRM International Conference for Effective and Sustainable Hydraulic Fracturing. Brisbane, Australia. 20-22 May,* ISRM-ICHF-2013-027.

Labuz, J. F., S. P. Shah, and C. H. Dowding. 1985. Experimental Analysis of Crack Propagation in Granite. *International Journal of Rock Mechanics and Mining Sciences & Geomechanics Abstracts* 22, 2: 85–98.

Lawn, B. 1998. Fracture of Brittle Solids. 2nd ed., Cambridge University Press, New York.

Lee, H.P. 2016. Fracture Propagation in Naturally Fractured Reservoirs, Ph.D. Thesis, The University of Texas at Austin, Austin, TX.

Lee, J.C. and L.M. Keer. 1986. Study of a Three-dimensional Crack Terminating at an Tnterface. *Journal of Applied Mechanics* 53, 2: 311–316.

Lister, J.R. 1990. Buoyancy-Driven Fluid Fracture: The Effects of Material Toughness and of Low-Viscosity Precursors. *Journal of Fluid Mechanics* 210: 263–80.

Liu, S. and P.P. Valko. 2015. An Improved Equilibrium Height Model for Predicting Hydraulic Fracture Height Migration in Multilayer Formations. In *Proceedings of the SPE Hydraulic Fracturing Technology Conference*. *Woodlands, Texas. 3-5 February*, SPE 173335.

Martin, R., J. D. Baihly, R. Malpani, G. Lindsay. W.K. Atwood. 2011. Understanding Production from Eagle Ford-Austin Chalk System. In *Proceedings of SPE Annual Technical Conference and Exhibition, Denver, Colorado, USA, 30 October–2 November*, SPE 145117.

McClure, M.W. and R.N. Horne. 2013. Discrete Fracture Network Modeling of Hydraulic Stimulation: Coupling Flow and Geomechanics, *Springer Briefs in Earch Sciences*, *Springer*.

Medlin, W. L., and L. Masse. 1984. Laboratory Experiments in Fracture Propagation. *Society of Petroleum Engineers Journal* 24, 3: 256–68

Mullen, J. 2010. Petrophysical Characterization of the Eagle Ford Shale in South Texas. In *Proceedings of Canadian Unconventional Resources and International Petroleum Conference, Calgary, Alberta, Canada, October 19–21*, SPE 138145

Nichols, G. 2009. Sedimentology and Stratigraphy, 2nd Edition. *Wiley-Blackwell, a John Wiley & Sons, Ltd., Publication.*

NSI Technologies Inc. 2010. Manual for StimPlan.

Olson, J. E. 2003. Sublinear Scaling of Fracture Aperture versus Length: An Exception or the Rule? *Journal of Geophysical Research: Solid Earth* 108, B9: 2413.

Olsson, W., and S.R. Brown. 1993. Hydro-mechanical Response of a Fracture Undergoing Compression and Shear. *International Journal of Rock Mechanics and Mining Sciences & Geomechanics*. 30, 7: 845-851.

Orowan, E. 1948. Fracture and Strength of Solids. *Reports on Progress in Physics* 12, 185-232.

Ortiz, A.C., D.E. Hryb, J.R. Martínez, and R.A. Varela. 2016. Hydraulic Fracture Height Estimation in an Unconventional Vertical Well in the Vaca Muerta Formation, Neuquen Basin, Argentina. In *Proceedings of SPE Hydraulic Fracturing Technology Conference, Woodlands, Texas, 9-11 February*, SPE-179145-MS.

Ouchi, H. 2016. Development of a Peridynamics-based Hydraulic Fracturing Model for Fracture Growth in Heterogeneous Reservoirs, Ph.D. Thesis, The University of Texas at Austin, Austin, TX.

Ouchi, H., J.T. Foster, and M.M. Sharma. 2017. Effect of Reservoir Heterogeneity on the

Vertical Migration of Hydraulic Fractures. *Journal of Petroleum Science and Engineering,* 151:384–408.

Ouchterlony, F., 1990. Fracture Toughness Testing of Rock with Core Based Specimens. *Engineering Fracture Mechanics*, 35: 351-366.

Palmer, I.D., and R.W. Veatch. 1990. Abnormally High Fracturing Pressures in Step-Rate Tests. *SPE Production Engineering* 5, 03: 315–23.

Papanastasiou, P. 1999. The Effective Fracture Toughness in Hydraulic Fracturing. *ResearchGate* 96, 2: 127–147.

Perkins T.K., L.R. Kern. 1961. Widths of Hydraulic Fractures. *Journal of Petroleum Technology* 13, 09: 937–949.

Philipp, S.L., F. Afşar, and A. Gudmundsson. 2013. Effects of Mechanical Layering on Hydrofracture Emplacement and Fluid Transport in Reservoirs. *Frontiers in Earth Science*.

Renshaw, C. E., and D. D. Pollard. 1995. An Experimentally Verified Criterion for Propagation across Unbounded Frictional Interfaces in Brittle, Linear Elastic Materials. *International Journal of Rock Mechanics and Mining Sciences & Geomechanics* 32, 3: 237–249.

Reuss, A. 1929. Berechnung der fließgrenze von mischkristallen auf grund der plastizitätsbedingung für einkristalle . *ZAMM - Journal of Applied Mathematics and Mechanics / Zeitschrift Für Angewandte Mathematik Und Mechanik* 9, 1: 49–58.

Rodrigues, N., P.R. Cobbold, H. Loseth, and G. Ruffet. 2009. Widespread Bedding-parallel Veins of Fibrous Calcite ('beef') in a Mature Source Rock (Vaca Muerta Fm, Neuquén Basin, Argentina): Evidence for Overpressure and Horizontal Compression. *Journal of the Geological Society* 166, 4: 695–709.

Rice, J. R. 1968. A Path Independent Integral and the Approximate Analysis of Strain Concentration by Notches and Cracks. *Journal of Applied Mechanics* 35, 2: 379–86.

Roegiers, J.C., and X.L. Zhao. 1991. Rock Fracture Tests in Simulated Downhole Conditions. *In Proceedings of American Rock Mechanics Association, Rapid City, SD, 26-28 June.*

Rose, L.R.F. 1986. The Crack-size Dependence of Fracture Toughness in Ceramic Polycrystals. *Journal of Materials Science Letters* 5, 4: 455–56.

Rubin, A.M. 1993. Tensile Fracture of Rock at High Confining Pressure: Implications for Dike Propagation. *Journal of Geophysical Research: Solid Earth* 98, B9: 15919–15935.

Schmidt, R.A, and C.W Huddle. 1977. Effect of Confining Pressure on Fracture Toughness of Indiana Limestone. *International Journal of Rock Mechanics and Mining Sciences & Geomechanics* 14, 5: 289–93.

Schultz, R.A., R. Soliva, H. Fossen, C.H. Okubo, and D.M. Reeves. 2008. Dependence of

Displacement–length Scaling Relations for Fractures and Deformation Bands on the Volumetric Changes across Them. *Journal of Structural Geology* 30, 11: 1405–1411.

Searles, K.H., M.G. Zielonka, J. Ning, J.L. Garzon, N.M. Kostov, P.F. Sanz, and E. Biediger. 2016. Fully-Coupled 3D Hydraulic Fracture Models: Development, Validation, and Application to O&G Problems. In *Proceedings of SPE Hydraulic Fracturing Technology Conference. Woodland, Texas. 9-11 February*, SPE 179121.

Shlyapobersky, J. 1985. Energy Analysis of Hydraulic Fracturing. *In Proceedings of American Rock Mechanics Association, Rapid City, SD, 26-28 June.*

Shlyapobersky, J. 1989. On-site Interactive Hydraulic Fracturing Procedures for Determining the Minimum In-situ Stress from Fracture Closure and Reopening Pressures. *International Journal of Rock Mechanics and Mining Sciences & Geomechanics Abstracts* 26, 6: 541–48.

Shlyapobersky, J., G.K. Wong, and W.W. Walhaug. 1988. Overpressure Calibrated Design of Hydraulic Fracture Stimulations. In *Proceedings of the SPE Annual Technical Conference and Exhibition, Houston, Texas, 2–5 October*, SPE 18194.

Shlyapobersky, J., M.A. Issa, M.S. Islam, J.W. Dudley, Y. Shulkin, and A. Chudnovsky. 1998. Scale Effects on Fracture Growth Resistance in Poroelastic Materials. In *Proceeding of the SPE Annual Technical Conference and Exhibition. New Orleans. 27-30 September*, SPE 48929.

Siebrits, E., and A.P. Peirce. 2002. An Efficient Multi-layer Planar 3D Fracture Growth Algorithm Using a Fixed Mesh Approach. *International Journal for Numerical Methods in Engineering* 53, 3: 691–717.

Simonson, E.R., A.S. Abou-Sayed, and R.J. Clifton. 1978. Containment of Massive Hydraulic Fractures. *SPE Journal* 18, 1: 27–32.

Smith, M.B., A.B. Bale, L.K. Britt, H.H. Klein, E. Siebrits, and X. Dang. 2001. Layered Modulus Effects on Fracture Propagation, Proppant Placement, and Fracture Modeling. In *Proceedings of the SPE Annual Technical Conference and Exhibition, New Orleans, 30 September–2 October*, SPE 71654.

Sneddon, I.N. 1946. The Distribution of Stress in the Neighborhood of a Crack in an Elastic Solid. In *Proceedings of the Royal Society of London A: Mathematical, Physical and Engineering Sciences* 187, 1009: 229–60.

Spence, D.A., P.W. Sharp, and D.L. Turcotte. 1987. Buoyancy-driven Crack Propagation: A Mechanism for Magma Migration. *Journal of Fluid Mechanics* 174: 135–53.

Teufel, L.M., and J.A. Clark 1984. Hydraulic Fracture Propagation in Layered Rock: Experimental Studies of Fracture Containment. *SPE Journal* 24, 1: 19–32.

The SCR Geomechanics Group. 1993. On the Modelling of Near-tip Processes in Hydraulic Fractures. *International Journal of Rock Mechanics and Mining*

Sciences & Geomechanics Abstracts 30, 7: 1127–34.

Thiercelin, M. 1987. Fracture Toughness under Confining Pressure Using the Modified Ting Test. *In Proceedings of American Rock Mechanics Association, Tucson, Arizona, 29 June-1 July*.

Thiercelin, M.J., J.C. Roegiers, T.J. Boone, and A.R. Ingraffea. 1987. An Investigation of the Material Parameters that Govern the Behavior of Fractures Approaching Rock Interfaces. In *Proceedings of the International Congress on Rock Mechanics, Montreal, Canada: A. A. Balkema*: 263–269.

Van Eekelen, H.A. 1982. Hydraulic Fracture Geometry: Fracture Containment in Layered Formations. *SPE Journal* 22, 3: 341–349.

Varela, R.A. and J.L. Maniere. 2016. Successful Dynamic Closure Test Using Controlled Flow Back in the Vaca Muerta Formation. In *Proceedings of the SPE Argentina Exploration and Production of Unconventional Resources Symposium, Buenos Aires, Argentina, 1–3 June*, SPE 180997.

Vernik, L., and X. Liu, 1997, Velocity Anisotropy in Shales: A Petrophyscial Study. *Geophysics*, 62: 521–532.

Vernik, L., and J. Milovac, 2011, Rock Physics of Organic Shales. *The Leading Edge*, 30: 318–323.

Voigt, W. 1910. Lehrbuch der Kristallphysik, *Leipzig*.

Wang, Q., and J.F. Gale. 2017. Characterizing Bedding-parallel Fractures in Shale: Aperture-size Distributions and Spatial Organization. In *Proceedings of AAPG Annual Convention and Exhibition, Calgary, Alberta, 22-June.*

Wang, W.W., J.E. Olson, and M. Prodanovic. 2013. Natural and Hydraulic Fracture Interaction Study Based on Semi-circular Bending Experiments. In *Proceeding of the Unconventional Resources Technology Conference. Denver, Colorado. 12–14 August*, URTeC 1576910.

Warpinski, N.R. 1985. Measurement of Width and Pressure in a Propagating Hydraulic Fracture. *Society of Petroleum Engineers Journal* 25, 01: 46–54.

Warpinski, N.R. 2011. Measurements and Observations of Fracture Height Growth. In *Proceedings of US EPA Technical Workshop for the Hydraulic Fracturing Study: Chemical & Analytical Methods, Arlington, Virginia.*

Warpinski, N.R., J.A. Clark, R.A. Schmidt, and C.W. Huddle., 1982. Laboratory Investigation on the Effect of In-Situ Stresses on Hydraulic Fracture Containment. *Society of Petroleum Engineers Journal* 22, 3: 333–340.

Warpinski, N.R., M.J. Mayerhofer, K. Agarwal, and J. Du. 2012. Hydraulic Fracture Geomechanics and Microseismic Source Mechanisms. In *Proceeding of the SPE Annual Technical Conference and Exhibition. San Antonio, TX. 8–10 October*, SPE 158935.

Warpinski, N. R., P.T. Branagan, R.E. Peterson, and S.L. Wolhart. 1998. An Interpretation of M-site Hydraulic Fracture Diagnostic Results. In *Proceedings of SPE Rocky Mountain/Low-Permeability Reservoirs Symposium, Denver, 5–8 April*. SPE 39950.

Warpinski, N.R., R.A. Schmidt, and D.A. Northrop. 1982. In-situ Stresses: the Predominant Influence on Hydraulic Fracture Containment. *Journal of Petroleum Technology* 34, 3: 653–664.

Weinberger, R., Z. Reches, A. Eidelman, and T.E. Scott. 1994. Tensile Properties of Rocks in Four-Point Beam Tests Under Confining Pressure. *In Proceedings of American Rock Mechanics Association, Austin, Texas, 1-3 June.*

Whittaker, B.N., R.N. Singh, G. Sun. 1992. Rock Fracture Mechanics: Principles, Design and Applications, Amsterdam, Elsevier

Workman, S.J., 2013. Integrating Depositional Facies and Sequence Stratigraphy in Characterizing Unconventional Reservoirs: Eagle Ford Shale, South Texas. *Master thesis. Western Michigan University.*

Wright, C.A., E.J. Davis, W.A. Minner, J.F. Ward, L. Weijers, E.J. Schell, and S.P. Hunter. 1998. Surface Tiltmeter Fracture Mapping Reaches New Depths-10,000 Feet and Beyond? In *Proceeding of the 1998 SPE Rocky Mountain Regional/Low-Permeability Reservoirs Symposium and Exhibition. Denver, Colorado. 5–8 April*, SPE 39919.

Wu, K. and J.E. Olson. 2015. Simultaneous Multi-fracture Treatments: Fully Coupled Fluid Flow and Fracture Mechanics for Horizontal Wells. *SPE Journal* 20, 2: 337–46.

Wu, K., J.E. Olson, M.T. Balhoff, and W. Yu. 2015. Numerical Analysis for Promoting Uniform Development of Simultaneous Multiple Fracture Propagation in Horizontal Wells. In *Proceeding of the SPE Annual Technical Conference and Exhibition. Houston. 28–30 September*, SPE 174869.

Xiong, Y., P. Winterfeld, C. Wang, Z.Q. Huang, and Y.S. Wu., 2015. Effect of Large Capillary Pressure on Fluid Flow and Transport in Stress-sensitive Tight Oil Reservoirs. In *Proceedings of the SPE Annual Technical Conference and Exhibition, Houston, Texas, 28–30 September*, SPE 175074.

Yao, Y., L. Liu, and L.M. Keer. 2015. Pore Pressure Cohesive Zone Modeling of Hydraulic Fracture in Quasi-Brittle Rocks. *Mechanics of Materials* 83: 17–29.

Yue, K., J.E. Olson, and R.A. Schultz. 2016. Calibration of Stiffness and Strength for Layered Rocks. In *Proceedings of US Rock Mechanics / Geomechanics Symposium, Houston, TX, 26–29 June*. ARMA 16–460.

Zhang, X., R.G. Jeffrey, and M. Thiercelin. 2007. Deflection and Propagation of Fluid-driven Fractures at Frictional Bedding Interfaces: a Numerical Investigation. *Journal of Structural Geology* 29, 3: 396–410.

Zhang, X. and R.G. Jeffrey. 2008. Reinitiation and Termination of Fluid-driven Fractures at Frictional Bedding Interfaces. *Journal of Geophysical Research* 113, B08416.

Zhu, X., and J.A. Joyce. 2012. Review of Fracture Toughness (G, K, J, CTOD, CTOA) Testing and Standardization. *Engineering Fracture Mechanics* 85: 1–46.

Zoback, M.D. 2007. Reservoir Geomechanics. New York: Cambridge University Press.